



Dottorato di Ricerca in Ingegneria Civile
Graduate School in Civil Engineering

Sede: Facoltà di Ingegneria - Università di Pavia - via Ferrata 1 - 27100 Pavia - Italy

Dottorato di Ricerca in Ingegneria Civile VII Ciclo nuova Serie
(XXI Ciclo)

**Experimental Applications on Cu-based
Shape Memory Alloys: Retrofitting of
Historical Monuments and Base Isolation**

Ph.D. Thesis
Karim Hamdaoui

Advisor:
Prof. Fabio Casciati

Revisor:
Prof. Alberto Marcellini

Pavia, October 2008

To my family

Dottorato di Ricerca in Ingegneria Civile

Settore:	Ingegneria
Field:	Engineering
Sede Amministrativa non consortile:	Università degli Studi di PAVIA
Administrative location:	University of Pavia
Durata del dottorato:	3 anni
Duration:	3 years
Periodo formativo estero (in mesi):	come previsto dal regolamento del Dottorato di Ricerca
Period in external organization:	as required by the school's law
Numero minimo di corsi:	6
Nminimum number of courses:	6

Recapiti - Addresses



Dipartimento di Meccanica Strutturale
via Ferrata 1 - 27100 Pavia - Italy
Tel. +39/ 0382 985450 Fax +39/ 0382 528422



Dipartimento di Ingegneria Idraulica e Ambientale
via Ferrata 1 - 27100 Pavia - Italy
Tel. +39/ 0382 / 985300 Fax +39/ 0382 985589

Coordinatore - Coordinator

CASCIATI Fabio - Professore Ordinario di Scienza delle Costruzioni (ICAR/08)

Dipartimento di Meccanica Strutturale
Via Ferrata 1 - 27100 Pavia – Italy Tel. +39/0382 985458 Fax +39/0382 528422
E-mail: fabio@dipmec.unipv.it

Collegio dei Docenti – Teaching Staff

CASCIATI Fabio	Professore Ordinario (ICAR/08)
CIAPONI Carlo	Professore Straordinario (ICAR/01)
DEL GROSSO Andrea	Professore Ordinario, Unige (ICAR/09)
FARAVELLI Lucia	Professore Ordinario (ICAR/08)
GALLATI Mario	Professore Ordinario (ICAR/01)
GOBETTI Armando	Professore Associato (ICAR/08)
MOISELLO Ugo	Professore Ordinario (ICAR/02)
PAPIRI Sergio	Professore Associato (ICAR/02)
SALA Roberto	Professore Associato (ING-IND/08)
MARCELLINI Alberto	Dirigente di Ricerca. CNR – Milano.

Organizzazione del corso

Il dottorato di ricerca in *Ingegneria Civile* presso la Facoltà di Ingegneria dell'Università degli Studi di Pavia è stato istituito nell'anno accademico 1994/95 (X ciclo).

Il corso consente al dottorando di scegliere tra due curricula: idraulico o strutturale. Egli svolge la propria attività di ricerca rispettivamente presso il Dipartimento di Ingegneria Idraulica e Ambientale o quello di Meccanica Strutturale.

Durante i primi due anni sono previsti almeno sei corsi, seguiti da rispettivi esami, che il dottorando è tenuto a sostenere. Il Collegio dei Docenti, composto da professori dei due Dipartimenti, organizza i corsi con lo scopo di fornire allo studente di dottorato opportunità di approfondimento su alcune delle discipline di base per entrambe le componenti, idraulica e strutturale. Corsi e seminari vengono tenuti da docenti di Università nazionali ed estere.

Il Collegio dei Docenti, cui spetta la pianificazione della didattica, si è orientato ad attivare ad anni alterni corsi sui seguenti temi:

- Meccanica dei solidi e dei fluidi
- Metodi numerici per la meccanica dei solidi e dei fluidi
- Rischio strutturale e ambientale
- Metodi sperimentali per la meccanica dei solidi e dei fluidi
- Intelligenza artificiale

più corsi specifici di indirizzo.

Al termine dei corsi del primo anno il Collegio dei Docenti assegna al dottorando un tema di ricerca da sviluppare sotto forma di tesina entro la fine del secondo anno; il tema, non necessariamente legato all'argomento della tesi finale, è di norma coerente con il curriculum, scelto dal dottorando (idraulico o strutturale).

All'inizio del secondo anno il dottorando discute con il Coordinatore l'argomento della tesi di dottorato, la cui assegnazione definitiva viene deliberata dal Collegio dei Docenti.

Alla fine di ogni anno i dottorandi devono presentare una relazione particolareggiata (scritta e orale) sull'attività svolta. Sulla base di tale relazione il Collegio dei Docenti, “previa valutazione della assiduità e dell'operosità dimostrata dall'iscritto”, ne propone al Rettore l'esclusione dal corso o il passaggio all'anno successivo.

Il dottorando può svolgere attività di ricerca sia di tipo teorico che sperimentale, grazie ai laboratori di cui entrambi i Dipartimenti dispongono, nonché al Laboratorio Numerico di Ingegneria delle Infrastrutture.

Il “Laboratorio didattico sperimentale” del Dipartimento di Meccanica Strutturale dispone di:

1. una tavola vibrante che consente di effettuare prove dinamiche su prototipi strutturali;
2. opportuni sensori e un sistema di acquisizione dati per la misura della risposta strutturale;
3. strumentazione per la progettazione di sistemi di controllo attivo e loro verifica sperimentale;
4. strumentazione per la caratterizzazione dei materiali, attraverso prove statiche e dinamiche.

Il laboratorio del Dipartimento di Ingegneria Idraulica e Ambientale dispone di:

1. un circuito in pressione che consente di effettuare simulazioni di moto vario;
2. un tunnel idrodinamico per lo studio di problemi di cavitazione; canalette per lo studio delle correnti a pelo libero.

Course Organization

The Graduate School of Civil Engineering at the University of Pavia was established in the Academic Year of 1994/95 (X cycle). The School allows the student to select one of the four offered curricula: Hydraulics, Environment, Seismic engineering and Structural Mechanics. Each student develops his research activity either at the Department of Hydraulics and Environmental Engineering or at the Department of Structural Mechanics. During the first two years, a minimum of six courses must be selected and their examinations successfully passed. The Faculty, made by Professors of the two Departments or by internationally recognized scientists, organizes courses and provides the student with opportunities to enlarge his basic knowledge. Courses and seminars are held by University Professors from all over the country and abroad. The Faculty starts up in alternate years common courses, on the following subjects:

- solid and fluid mechanics,
- numerical methods for solid and fluid mechanics,
- structural and environmental risk,
- experimental methods for solid and fluid mechanics,
- artificial intelligence.

More specific courses are devoted to students of the single curricula. At the end of each course, for the first year the Faculty assigns the student a research argument to develop, in the form of report, by the end of the second year; the topic, not necessarily part of the final doctorate thesis, should be consistent with the curriculum selected by the student. At the beginning of the second year the student discusses with his Coordinator the subject of the thesis and, eventually, the Faculty assigns it to the student. At the end of every year, the student has to present a complete report on his research activity, on the basis of which the Faculty proposes to the Rector his admission to the next academic year or to the final examination. The student is supposed to develop either theoretical or experimental research activities, and therefore has access to the Department

Experimental Laboratories, even to the Numerical Laboratory of Infrastructure Engineering. The Experimental Teaching Laboratory of the Department of Structural Mechanics offers:

1. a shaking table which permits one to conduct dynamic tests on structural prototypes;
2. sensors and acquisition data system for the structural response measurements;
3. instrumentation for the design of active control system and their experimental checks;
4. an universal testing machine for material characterization through static and dynamic tests.

The Department of Hydraulics and Environmental Engineering offers:

1. a pressure circuit simulating various movements;
2. a hydrodynamic tunnel studying cavitation problems; micro-channels studying free currents.

Elenco delle tesi – Previous Theses

Battaini Marco (X Ciclo)	Sistemi strutturali controllati: progettazione e affidabilità.
Mariani Claudia (X Ciclo)	Problemi di ottimizzazione per strutture bidimensionali anisotrope.
Negri Antonella (X Ciclo)	Stima delle perdite idrologiche nei bacini di drenaggio urbani.
Pisano Aurora Angela (XI Ciclo)	Structural System Identification :Advanced Approaches and Applications.
Saltalippi Carla (XI Ciclo)	Preannuncio delle piene in tempo reale nei corsi d'acqua naturali.
Barbieri Eugenio (XI Ciclo)	Thermo fluid Dynamics and Topology: Optimization of an Active Thermal Insulation Structure.
Barbolini Massimiliano (XII Ciclo)	Dense Snow Avalanches: Computational Models, Hazard Mapping and Related Uncertainties.
Espa Paolo (XII Ciclo)	Moti atmosferici generati da forze di galleggiamento: simulazioni numeriche e studio su modello fisico.
Petrini Lorenza (XII Ciclo)	Shape Memory Alloys: Modelling the Martensitic Phase Behaviour for Structural Engineering Exploitation.

Podestà Stefano (XIII Ciclo)	Risposta sismica di antichi edifici religiosi: una nuova proposta per un modello di vulnerabilità.
Sturla Daniele (XIII Ciclo)	Simulazioni lagrangiane di flussi rapidamente variati nell'approssimazione di acque poco profonde.
Marazzi Francesco (XV Ciclo)	Semi -active Control of Civil Structures: Implementation Aspects.
Nascimbene Roberto (XV Ciclo)	Sail Modelling for Maximal Speed Optimum Design.
Giudici Massimo (XVI Ciclo)	Progettazione in regime non lineare di strutture in CAP a cavi aderenti e non aderenti.
Mutti Matteo (XVI Ciclo)	Stability Analysis of Stratified Three—phase Flows in Pipes.
Petaccia Gabriella (XVI Ciclo)	Propagazione di onde a fronte ripido per rottura di sbarramenti in alvei naturali.
Casciati Sara (XVII Ciclo)	Damage Detection and Localization in the Space of the Observed Variables.
D'Amico Tiziana (XVI Ciclo)	Ricerca e sviluppo di metodologie diagnostiche per il recupero di edifici monumentali: prove vibroacustiche sul tufo.
Barco Olga Janet (XVII Ciclo)	Modeling the Quantity and Quality of Storm Water Runoff Using SWMM.
Boguniewicz Joanna (XVIII Ciclo)	Integration of Monitoring and Modelling in the Surface Water State Evaluation Process of a Sub-Alpine Lake Watershed.

Bornatici Laura (XVIII Ciclo)	L'impiego degli algoritmi generici per la risoluzione dei problemi di progetto di reti di distribuzione idrica.
Collivignarelli M Cristina (XVIII Ciclo)	rattamento di rifiuti liquidi mediante processi biologici aerobici termofili e mesofili e processi avanzati di ossidazione chimica in diversa.
Domaneschi Marco (XVIII Ciclo)	Structural Control of Cable-stayed and Suspended Bridges.
Ráduly Botond (XVIII Ciclo)	Artificial Neural Network applications in Urban Water Quality Modeling.
Antoci Carla (XVIII Ciclo)	Simulazione numerica dell'interazione fluido-struttura con la tecnica SPH.
Cappabianca Federica (XVIII Ciclo)	La valutazione del rischio valanghivo attraverso la modellazione dinamica.
Callegari Arianna (XVIII Ciclo)	Applicazione di tecnologie di monitoraggio on-line per la gestione dei processi di trattamento reflui.
Gazzola Elisa (XVIII Ciclo)	Applicazione di processi biologici anaerobici al trattamento di acque reflue e fanghi di depurazione: aspetti tecnici ed energetici.
Giuliano Fabio (XIX Ciclo)	Performance Based Design and Structural Control for Cable Suspension Bridges.
Maranca Federica (XVIII Ciclo)	Valutazione del ciclo di vita (LCA): confronto tra sistemi di trasporto gas via gasdotto.
Falappi Stefano (XIX Ciclo)	Simulazioni numeriche di flussi di fluidi viscosi e materiali granulari con la tecnica SPH.

Zanaboni Sabrina (XIX Ciclo)	Pre-trattamento di rifiuti liquidi industriali mediante ossidazione ad umido.
Bruggi Matteo (XX Ciclo)	Topology optimization using mixed finite elements.
Cimellaro Gian Paolo (XX Ciclo)	Passive Control of Industrial Structures for Natural Hazard Mitigation: Analytical Studies and Applications.
Pagliardi Matteo (XX Ciclo)	Application of PIV technique to the study of subaqueous debris flows.
Todeschini Sara (XX Ciclo)	Il controllo degli scarichi fognari in tempo di pioggia mediante vasche di prima pioggia: aspetti progettuali e gestionali.

Acknowledgments

The author wishes to express all his deep gratitude and appreciation to his advisor, Prof. Fabio Casciati, for his patient guidance, constant support and, valuable comments during the development of this research.

The author wants to present his special thanks to Prof. Lucia Faravelli for her constructive suggestions and help throughout his Ph.D studies period.

The author would like to extend his sincere tanks Prof. Alberto Marcellini, CNR - Milano, for his direction and time spending to evaluate this work.

Acknowledgments are due to Eng. Mauro Mottini for his considerable help and friendship during the elaboration of the laboratory tests in the University of Pavia, Dr. Christis Chrysostomou and Eng. Themis Demetriou for their hospitality and valuable comments during the performance of the in situ tests in Cyprus.

Special thanks are extended to Prof. Khaldoun Bani Hani and Prof. Hazim Zibdeh, Jordan University of Science and Technology, Jordan, Dr. Nadir Boumechra, University of Tlemcen, Algeria, and Prof. Sami El-Borgi, Tunisia Polytechnic School, Tunisia, for their unconditional support and respect to science.

The author would like to thank his friends: Clemente Fuggini, Matteo Bruggi, Marco Domaneschi, Filippo Ubertini, Thomas Meservey, Sara Casciati, Alexandro Marzzi and Luca Bossi for their sincere amity in Italy, Mohammed Mankouri, Issam Kacemi, Mahmoud Larbaoui, Hadj Kadid and Brahim Bentrari for their unchanging friendship and encouragements although they were far from him, in Algeria.

Indice – Contentes

Abstract pag. 1

Chapter 1

Introduction

- 1.1. Shape Memory Alloys (SMA) pag. 3
- 1.2. SMAs for seismic retrofitting pag. 7
- 1.3. Studied cases pag. 13
- 1.4. Organization of the Text pag. 14
- 1.5. References pag. 17

Chapter 2

Algeria, its Seismic Activity and its Monumental Cultural Heritage

- 2.1. Background of Algerian society pag. 19
- 2.2. Background on the seismic activity of Algeria pag. 22
- 2.3. Archaeological sites and monuments of Algeria pag. 47
- 2.4. References pag. 61

Chapter 3

Pre-stressed SMA Wires for Structural Retrofitting: the Masonry Wall Model

3.1. Introduction	pag. 65
3.2. Characterization of proposed masonry wall	pag. 67
3.3. Methodology and testing procedure	pag. 70
3.4. The wall in its virgin state	pag. 71
3.5. Adding SMA ties	pag. 80
3.6. Comparison of using SMA versus steel ties	pag.102
3.7. Conclusions	pag.104
3.8. References	pag.105

Chapter 4

Pre-stressed SMA Wires for Structural Retrofitting: the Aqueduct of Larnaca

4.1. Introduction	pag.107
4.2. Description of the monument	pag.109
4.3. Structural health monitoring and System identification	pag.110
4.4. Experimental Analysis	pag.114
4.5. Measurements with using SMA wires	pag.128
4.6. Discussion	pag.139
4.7. Conclusion	pag.145
4.8. References	pag.147

Chapter 5

SMA Bars as Base Isolation Device

5.1. Introduction	pag.151
5.2. Base isolation of works of art and monuments	pag.154
5.3. The proposed device	pag.156
5.4. ANSYS FE element code as workbench environment	pag.158
5.5. The material model	pag.160
5.6. The device's numerical model: Single bar	pag.162
5.7. Experimental features	pag.169
5.8. Conceiving the device prototype	pag.172
5.9. Geometry of the experimentally tested device	pag.184
5.10 Prototype test and system identification	pag.187
5.11 Test details and hysteresis loops	pag.192
5.12 Conclusion	pag.200
5.13 References	pag.203

Conclusions	pag.205
--------------------	---------

Bibliografy	pag.211
--------------------	---------

Abstract

Experimental applications on Cu-based Shape Memory Alloys (SMA) are focussed in this thesis. First, SMA wires are proposed for the retrofitting of historical monuments, then as an innovative base isolating system.

A brief review on the seismic activity of Algeria, as the author is originated from, is presented. The country is considered as the most active seismogenic region in the Western Mediterranean area. Historically, this zone showed a significant seismicity and had experienced many destructive earthquakes. Consequently, the historical monuments and the ancient structures which survived need to be protected. Some cultural heritage and historical monuments of the country are then described, in the aim to nominate them for future applications of the proposed techniques.

In view of a first application, pre-tensioned wires are anchored on a scaled masonry wall model built only with superposed bricks (to reproduce the properties of a monumental structure). Shaking table experiments are carried out when the wall is reinforced with 0, 2, 4 and 6 SMA wires. The experimental results are compared with those from numerical analysis. For this purpose a 3-D, 8-node, solid finite elements model is built using SAP 2000. The effectiveness of the retrofit with SMA wires is then checked by evaluating numerically the case when steel is used instead of SMA wires. Following the conclusions from these laboratory tests, SMA ties are inserted on a real monumental structure: the aqueduct of Larnaca in Cyprus. The monument is then reinforced with 0, 4, 12, 20, 16, 8 wires. Ambient vibration tests are performed to get the dynamic characteristics of each case of reinforcement. The insertion of SMA wires shows a significant effect on the dynamic characteristics of the aqueduct.

A new concept of base isolator is then introduced as second application. The innovative system consists of several SMA bars assembled in a suitable geometry. The device is designed to bear a steel plate that serves as superimposed tray, where the system to be isolated is built up. A numerical model of the isolator is built. A prototype of the device is also built and experimentally tested on the shaking table. It is shown that the main feature of the proposed base isolation device is that for cyclic loading, the super-elastic behaviour of the alloy results in wide load-displacement loops, where a large amount of energy is dissipated.

Finally, concluding remarks are made, and recommendations for future works are outlined.

Chapter 1

Introduction

1.1 Shape Memory Alloys (SMA)

The series of Nickel/Titanium alloys developed by Buehler and Wiley [Buehler and Wiley, 1965] in 60', exhibited a special property allowing them to regain and remember their original shape, although being severely deformed, upon a thermal cycle. This remarkable characteristic became known as the shape memory effect, and alloys that exhibit it were named shape memory alloys. Later, it was found that at sufficiently high temperatures, such materials also have the super-elasticity property: the recovery of large deformations during mechanical loading-unloading cycles performed at constant temperature [Auricchio, 1995], [Auricchio et al., 2001]. Subsequently, SMAs lend themselves to innovative applications.

SMAs change their crystalline arrangement as they are cooled down or heated up, as well as in the presence of a stress field. They have two stable phases: austenite, at high temperature, and martensite at low temperature. Additionally, the later one (martensite) can be in one of two forms: twinned or de-twinned.

If cooled, and in the absence of any applied load, the material transforms from austenite into twinned martensite phase. Here, no observable macroscopic shape change is seen. When the material in its martensitic phase is heated, a reverse phase transformation occurs and the material is transformed to the austenite phase.

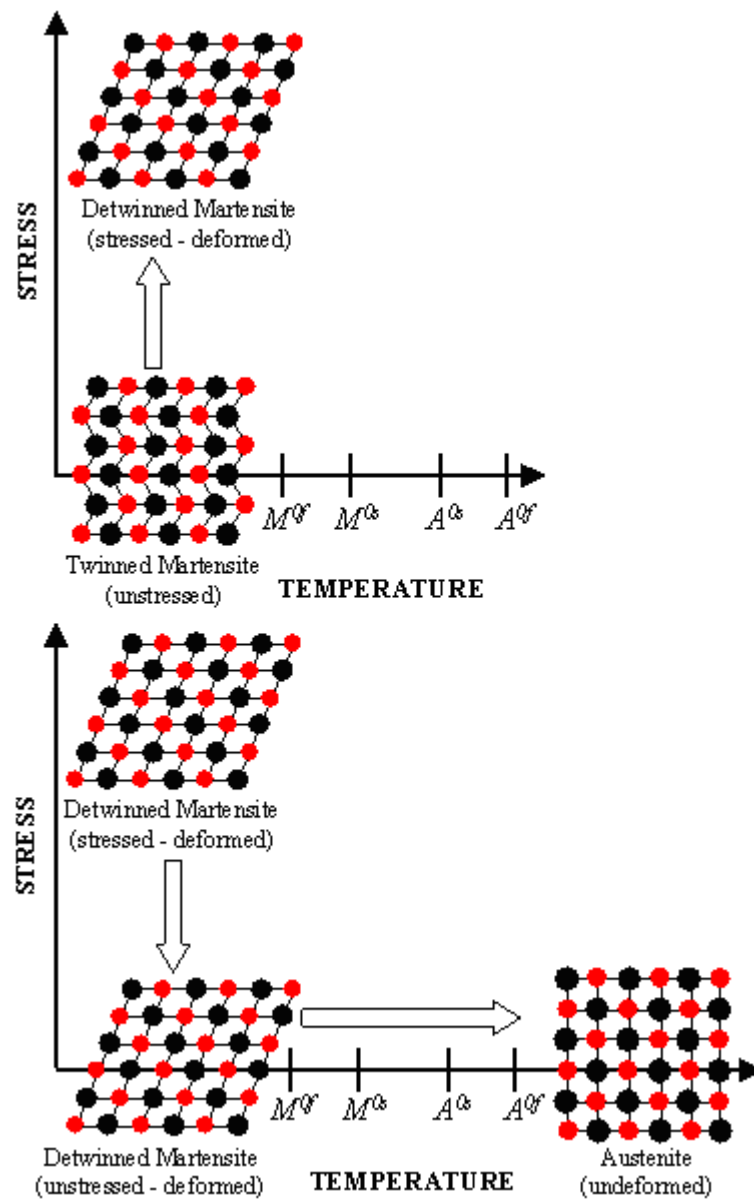


Figure 1.1: Temperature-induced phase transformation and shape memory effect of SMA [from smartlab, 2008].

In Figure 1.1, this process is illustrated and four characteristic temperatures are defined: i) M^{0s} , the martensitic start temperature (transformation from austenite to martensite); ii) M^{0f} , martensitic finish temperature (the material is fully in the martensitic phase); iii) A^{0s} , austenite start temperature (beginning of the reverse transformation (austenite to martensite)); and iv) A^{0f} , austenite finish temperature (the material is the austenitic phase).

A detailed references list on the use of SMAs metals in different engineering applications are provided in the book [Auricchio et al., 2001]. The same book illustrates their use in vibration control in the form of austenitic wires. More recently, investigations are focussed on the possibility of using the pre-stressed SMA wires to sew ancient buildings made by blocks [Casciati and Faravelli, 2004] and [Casciati et al., 2005].

The mechanic characteristics of the Nickel/Titanium (NiTi) alloys has already been widely investigated [Auricchio et al., 2001], [Saadat et al., 2002] and [Casciati, 2003]. Commercial products (of Nitinol) were already adopted in the retrofitting of a famous church [Auricchio et al., 2001], [Saadat et al., 2002], and a numerical simulations when implementing the constitutive law of a commercial Ni-Ti alloy as a subroutine in the retrofitting of a large Egyptian monolithic statue, called the Memnon Colossus, was shown in [Casciati and Osman, 2005].

Because of their expensive cost and their limited range of potential transformation temperatures, the application of the NiTi alloy might not be the best candidate for the seismic retrofit of cultural heritage structures. Therefore, [Casciati and Faravelli, 2004] checked the availability of an alloy different from NiTi for the application in monumental retrofitting. The interest was focused on the Copper-based, which is another type of alloy, that consists of Cu, Al and Be chemical composites.

Several mechanical tests were also performed on this kind of alloys [Isalgue et al., 2002], [Faravelli and Casciati, 2003], [Casciati and Faravelli, 2003] and [Casciati and Faravelli, 2004]. Recently, Cu-based SMAs were used, in the

form of 2.85 mm wires, to reinforce a prototype of masonry wall to be tested in laboratory [Delmonte, 2007].

A basic aspect in managing the Cu Al Be alloy is the thermal treatment. Each SMA wire needs to be heated in an oven at 850°C for a time period that ranges between 1 and 5 minutes and depends on the specimen's cross section, as shown in Table 1.1 [Casciati F. and Faravelli, 2004].

Table 1.1: Thermal treatment.

Specimen Diameter (mm)	Heating Time (minutes)
1	1
3	3
6	4

The cooling to ambient temperature follows this process by direct immersion in water. To complete the process, the wires are treated for 120 minutes in an oven at 100°C, and then cooled, again to ambient temperature.

The engineering application is still limited mainly because the complete understanding and control of the SMA's properties and the associated metallographic processes are still being developed. The super-elastic behaviour exhibits good damping capacity because of the necessary energy for the phase transformations. The movement of the austenite-martensite interfaces and interfaces between martensite variants contribute to the damping effect as well. The introduction of SMAs into engineering applications requires careful answers to a long list of questions:

- what if the traction is replaced by compression, shear or a more general stress combination?
- how long and how flat is the plateau?
- is the stress-strain relationship stationary or evolutionary?
- which are the associated fatigue properties?
- how all these properties evolve with temperature?

Most of them can only be obtained by deep experimental compaign.

1.2 SMAs for seismic retrofitting

Standard restoration techniques are often inadequate, when dealing with historical monuments. Not invasive operations need to be performed and the traditional retrofitting methods often do not give the structures sufficient resistance against maximum expected earthquakes. These facts underscore the need for further research on innovative techniques to protect old structures, (especially the cultural heritage) against seismic hazard. These techniques should guarantee structural stability and, at the same time, respect as much as possible their integrity.

Within the framework of the project “WIND-CHIME” (Wide-Range Non-Intrusive Devices Toward Conservation of Historical Monuments in the Mediterranean Area [WIND-CHIME, 2007]), funded by the European Commission, innovative techniques based on the use of SMA devices have been studied and experimentally tested to protect historical monuments from the effects of earthquakes. The results are summarized in this thesis.

For seismic applications, the first property is the alloy super-elasticity: the crystal structure of the material will not be degraded if the alloy is under stress. In the loading-unloading stress strain path shown in Figure 1.2, the SMA material is first loaded (ABC), showing a nonlinear behaviour. Then, when unloaded (CDA), the reverse transformation occurs. This behaviour is hysteretic with no permanent strain [Auricchio et al., 1997]. The two plateaus shown by the material in the stress-strain curve could represent the area inside which, civil materials could work safely. The difference between the two levels of stress multiplied by the corresponding strain range gives the energy absorbed in the hysteresis loop by the SMA.

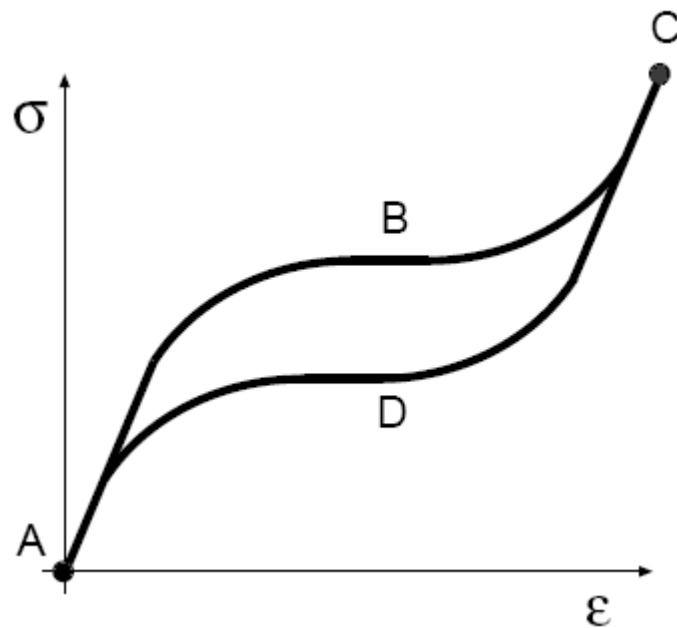


Figure 1.2: Typical super-elastic behaviour of SMA.

The basic idea is to connect part of the main walls by SMA devices that should behave as follow [Auricchio et al., 2001]:

- Under service loads; the device does not apply any static force to the structural elements that connects (and consequently it is called “self-balanced”);
- Under low intensity dynamic horizontal actions (wind, small intensity earthquakes) the device remains stiff, as traditional steel ties do, not allowing significant displacements;
- Under higher intensity dynamic horizontal actions (i.e. design earthquakes) the stiffness of the device significantly decreases, allowing the wall “controlled displacements”, while the force remains almost constant. This behaviour should reduce the amplification of accelerations (as compared to stiff connections). The structure should

- be able to sustain a high intensity earthquake without collapse, though undergoing some minor damage;
- Under extraordinary dynamic horizontal actions (i.e. earthquakes stronger than the design earthquake), the stiffness of the device increases and thus prevents instability.

The following examples illustrate the effectiveness of SMA device based techniques for seismic retrofitting of historical monuments instead the use of traditional one with steel ties. The case of Figure 1.3 is the rocking of gable-end walls [Auricchio et al., 2001], due to inertia forces generated by the earthquake and acting orthogonally to the wall. It is mainly due to the absence of an effective connection of the wall with the roof and/or the floors. A common intervention technique used to prevent the rocking of the gable-end walls is to improve the connection between facades walls and floors and/or orthogonal walls by means of steel tie-rods. Nonetheless, such reinforcement techniques often prove to be inadequate in preventing collapse. Indeed, other types of collapse may be introduced by the earthquake, as those shown in Figure 1.4. It has been observed from past earthquakes damage [Doglioni et al., 1994] that the presence of steel ties connecting the façade with the roof does not avoid tympana collapse (Figure 1.4, top left).

Furthermore, the high stiffness of steel bars used as ties causes high forces to be transmitted to the masonry structure during an earthquake. Consequently, the connection can fail due to the “punching” effect of the anchorage, especially in cases where the masonry materials in question are of poor quality or deteriorated by aging.

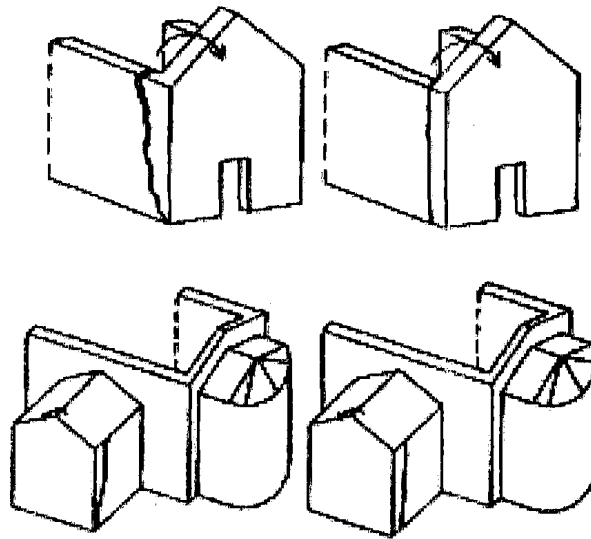


Figure 1.3: Examples of rocking walls due to absence of connections.

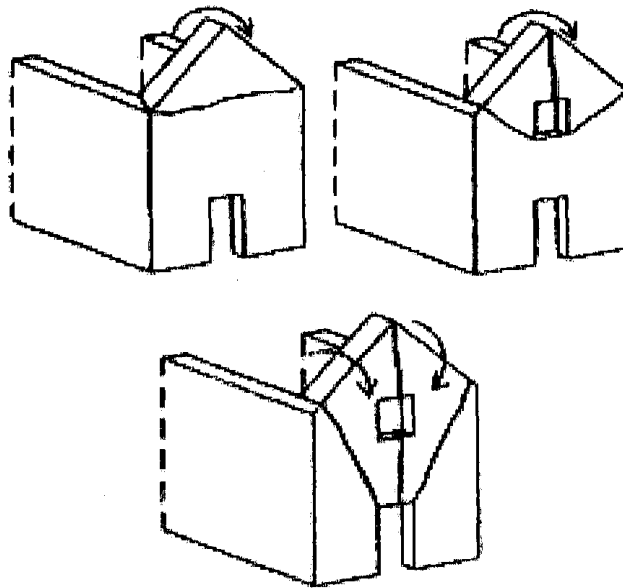


Figure 1.4: Examples of upper collapse by "punching" effect.

In order to prevent the above described collapse, an intervention technique using SMA device as ties has been developed. The idea is to use SMAs to realize a connection that has the advantage of the traditional steel ties (i.e. the ability to prevent rocking) but that at the same time has not the above described drawbacks of steel ties.

Another typical damage induced by an earthquake in masonry structures is the one shown in Figure 1.5 that is the formation of diagonal and X-diagonal cracks resulting from shear forces in the plane of the walls. This damage constitutes a lessening of the lateral stiffness of the building, and can induce instability and collapse when the relative displacement across the cracks becomes large. Techniques based on the used of SMA wires have been developed even to prevent instability and collapse due to this type of damage. It is well known that the shear strength of masonry can be increased by pre-stressing it with steel tendons (bars or stands). The addition of SMA devices in series with tendons adds the advantage of limiting the amount of stress that the masonry undergoes under both service and seismic conditions. Working on the super-elastic plateau of SMAs guarantees a fairly constant force even in the presence of a significant deformation. Furthermore, the energy dissipation capacity of the SMAs can help to reduce damage as well as to increase structural stability even under strong earthquakes.

The use of SMA devices in series with conventional steel tendons for masonry has also been shown useful to prevent flexural collapse of tall and slender structures such as towers (see Figure 1.6) or instability of columns and colonnades. In such type of applications, the advantage met by the use of SMA devices, in comparison with the use of simple steel tendons, is their ability to act as force limiting devices owing to the super-elastic behaviour.

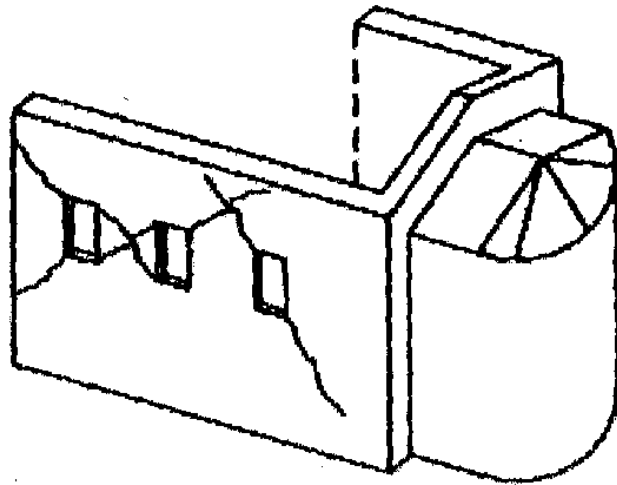


Figure 1.5: Example of in-plane damage due to low shear strength limit.

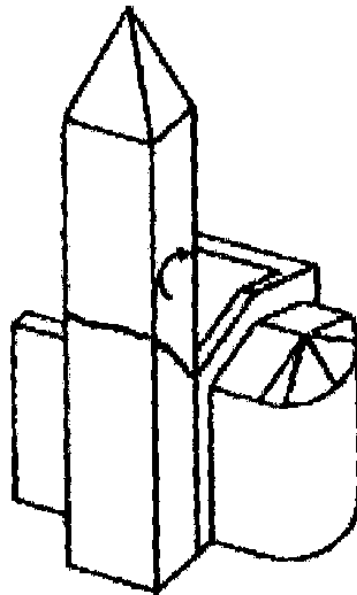


Figure 1.6: Typical flexural collapse in bell tower un-reinforced.

1.3 Studied cases

In this thesis, three case studies will be investigated: i) a scaled masonry wall model with implemented SMA wires, ii) an application of SMA devices on an ancient structure: the aqueduct of Larnaca in Cyprus, and, iii) the performance of a base isolator with SMA bars.

For the first case, the structural behaviour of a scaled masonry model will be studied. Shaking table tests will be conducted to capture the accelerations at the top and the bottom of the wall. Output-only modal identification techniques will be used to extract the modal frequencies. A three-dimensional finite element model of the structure, using software package SAP 2000 [SAP, 2003], will be developed and calibrated according to the modal parameters obtained experimentally by the shaking table test results and the measured characteristics of the bricks (without mortar).

In the second case, an application of SMA devices on an ancient structure the “Aqueduct of Larnaca” will be seen and, as first step, the structural behaviour of the selected monument will be investigated. After dimensional measurements and determination of its current state of damage, ambient vibration tests will be drawn to detect the accelerations at selected locations on the aqueduct using very sensitive sensors. The modal frequencies and mode shapes will be extracted by applying output-only modal identification techniques. Three-dimensional finite element model of the structure, using the same software (SAP 2000), will be developed then calibrated according to the modal parameters experimentally obtained by the ambient vibration test results and the measured characteristics of the old stone and deteriorated mortar. The second step will focus on the rehabilitation, when incorporating SMA devices. The monument will be characterized again by a system identification study which includes measurements and computational models. The models will be used to test the effectiveness of SMA pre-stressed devices and SMA dampers in protecting the monument from future catastrophic earthquakes. The results of

the application of the SMA devices and their effects are presented and discussed.

As a third case, SMA bars will be assembled in a base isolator, where its performance will be studied. A new and innovative base isolator in which a sliding system is coupled with inclined SMA bars in its austenite phase will be presented. The proposed prototype will be modelled and tested. To model this specific material requires a very complex constitutive law description, possibly accounting for the martensite fractions in it. Shaking table test will be conducted to verify the expected performance of the prototype. The tested structure will be subjected to sinusoidal waves of displacement of increasing frequency with different amplitudes. Based on experimental observations carried out on the model, the main feature is that for cyclic loading, the super-elastic behaviour of the alloy results in wide load-displacement loops, where a large amount of energy is dissipated. These loops become smaller and smaller as the excitation intensity decays, resulting in the device re-centring.

1.4 Organization of the Text

In the aim to give an overview to the reader, the organization of the thesis is presented here. This study lies in six chapters, beginning with the current one, which introduces the work and presents the study.

Chapter two deals with the seismicity of Algeria and provides a description of its cultural heritage and historical monuments. Here, the idea is to introduce the available monuments in the country with the intention that they will be the site of future applications of the proposed techniques.

In chapter three, a scaled masonry wall model is tested before and after implementing a number of SMA wires. The cases when 0, 2, 4 and 6 SMA wires are introduced and discussed.

Chapter four discusses the experimental application of SMA devices on the aqueduct of Larnaca. This chapter is the real-scale application of the results discussed in the third one, which first provides the laboratory results.

In chapter five, the performance of an innovative base isolator with inclined SMA bars is studied. A prototype model is first modelled using the ANSYS software, and then tested on a shaking table.

Finally, chapter six presents the conclusions and some recommendations for future works.

References:

1. Auricchio F. (1995). "Shape Memory Alloys: Applications, Micromechanics, Macromodelling and Numerical Simulations", *Ph.D Thesis*, University of California at Berkeley, USA.
2. Auricchio F., Faravelli L., Magonette G. and Torra V. (eds.) (2001). *Shape Memory Alloys: Advances in Modelling and Applications*, CIMNE, Barcelona.
3. Auricchio F., Taylor R.L. and Lubliner J. (1997). "Shape-Memory Alloys: Macromodeling and Numerical Simulations of the Superelastic Behavior", *Computational Methods in Applied Mechanical Engineering*, vol. 146, 281-312.
4. Buehler W.J. and Wiley R.C. (1965). "Nickel-based Alloys", *Technical report*, US-Patent 3174851.
5. Casciati F. (ed.) (2003). *Proceeding of the 3rd World Conference on Structural Control*, John Wiley & sons, Chichester.
6. Casciati F. and Faravelli L. (2004). "Experimental Characterization of a Cu-based Shape Memory Alloy toward Its Exploitations in Passive Control Devices", *Journal de Physique IV*, vol. 115, 299-306.
7. Casciati S. and Faravelli L. (2003). "Thermo-mechanic Properties of a Cu Based Shape Memory Alloy", *Proceedings SMART03*, Warsaw, Poland.
8. Casciati S. and Faravelli L. (2004). "Fastening Cracked Blocks by SMA Devices", *Proceedings of the 3rd European Conference on Structural Control*, Vienna, Austria, M1-1/M1-4.
9. Casciati S. and Faravelli L. (2004). "Thermo-mechanic Characterization of a Cu-Based Shape Memory Alloy", *Proceedings SE04*, Osaka, Japan, 377-382.
10. Casciati S. and Osman A. (2005). "Damage Assessment and Retrofit Study for the Luxor Memnon Colossi", *J. Structural Control & Health Monitoring*, vol. 12, no. 2, 139-159.
11. Casciati S., Faravelli L. and Domaneschi M. (2005). "Dynamic tests on Cu-based shape memory alloys toward seismic retrofit of cracked stone

- monuments”, *Workshop on smart structures and advanced sensor technologies*, June 26-28, Santorini Island, Greece.
12. Delmonte G. (2007). “Pretensionamento Con Fili In Lega A Memoria Di Forma Di Elementi Strutturali Murari”, *Master Thesis*, Department of Structural Mechanics, University of Pavia, Italy. (In Italian).
 13. Doglioni F., Moretti A. and Petrini V., (eds.) (1994). *Le Chiese e il terremoto*. Edizione Lint, Trieste. (In Italian).
 14. Faravelli L. and Casciati S. (2003). “Dynamic behavior of a Shape Memory Alloy Structural Devices: Numerical and Experimental Investigation”, in K. Watanabe and F. Ziegler (eds.), *Dynamics of Advanced Materials and Smart Structures, IUTAM series*, Kluwer Academic Publishers, Dordrecht, Netherlands. 63-72.
 15. Isalgue A., Torra V. and Lovey F.C. (2002). “Cu-based SMA: Quantifying and Guaranteeing the Time and temperature Dependence on Damping”, in F. Casciati (ed.), *Proceedings of the 3rd World Conference on Structural Control*, John Wiley & sons, Chichester, UK, vol. 2, 363-368.
 16. Saadat S., Salichs J., Noori M., Hoo Z., Davoodi H., Bar-on I., Suzuki Y. and Masuda A. (2002). “An Overview of Vibration and Seismic Application of NiTi Shape Memory Alloys”, *Smart Materials and Structures*, vol. 11, no. 2, 218-229.
 17. SAP 2000. (2003). [Computer Program]. Version 8, Computer and Structures, Inc.
 18. SmartLab, <http://smart.tamu.edu/>.
 19. WIND-CHIME 2004-2007, <http://dipmec.unipv.it/chime/>.

Chapter 2

Algeria, its Seismic Activity and its Monumental Cultural Heritage

2.1 Background of Algerian society

2.1.1 Introduction

Algeria, officially the People's Democratic Republic of Algeria, is a gateway between Europe and Africa, located in North Africa. With its area of 2.381.741 km², it is considered as the largest country of the Mediterranean basin, the second largest on the African continent and the 11th largest country in the world in terms of total area [Wikipedia, 2008]. It has a population of 34.8 million inhabitants (in April 2008) with 85% who live in the Northern zone that forms only 20% of the total area of the country. The main cities are, in addition to the capital Algiers (with 4 millions inhabitants), Oran, Constantine and Annaba. 70% of the population are less than 30 years old where the life expectancy at birth is of 71 years. Algerians national languages are Arabic and Tamazight (language of the original people). French is still the most widely studied foreign language, and most Algerians are fluent in French though it is usually not spoken in daily circumstances.

The hydrocarbon sector is the most flourishing for the Algerian economy. It represents 60% of the budget returns and more than 95% of the exportation gains. Algeria is 5th country in the world for the gas reserves and the 14th one for petrol. It is the 2nd country exporting gas.



Figure 2.1: General views on Algiers.

2.1.2 Ancient history

Algeria has been originally inhabited by Berbers (or Imazighen) since at least 10000 BC. After 1000 BC, the Carthaginians began establishing settlements along the coast. The Berbers seized the opportunity offered by the Punic Wars to become independent of Carthage, and Berber kingdoms began to emerge, most notably Numidia.

In 200 BC, however, they were once again taken over, this time by the Roman Republic. When the Western Roman Empire collapsed, Berbers became independent again in many areas, while the Vandals took control over other parts, where they remained until expelled by the generals of the Byzantine Emperor, Justinian I. The Byzantine Empire then retained a precarious grip on the east of the country until the coming of the Arabs in the eighth century, whose introduction of Islam profoundly altered the character of the area.

By 1517, Algeria was brought into the Ottoman Empire by Khayreddin Barbarossa and Aruj. These brothers established Algeria's modern boundaries in the north of Africa.

On the pretext of a slight to their consul, the French invaded Algiers in 1830 [Horne, 2006]. The conquest of Algeria by the French was long and extremely violent, and it resulted in the disappearance of about one third of the Algerian population [La démographie figure, 2008].

Intense resistance from the population commanded by leaders as Emir Abdelkader, Ahmed Bey and Fatma N'Soumer made the French conquest slow. Indeed, the conquest was not technically complete until the early 1900s when the last Touareg, (in the south), were conquered. Europeans began then to arrive in large numbers, dominating the government and the economy, and leaving the native Muslim population with scant political or economic power

In 1954, the National Liberation Front (FLN) launched the Algerian War of Independence which was a guerrilla campaign. By the end of the war, the newly elected President Charles de Gaulle, understand that the age of the empire was ending, and Algeria got its independence in the 5th of July, 1962. France was responsible for the extermination of 1.5 million Algerians

2.1.3 Geography

Most of the coastal area is hilly, sometimes even mountainous, and there are a few natural harbours. The area from the coast to the Tell Atlas is fertile. South of the Tell Atlas is a steppe landscape, which ends with the Saharan Atlas; further south, there is the Sahara desert. The Ahaggar Mountains, also known as the Hoggar, are a highland region in central Sahara, Southern Algeria. They are located about 1.500 km (932 miles) south of the capital, Algiers and just west of Tamanghasset.

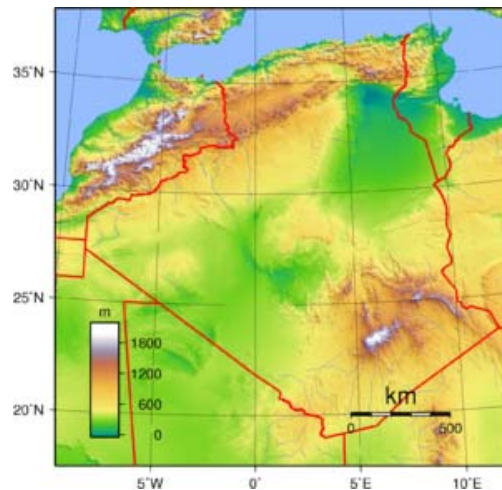


Figure 2.2: Topographic map of Algeria.

2.2 Background on the seismic activity of Algeria

2.2.1 Tectonic and seismotectonic setting

The Northern Algeria area can be briefly described by including from North to South the following main structural domains: the Tell (Tell Atlas), the High Plateaus, the Sahara Atlas (Atlas Mountains system) and the Sahara Platform (Figure 2.3).

The tectonics of this region has been the subject of various studies, such as [McKenzie, 1972], [Tapponier, 1977], [Meghraoui, 1988], [Aoudia and Meghraoui, 1995], [Mickus and Jallouli, 1999] and [Frizon de Lamotte et al., 2000]. To the point, the Tell is part of an Alpine orogen that includes the Spanish Betic Mountains in the west and the Italian Apennines in the east. These Tell mountains consist of a succession of valleys (alluvial basins) and ridges formed by thrusts and folds with an E-W to NE-SW trending parallel to the coastline. The main transport direction of the thrust is S and SE. The High Plateaus zone is situated between the Middle Atlas, the Tell and the Sahara

Atlas, in an elevated region of relatively tabular topography characterized by a thin Meso-Cenozoic cover. The Sahara Atlas belongs to the Atlas Mountains system (Anti, High and Middle Atlas in Morocco, Sahara Atlas in Western Algeria, Aures in eastern Algeria and Tunisian Atlas in Tunisia), a mountain range with a deformed faulted and folded Mesozoic-Cenozoic cover. The Sahara Platform is characterized by no important Meso-Cenozoic deformations. It represents the Southern limit of the studied area.

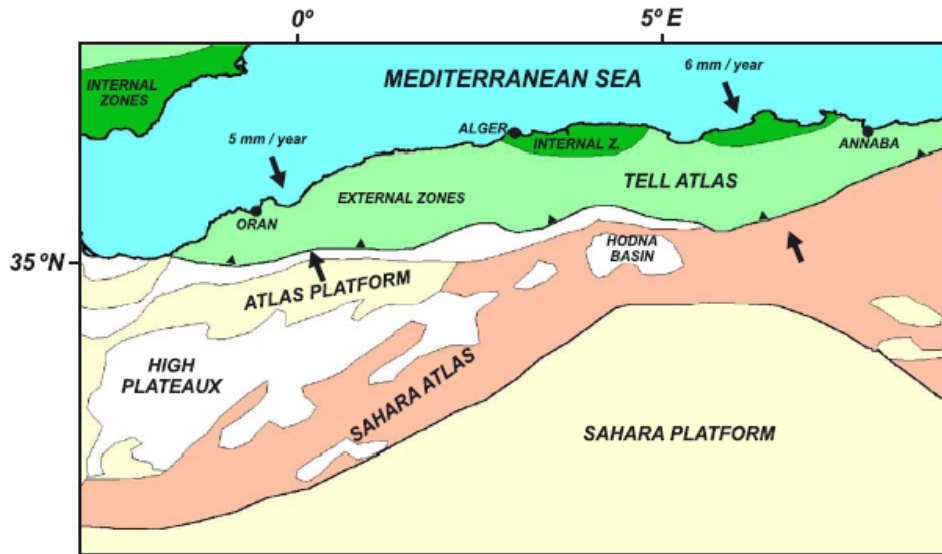


Figure 2.3: Schematic map showing the main tectonic and geologic domains in Northern Algeria (modified from [Frizon de Lamotte et al., 2000]).

The Tell is the eastern part of the Rif-Tell system, an active collision area between the Spain microplate and the Africa and Europe plates, composed of, as in the case of the Betic mountains, internal and external zones with different seismic characteristics. Since the early Cenozoic, this area is under a compressional regime, with a N-S to NW-SE convergence from the late Quaternary. Post-nappes basins present E-W to NE-SW folds and reverse faults. According to [Meghraoui, 1988], [Bezzeghoud and Buforn, 1999] and [Henares

et al., 2003], this active zone absorbs 4-6 mm/year of crustal shortening, with predominant dextral shearing, and it is responsible of the present seismicity.

The main faults, with strike NE-SW, correspond to thrust faults dipping to NW often organized in echelon systems, such as the El Asnam and Tipaza faults [Bezzeghoud and Buforn, 1999] [Aoudia et al., 2000].

2.2.2 Seismic activity of Northern part

The Northern region of Algeria and particularly, its central section is known to be part of an active tectonic structure, where the African plate collides with the Eurasian one. These collisions create a zone of compression, which manifests itself by a series of thrust and normal faults that have been mapped in the area. This region is then considered as the most active seismogenic area in the Western Mediterranean region. Historically, this zone has a rich history of seismicity and had experienced many destructive earthquakes in the past such as the great one of 1365, which destroyed completely the city of Algiers. Reports on other earthquakes that struck Northern Algeria in 1716 (20.000 dead!), 1887, 1910, 1922, and 1934 are also available [CRAAG, 1994]. Several more moderate earthquakes have occurred in that region in recent years [Benouar and Laradi, 1996]. On October 10, 1980, the city of El Asnam (today Chlef) was severely damaged by a magnitude 7.1 earthquake killing roughly 3000 people. The same city had been heavily damaged on September 9, 1954, by a magnitude 6.7 earthquake and killed more than 1000 people. Five other damaging earthquakes, of magnitude 5.4 or higher, were reported in the country in the short period from 1989 to 2000 (such as Ain Temouchent 1999 (5.7) and in Beni Ourtilane 2000 (5.6)). Recently, a magnitude 6.8 earthquake shoot the city of Boumerdes, that killed at least 2278 people in May 21, 2003. A list of important earthquakes in the country from 1365 until now is resumed as Table 2.1.

Table 2.1: List of principal earthquakes in Algeria.

January 03, 1365	:	Algiers was totally destructed, 100 replicas at the night, a part of Algiers was inundate.
February 03, 1716	:	Intensity X at Algiers, 20000 dead.
October 09, 1790	:	Intensity X at Oran, 3000 victims.
March, 1819	:	Intensity X at Mascara, many victims.
March 02, 1825	:	Intensity X at Blida, 7000 dead.
February 09, 1850	:	Intensity VIII at Zemmoura El Ghenzet.
November 22, 1851	:	Intensity VII-VIII at Mascara.
August 22, 1856	:	Intensity IX at Jijel, VIII at Béjaia.
January 02, 1867	:	Intensity X-XI at Mouzaia, 100 dead.
November 16, 1868	:	Intensity IX at Biskra.
January 19, 1885	:	Intensity VIII at N'gaous.
January 08, 1887	:	Intensity VIII at El Mansoura.
November 29, 1887	:	Intensity IX-X, magnitude 6.5-7.5 at Collo, 20 dead.
January 06, 1888	:	Intensity VIII at Mouzaia.
January 15, 1891	:	Intensity X, magnitude 7.5 at Gouraya, 38 dead.
March 11, 1908	:	Intensity VII-VIII at Blida.
August 04, 1908	:	Intensity VIII, magnitude 5.1 at Constantine.
June 24, 1910	:	Intensity VIII-X, magnitude 6.4-6.6 at Sour El Gouzlène, 30 dead.
August 06, 1912	:	Intensity VI, magnitude 5.3 at Oued Marsa.
August 25, 1922	:	Intensity IX-X, magnitude 5.1 at Bordj Abou Hassan, 2 dead.
March 16, 1924	:	Intensity IX, magnitude 5.6 at Batna, many dead.
November 05, 1924	:	Intensity VIII, magnitude 5.0 near Algiers.
June 10, 1925	:	Intensity VIII near Boghar.
August 24, 1928	:	Intensity VIII, magnitude 5.4 at Oued Rhiou.
August 15, 1931	:	Intensity VIII, magnitude 4.9 at Djebel Dira.
September 07, 1934	:	Intensity VII-IX, magnitude 5.0 at El Abadia, 0 dead.

September 19, 1935	:	Magnitude 5.1 near Chetaibi.
February 10, 1937	:	Intensity VIII, magnitude 5.4 near Guelma.
April 16, 1943	:	Intensity IX, magnitude 4.0 near El Mansoura, many victims.
February 12, 1946	:	Intensity VIII-IX, magnitude 5.6 at the Hodna mountain.
August 06, 1947	:	Intensity VIII-IX, magnitude 5.3 at Oued Hamimine, many victims.
March 13, 1948	:	Intensity VIII, magnitude 4.9 at Asla, 1 dead.
February 17, 1949	:	Intensity VIII, magnitude 4.9 near kherrata.
April 20, 1950	:	Intensity VI-VIII, magnitude 5.1 near Aflou.
July 05, 1953	:	Intensity VIII, near Ain Bessam.
August 29, 1953	:	Intensity VIII-IX at the Hodna mountain, 1 dead.
September 09, 1954	:	Intensity X, magnitude 6.7 at Chlef, 1243 dead, and 20000 destructed house.
September 10, 1954	:	Intensity IX, magnitude 6.2, replica at Chlef.
February 04, 1955	:	Intensity VIII, replica at Chlef.
May 08, 1955	:	Intensity VIII at Béni Haoua.
June 05, 1955	:	Intensity VIII, magnitude 5.7 at Béni Rached.
February 14, 1956	:	Intensity VI-VII, magnitude 5.9 at Bordj Abou Hassan.
June 28, 1957	:	Intensity VII, magnitude 5.0 at Sendjas.
May 24, 1959	:	Intensity VII-VIII, magnitude 5.5 at Zemmoura El Ghenzet.
November 07, 1959	:	Intensity VIII, magnitude 5.5 at Bou medfa.
February 12, 1960	:	Intensity VIII-IX, magnitude 5.6 at Béjaia, 264 dead, 1000 destructed house, 112 injured.
February 21, 1960	:	Intensity VIII, magnitude 5.6 at Melouza (M'sila), 47 dead and 88 injured.
December 02, 1961	:	Magnitude 5.5 at Annaba (at sea).
September 04, 1963	:	Magnitude 5.7 near Sétif, 1 dead and 100 injured.
January 01, 1965	:	Magnitude 5.5 at M'Sila, 5 dead, 24 injured and

- 1304 destructed house.
- July 13, 1967 : Intensity VII, magnitude 5.1 near Sig, 10 dead and 15 injured.
- February 28, 1968 : Intensity VIII, magnitude 4.9 at El Alen, 1 dead and 4 injured.
- February 05, 1971 : Magnitude 5.9 at In Aménas.
- February 23, 1971 : Intensity VIII, magnitude 4.9 at Rouina.
- February 25, 1971 : Magnitude 5.4 at Asla.
- March 11, 1973 : Magnitude 5.7 at the cost, near Tènes.
- November 24, 1973 : Intensity VII, magnitude 5.1 at Bordj Bou-Arreidj, 4 dead, 50 injured.
- November 25, 1973 : Intensity VII, magnitude 4.9 at Guenzet.
- July 28, 1974 : Intensity VII, magnitude 5 at Sétif.
- November 09, 1974 : Intensity VIII, magnitude 4.1 at the south of Béjaïa.
- July 11, 1975 : Intensity VIII, magnitude 5 at Sétif, 1 dead, 18 injured.
- October 10, 1980 : Intensity X to XI, magnitude 7.5 at Béni Rached (Chlef), 2633 dead, 8369 injured, 70% of habitation was testrected.
- October 10, 1980(1 : Magnitude 6.5 at Béni Rached.
heure later)
- November 08, 1980 : Magnitude 5.7 at Béni Rached.
- April 19, 1981 : Magnitude 4.8 at Oran, Arzew.
- June 30, 1981 : Magnitude 4.5 at Ain Bénian, chéraga, Staoueli.
- May 23, 1982 : Magnitude 4.5 at Bordj Ménaiel.
- November 15, 1982 : Magnitude 4.8 in Tiaret region.
- September 28, 1983 : Magnitude 4.4 in Teniat El Had region.
- November 10, 1983 : Magnitude 4.5 at Relizane region.
- December 07, 1983 : Magnitude 4.5 at Algiers, Staoueli, Zéralda.
- December 20, 1983 : Magnitude 4.7 at Constantine, Skikda.
- June 15, 1984 : Magnitude 4.5 at Gouraia, Tènes.
- October 05, 1984 : Magnitude 4.5 at Oum El Bouaghi.

March 05, 1985	:	Magnitude 4.8 at Tiaret region.
September 07, 1985	:	Magnitude 4.7 at Relizane, Ech-Chellif.
October 27, 1985	:	Intensity VIII, magnitude 5.9 at Constantine, 10 dead, 300 injured.
January, 1986	:	Magnitude 4.6 at Blida, El Affroun, Mouzaia.
March 28, 1986	:	Magnitude 4.5 at Constantine.
May 20, 1986	:	Magnitude 4.8 at Batna, Constantine.
November 04, 1986	:	Magnitude 4.5 at Ain Defla.
December 19, 1986	:	Magnitude 4.7 at Blida, Algiers.
January 26, 1987	:	Intensity VI-VII at Bordj Bounaama (Tissemsilt), 1 dead, number of injured, some houses gravely damaged.
February 28, 1987	:	Intensity V, magnitude 4.6 at Tissemsilt.
July 24, 1987	:	Intensity V, magnitude 4.3 at Médéa region.
October 31, 1988	:	Intensity VII, magnitude 5.4 at El-Afroun, Boumedfâa, numerous havocs (schools, habitations, and hospitals), more than 500 families without shelter, and 3 injured, 0 dead.
February 12, 1989	:	Intensity V, magnitude 4.9 at Algiers and Blida.
October 29, 1989	:	Intensity VIII, magnitude 6.0 at Chenoua mount (Tipaza), 22 dead.
August 18, 1994	:	Intensity VII, magnitude 5.6 at Mascara.
September 04, 1996	:	Intensity VII, magnitude 5.7 at Algiers.
December 22, 1999	:	Intensity VII, magnitude 5.8 at Aint-Temouchent, 28 dead.
November 10, 2000	:	Intensity VII, magnitude 5.4 at Béni-Ouartilane (Tizi-Ouzou), 2 dead.
May 21, 2003	:	Intensity X, magnitude 6.8 at Boumerdes, 2778 dead.

The analysis of earthquake epicentres' distribution during the last three centuries leads to the conclusion that earthquakes in Algeria occur mostly in some Tell cluster zones. However, a few earthquakes appeared in the High Plateaus and across the Sahara Atlas range (Figure 2.4). According to [Aoudia et al., 2000], the seismicity analysis also shows that the seismogenic areas are located in the vicinity of the Quaternary Basins. These tectonic zones, that coincide with the areas in which there are Neogene and Quaternary deposits, extend to the Messeta Basin (region of Oran) in the Western Tell, in the centre to the Mitidja Basin (Tipaza–Algiers) close to the Atlas blideen (or Blidean Atlas, from the Blida city), and extends to the Soumam, Constantine and Guelma Basins in the eastern part, and to the Hodna Basin in the southeast.

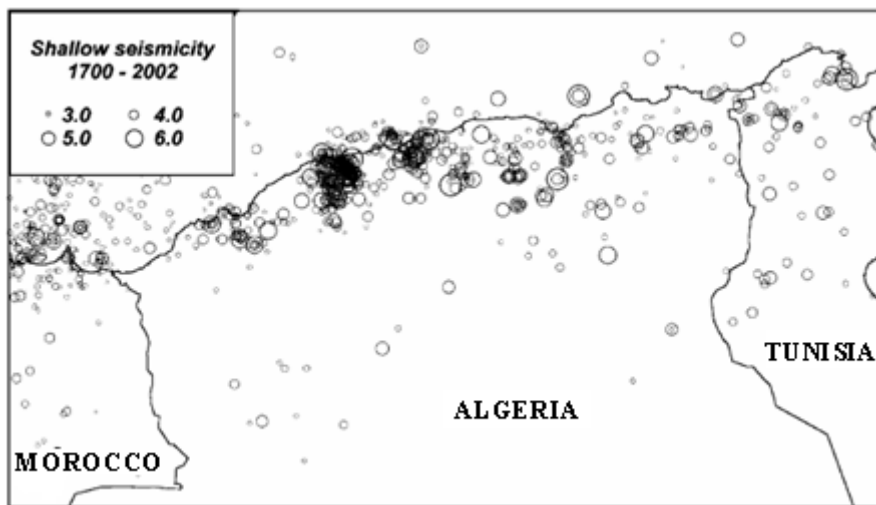


Figure 2.4: Past earthquakes in Algeria (1700-2002).

2.2.3 Network of seismograph stations [Benouar, 1994]

Earthquake instrumental recordings in the North African region started in the 19th century, with very limited instruments by today's standards. The first instrument in the region was installed in Bouzareah (Algiers) by 1917. Most of seismographic stations covering the Maghreb countries were operating in

Southern Europe. The distribution of seismograph stations that operated in the North Africa and neighbouring regions before 1955 are shown in Figure 2.5.

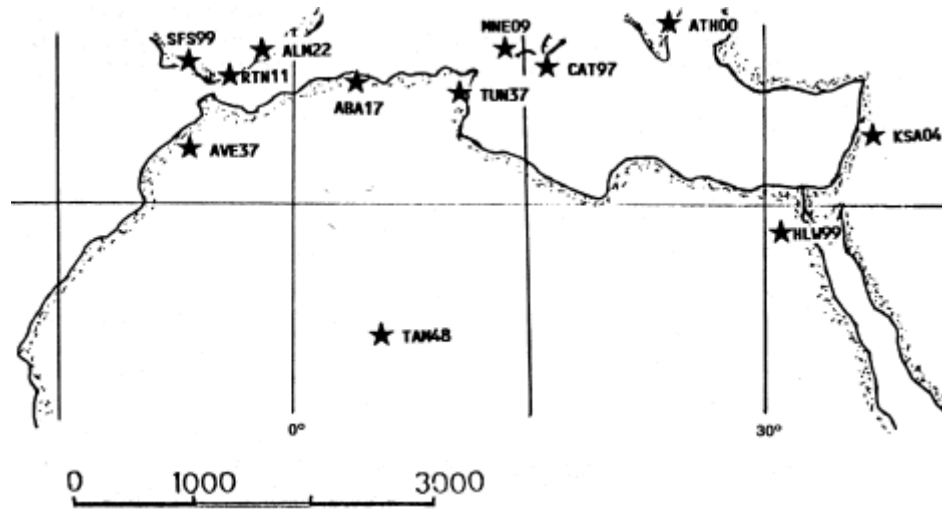


Figure 2.5: The distribution of seismograph stations in North Africa and adjacent areas before 1955.

During the period 1899-1919, the first instruments installed were Milne seismographs, most of them un-damped, short period (10-20s), low magnification (10-20). These instruments had no precise timing. The Milne instruments mainly recorded surface waves and were unable to report consistent pairs of P and S phases, which prevent the estimation of origin times and thus reliable north-south location. For some major events, instrumental locations seem to be correct to a few tens of kilometres, which were enough to estimate the overall area of an event, but sufficiently gross to be adopted over macro-seismic epicentres.

During the period 1920-1960 and particularly in the early years, the un-damped Milne pendulums were gradually replaced by a growing number of shorter-period damped instruments. The new material had higher sensitivity which gave more reliable readings of P and S phases, thus more precise calculations. This

period has seen an improvement of the aptitudes of the seismograph station network in the region, particularly the installation of local stations in Tamanrasset (1948), Relizane (1955) and Setif (1957).

Since 1961, with the installation of the World-Wide standard Seismograph Network (WWSSN), the quality of the data, both in accuracy and in the number of earthquake records, improved remarkably. The introduction of advanced instruments and the improvement of location techniques (particularly computer determinations) were clearly exhibited by the number of earthquakes reported, by the good agreement in the epicentral position given by different seismological stations and also by the increasing number of source parameters made available. This period had also been marked by the development of national seismographic networks in Algeria, where the number of operating stations increases from 1 station in 1917, to 2 in 1948, to 4 in 1957, to 9 in 1990 and to 200 in 2003.

Following the catastrophic earthquake of El-Asnam in 1980, the Algerian authorities lunched, in 1982, a project for the installation of a national telemetry seismograph network in the Northern part of the country. The installation of the instruments, which were received by 1986, has been in progress since then by the "Centre of Research in Astronomy, Astrophysics and Geophysics" (GRAAG) which was also in charge of exploitation of the network. This national network was subdivided into four regional networks: Oran, Chlef, Algiers and Constantine. The four regional networks were linked to the main station at Bouzereah (Algiers). In 1987, the "Centre National de Recherche Appliquée En Genie Parasismique (C.G.S)" have been created with the main missions and objectives to perform investigation and research activities in the field of seismic risk reduction, to build its specific research and testing laboratories, in addition to aid and assist the engineering offices and concerned institutions. The two centres (GRAAG and CGS) were equipped then with an important number of accelerograms that have been installed on free field and in special buildings.

Now, the plan is to establish a network of 335 accelerograph-stations. In 2003, 200 stations including 40 digital recorder stations were already installed.

2.2.4 An overview of the Algerian seismic codes

The first seismic code in Algeria was developed by the French in 1955 after the 1954 Orléansville (El-Asnam and later Chlef) earthquake [CTC]. That very succinct code (called “Recommendations AS 55”) was used more or less for the reconstruction in the stricken region, and divided the overall country in two seismic zones: “A” of low seismicity and “B” for high seismic activity (the Northern part from Moroccan to the Tunisian borders). These regulations were revised in 1969 where more general seismic rules inspired from the modern French regulations “PS 69” were applied. In 1976, the CTC (Organisme National de Contrôle Technique de la Construction: National Organism of technical control of construction) had contracted an agreement with Stanford University, in order to set up a new “Draft Code” which takes into account more accurately the specific parameters of Algerian construction (microzoning map, local construction techniques...). This draft code was ready in 1979 and was in discussion and enrichment at the level of CTC technical staff when 10.10.1980 El Asnam Earthquake took place. This event provided many interesting lessons that have been taken into account in the new code. That is why the code had been enacted definitely only in 1983 under the title “Algerian Earthquake Design Regulations 1981 (RPA 81-version 1983)”. The RPA 88 version have been edicted with mandatory application following the legislative and regulatory aspects that were taken into account by two 1985 decrees concerning disaster reduction and emergency at global level. The actual version of the Algerian seismic code was published in 1999 (RPA 99) under the American model. It prescribes the requirements for seismic design of ductile structures and the use of equivalent static and dynamic analyses.

The RPA 99 code divided the territory in 4 zones according to their seismic intensity:

Zone 0: Negligible seismicity

Zone 1: Low seismicity

Zone 2: Moderate seismicity

Zone 3: High seismicity.

Figure 2.6 shows the map of seismic zones in Algeria.

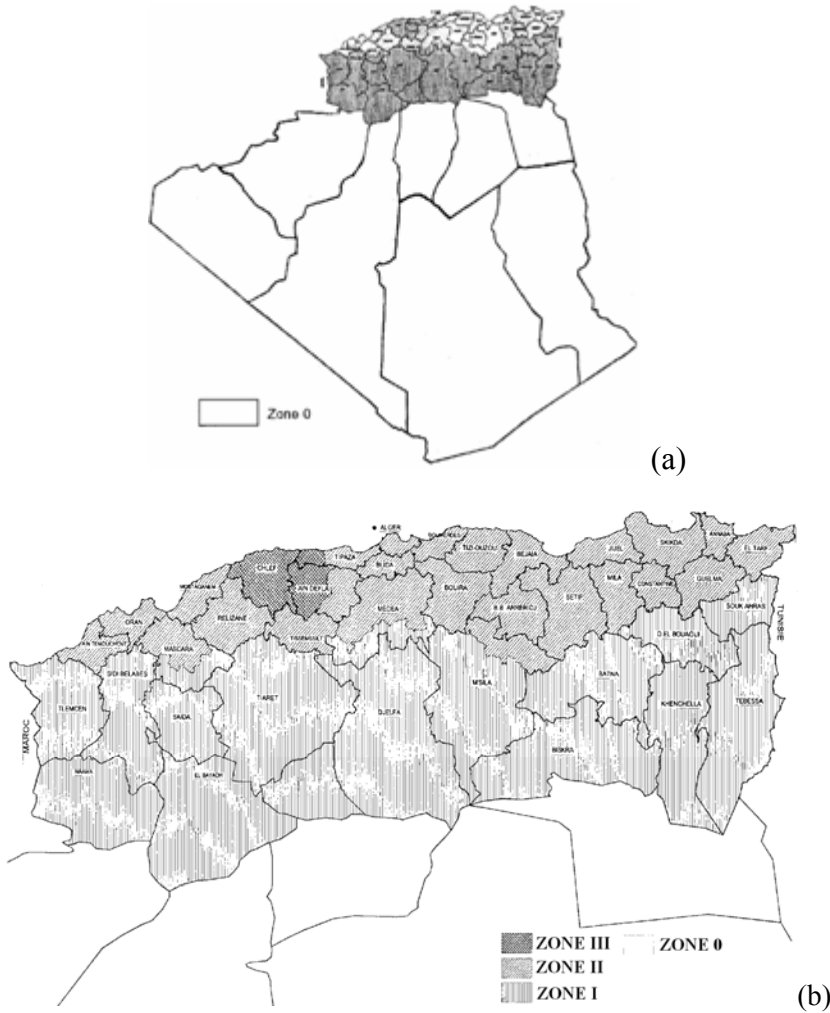


Figure 2.6: Seismic zoning map in Algerian: (a) national territory, (b) the Northern part.

The code gives also a degree of safety to a structure depending on its importance for the community. Four groups were proposed.

Group 1A: Structures of vital importance: Hospitals, electrical centrals, airports, military caserns, dams...

Group 1B: Structures of great importance: public buildings, universities, mosques...

Group 2: Structure of moderate importance: habitation and administrative buildings, sportive constructions...

Group 3: structures of low importance: provisory constructions, structures for non important properties...

The coefficient of peak ground acceleration (PGA), A , is given depending on the group of importance and the corresponding seismic zone (see Table 2.2).

Table 2.2: Coefficient of the peak ground acceleration.

Group	Zone		
	1	2	3
1A	0.12	0.25	0.35
1B	0.10	0.20	0.30
2	0.08	0.15	0.25
3	0.05	0.10	0.15

Also, the code takes in account the soil nature and its mechanical properties. It classifies it depending on the speed of the shear wave's propagation.

Rock soil: $V_s > 800$ m/s

Firm soil: $V_s > 400$ m/s from 10 m of depth.

Soft soil: $V_s > 200$ m/s from 10 m of depth.

Very soft soil: $V_s < 200$ m/s in the first 20 m.

Following the 2003 Boumerdes earthquake, an updated edition of the RPA99 code was elaborated, taking into consideration the lesson learned from that disaster. Several modifications were seen in the updated and accurate version, some important one are sited in the following section.

According to the original RPA 99, Algiers was located in the seismic zone 2, where the peak ground acceleration (PGA) value for a design earthquake corresponding to this zone was 0.15g for residential apartment buildings. However, according to the information provided by the Algerian National Earthquake Engineering Research Center (CGS) [CGS], the recorded peak accelerations in the east part of Algiers during the May 21, 2003 earthquake were on the order of 0.34g. In the updated version, the seismic zone for Algiers was upgraded to zone 3, corresponding to the PGA value for residential apartment buildings of 0.25g. In the modified code version, a more accurate micro-zoning map of the country was provided, dividing zone 2 (of moderate seismic activity) into zone 2A (with PGA of 0.15g) and zone 2B (with PGA of 0.20g)- for the same example of residential apartment buildings-. As the case of Algiers, other cities and departments were upgraded according to their new seismic activity. Figure 2.7 gives the new micro-zoning map, where table 2.3 shows the updated PGA factors.

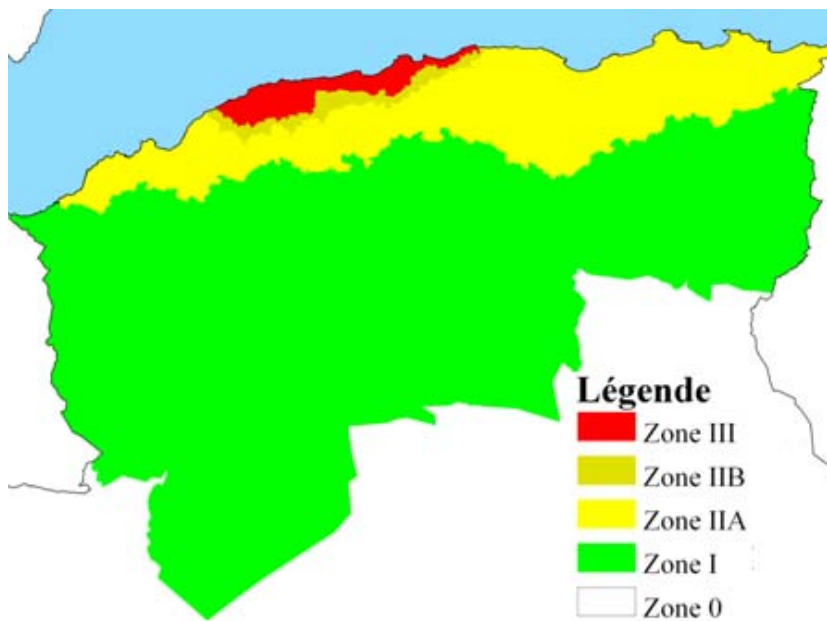


Figure 2.7: The updated seismic zoning map.

Table 2.3: Coefficient of PGA acceleration from the modified Algerian code.

Group	Zone			
	1	2A	2B	3
1A	0.15	0.25	0.30	0.40
1B	0.12	0.20	0.25	0.30
2	0.10	0.15	0.20	0.25
3	0.07	0.10	0.14	0.18

The new version increased also the steel minimum area for reinforced concrete structures. Consequently, the majority of RC structures in moderate seismic region were reinforced with that minimum steel area. Additionally, it corrects also the previous technical errors in the previous code. Note for example that the RPA99 code allowed the use of a thimble at the basement of columns for easier framework (that caused a rupture joint), where it was strictly forbidden in the modified version (see Figure 2.8).

**Figure 2.8:** Thimble at the basement of columns used for easier framework.

2.2.5. Examples of major damaging earthquakes in Algeria

Regarding their resulted huge number of victims, three of the most memorised earthquakes for Algerians are briefly presented here. The first is the more recent one, 2003, where the traces are still clear on the struck city and its people. The second one happened 28 years ago (1980), and with its catastrophic results, formed the base of the regulations in the Algerian para-seismic code. The third one is a historical earthquake (1716). We are speaking about:

- the May 21, 2003 Boumerdes earthquake: Intensity X, magnitude 6.8, 2278 dead, 11450 injured, 182000 of people lost their house.
- The October 10, 1980 Al-Asnam earthquake: Intensity X to XI, magnitude 7.5, 2633 dead, 8369 injured, 70% of habitation was testrected.
- The February 3, 1716 Algiers earthquake: Intensity X, 20000 dead.

2.2.5.1 The May 21, 2003 Boumerdes earthquake

An earthquake of magnitude 6.8 shook Algeria at 18:44:19 UTC on 21 May 2003 and caused damage in five provinces in the North-Central section of the country (Figure 2.9) [Bendimerad, 2004]. This zone included 3-4 millions inhabitant, where the population was deeply traumatized. According to the records, the epicenter was located in the Mediterranean Sea at 36.89°N, 3.78°E, approximately 4 km from the coast between from the cities of Zemmouri and Boumerdes (about 50 km east of the capital Algiers). The hypocentral depth was estimated as 10 km. The maximum intensity of the earthquake according to the Modified Mercalli Intensity scale was X. The earthquake was followed by several aftershocks (at least 240), including two events of magnitude 5.8.

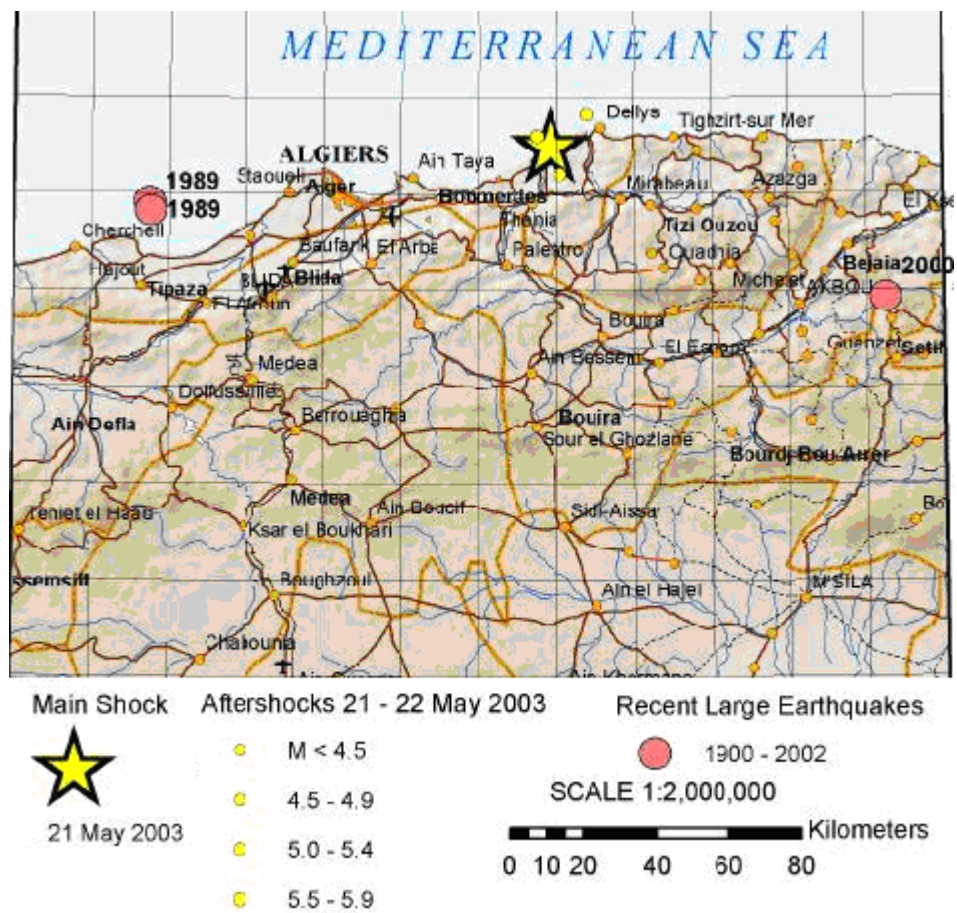


Figure 2.9: Region of Algiers - Boudjaja - Dellys that was affected by the earthquake.

The focal mechanism of the May 21 earthquake corresponds to a northeast-striking thrust fault called Zemmouri fault (identified for the first time after the earthquake), as shown in Figure 2.10.

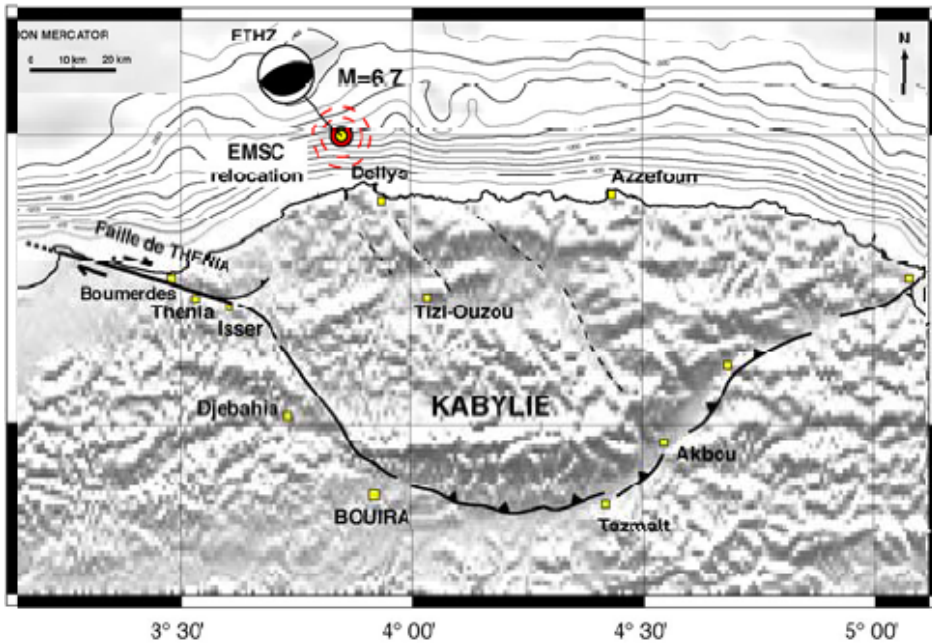


Figure 2.10: Map showing faults in the earthquake-affected region.

87 stations including 29 digital stations were set in the region where the earthquake detected during the May 21, 2003 Boumerdes Earthquake. 14 mobile stations were temporarily set around the near field and the heavily damaged areas to monitor the after shock. Figure 2.11 shows a map of the region touched by the Boumerdes earthquake with the surrounding record station.

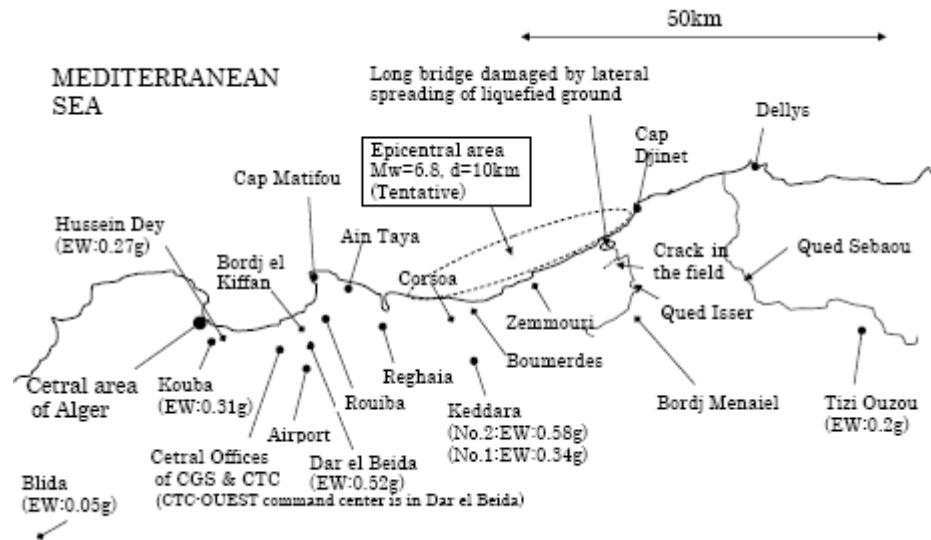


Figure 2.11: Algiers, Boumerdes and Blida region with the surrounding recording stations.

The closest station, located 20 km away from the epicenter at the Keddara Dam, recorded the maximum acceleration of 0.58g in the E-W direction; the station (Keddara Dam 2) was located at a soil site. Another station, located only 100 m away at a rock site (Keddara Dam 1), recorded the maximum acceleration of 0.34g (also in the E-W direction). This trend, attributed to site effects, is characteristic for other four stations as well. It should be also noted that modern reinforced concrete buildings in the eastern part of Algiers located in the soft soil area were severely affected by the earthquake, while the older masonry buildings located in the part of the city supported by hard strata, were less affected, in spite of their high seismic vulnerability.

The E-W acceleration component was consistently larger than the N-S component; for example, the station Keddara Dam 2 that recorded the maximum acceleration of 0.58g in the E-W direction, recorded a significantly lower N-S acceleration of 0.22g. The maximum recorded vertical acceleration

was 0.35g (Keddara Dam 2 station), however some field observations have reported the vertical accelerations of 1.0g or higher in the epicentral region [EERI, 2003].

Soil liquefaction and lateral spreading were observed in the epicentral region, especially in the area near the Isser River. Tension cracks caused by lateral spreading in the epicentral region are shown in Figure 2.12.



Figure 2.12: Lateral spreading in the epicentral area of the May 21, 2003 earthquake close to the Zemmouri-El-Bahri port.

The areas affected by the earthquake are located along a shoreline strip 100 km long and about 50 km wide. This strip encloses a few highly populated cities, including Algiers and Boumerdes. The earthquake caused 2278 deaths and 11000 injuries and left over 180000 people homeless. The total economic loss was estimated to be around \$6.5 billion (approximately 10% of the national GDP). The earthquake most adversely affected buildings in general, and housing construction in particular (Figure 2.13). In total, about 182000 housing units (apartments and private houses) were damaged in the earthquake, out of which more than 19000 collapsed or were uninhabitable after the earthquake. Industrial facilities located in the earthquake affected area also suffered

damages to buildings and equipment. Over 50% of the health care facilities and more than 550 schools in the earthquake affected area were destroyed or severely damaged. The water distribution system was impaired after the earthquake, and the distribution of water in the affected area was ensured by mobile cisterns and individual containers. The repair costs for drinking water systems were estimated to be over \$40 million.

Transportation systems, especially bridges, were also affected by the earthquake, with the estimated repair cost of around \$37 million. The Port of Algiers was affected by the earthquake, and several piers were damaged due to liquefaction.

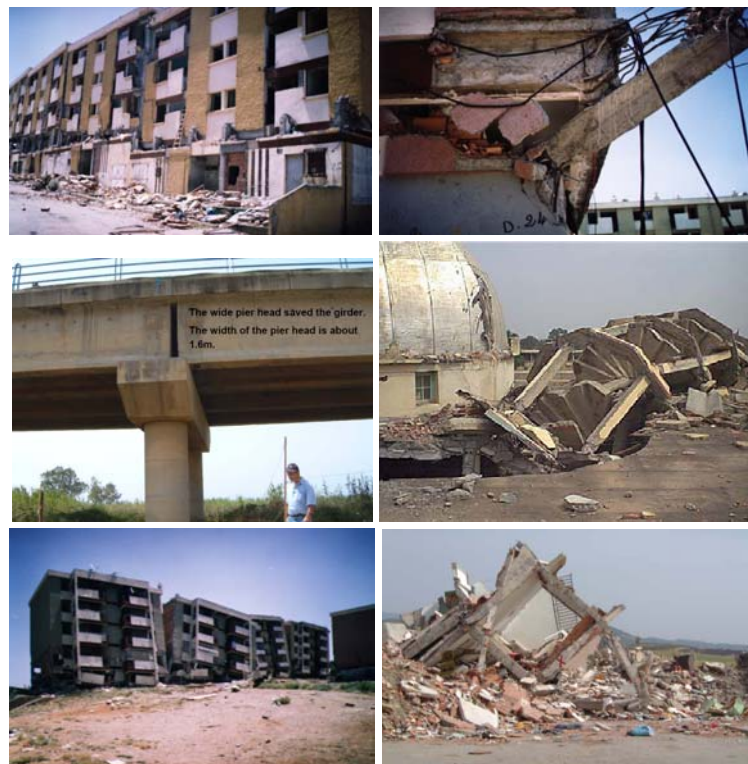


Figure 2.13: Catastrophic effect caused by Boumerdes earthquake.

2.2.5.2 The October 10, 1980 Al-Asnam earthquake

On Friday 10 October, 1980 at 13:24:24, a destructive and violent earthquake struck the El-Asnam and its surrounding villages affecting a rather densely inhabited region [Benouar, 1994]. Almost all the seismological stations operating at that time recorded the main shock. Its magnitude was re-calculated at 7.4 (± 0.3). The epicenter was located at Beni Rached, 15Km east of El-Asnam, the focal depth of the earthquake was 10 km and the approximate duration 40 seconds (see Figure 2.14). The main shock was followed by a long series of aftershocks, during several months, with some of them strong enough to add further damage and casualties among the population. This earthquake was reported to the ISC by 514 seismological stations.

The main shock and its largest aftershock caused the death of at least 3000 people, injuring more than 8500 and making about 480000 homeless. It damaged about 60000 housing units in the whole affected area, among them, 30000 units were destroyed, in addition to the destruction of numerous public buildings, major stores, industrial installations, lifeline systems, transport and commercial facilities, and public and hydraulic works in the whole affected zone.

This earthquake caused considerable economic losses to Algeria, had large socio-economic and psychological impacts on the region. The total cost of the damage has been estimated at around 5 billions U.S. Dollars. The zone of greatest structural damage, loss of life and ground deformations was confined within the narrow area including El-Asnam, Sendjas, Zeboudja, Al-Abadia, Oued Fodda, Beni Rached, Al- Attaf and Oum Drou.

In El-Asnam itself, as much as 1500 people perished, 4000 were injured and about 88000 rendered homeless; as much as 20% of the building stock was completely destroyed, 60% severely damaged and the remained were either slightly affected or survived without any damage.

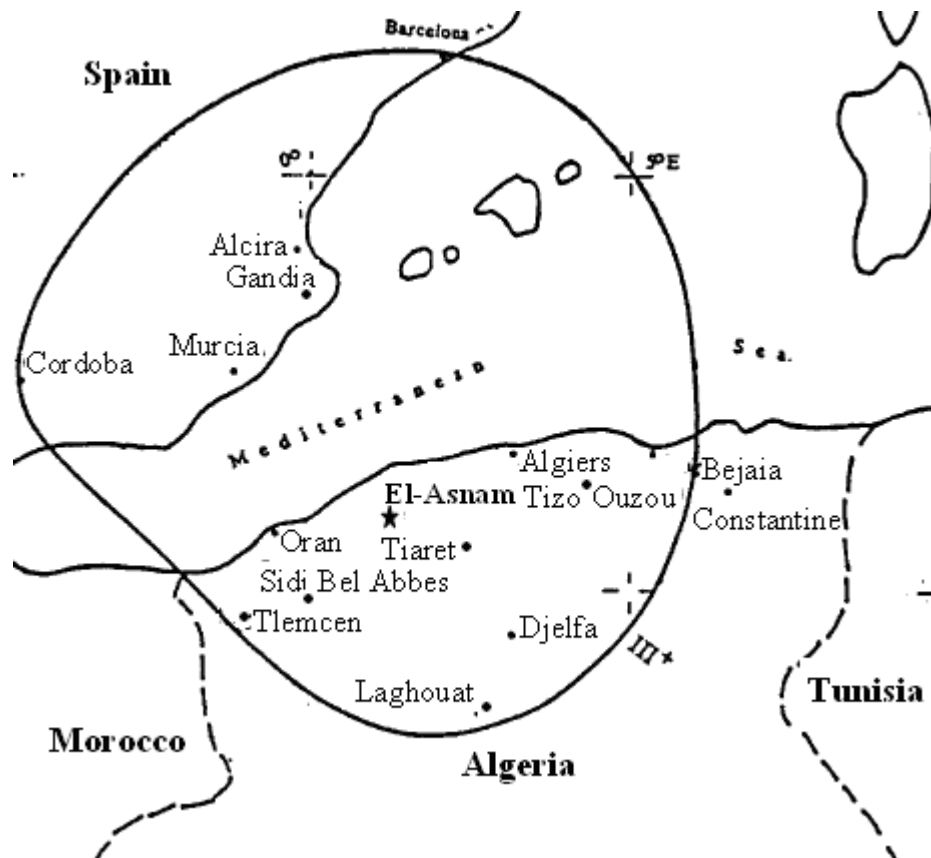


Figure 2.14: Map of the felt area of El-Asnam, October 10, 1980 earthquake.

Several modern structures suffered pancake collapse in which several hundred people were killed under their debris. In a radius of about 40 Km around El-Asnam, most damage consisted of the collapse of various structures, loss of life and ground deformations. Khemis Miliana 60 km away was the last town where damage could be clearly seen. In the capital Algiers 179 km distant, the shock was strong enough to make people panic and flee from their homes to the streets, 16 buildings in the Casbah of Algiers, seriously cracked and threatening of collapse, were evacuated. Also in Blida, Tiaret, Freneda and Mostaganem, the shaking caused considerable panic among the inhabitants, but no damage were

reported. In Spain, at Murcia, Gandia, Alcira, Valencia and Ibiza Island, the earthquake caused panic movements of the population and slight damage to buildings. The radius of perceptibility was fairly large and the shaking was felt as far east as Bejaia, south as Laghouat, west as Tlemcen and north as Cordoba and Barcelona in Spain. There is no evidence that the shock was felt in Morocco.

The earthquake was associated with an extensive ground deformations, it is the first known event to produce large surface rupture in the Western Mediterranean area. One of the remarkable effects of this earthquake is that an equivalent amount of both extensional and compressional deformations was observed which implies a rather complex deformation mechanism. Damage to the surface as a result of the shaking was extensive, disastrous and varied. Much land was sunk and some was uplifted, a lake was formed, the flow of springs was altered, water levels in wells were modified and the courses of Oued Chellif and Oued Fodda were changed. Fitures, large cracks, landslides, sand blows and extrusions of various kinds were common. The manifestation of the earthquake itself was a visible surface fault passing very close to Oued Fodda. It was about 3 km west Oued Fodda, where the fault cut the Algiers - El-Asnam railway line and Ouel Chlef bed. Among the most impressive sights left behind by the earthquake were the bending of railway lines and the uplifting and overturning of the freight train that was crossing the fault at the moment the shaking occurred.

The main reasons of the damages are:

- Use of the “vide sanitaire” (a short crawl space) which is used for water, gas, sewage and ventilation conduits, supported by short columns.
- Use of irregular building configurations with severe discontinuities in mass, stiffness and ductility.
- Use of very heavy roofs.
- Use of long heavy cantilevers.
- Use of thermal, expansion construction gaps without proper separation between adjacent parts of the building.

- Poor inspection and construction techniques.
- Inadequate building maintenance.
- Use of strong beams and weak columns.

2.2.5.3 The 1716 Algiers earthquake

On February 3, 1716, at 9h 45m (local time) an intensity X destructive earthquake shook the city of Algiers and its adjacent regions. As it was reported, around 200 houses collapsed, the large mosque was cracked, even the country houses (administrative builds) suffered from considerable damages and some of them were thrown to the ground [Abdessemed-Foufa, 2005]. About 3 km far from the city, the ground had large openings. Large soil deformations and liquefaction were observed in the south west of the city. Many fires burst and increased the damage. The number of foreshocks was evaluated to 24 and lasted until June with such a violent commotion on February 26. The inhabitants left the city and settled in tents in the countryside during the nine following months. The number of the victims reached 20.000, most of them buried under the debris. All these informations have been reported by the different sources: [Delphin, 1922], [Gazette de France, 1716] and [Comelin, 1720] historical studies [Chesneau, 1892], [Tassy, 1830] and [Grammont, 1887] and recent studies [Saidouni, 1985] and [Harbi, 2005].

The recorded damages are grouped as the following three types:

- Total collapse of the houses: Two hundred (200) houses collapsed, most of the dwellings were ruined and part of the city was thrown to the ground. The country houses or house of the fahs around Algiers collapsed completely at a distance of about 3 km around the city.
- Destruction of the walls: Many houses were damaged and the great Mosque of the city presented several cracks and repairs were conducted to the damaged houses. It was reported that the aftershock of 26 February added damaged to most of the houses, which did not collapse totally after the main shock.

- Rupture of floors: It was revealed that many floors of the houses collapsed following the earthquake. Comelin [Comelin, 1720] reported on the event: “...The house of the ambassador of France was one of the most beautiful of Algiers. It had three floors before the last earthquake, now only two floors remains”.

2.3 Archaeological sites and monuments of Algeria

2.3.1 Introduction

Algeria is rich in prehistoric memorials of human occupation, especially in megalithic remains, of which nearly every known kind has been found in the country. Numerous flints of palaeolithic type have been discovered, notably at Tlemcen and Kolea. Near Djelfa, in the Great Atlas, and at Mechra-Sfa (“ford of the flat stones”), a peninsula in the valley of the river Mina not far from Tiaret, are vast numbers of megalithic monuments. Notable among the prehistoric cultures of the area is the Capsian culture, whose shell-mounds are found throughout the north.

In the Qabr-er-Rumia (“grave of the Roman lady”, “Roman” being used by the Arabs to designate strangers of Christian origin) the Medrasen, and the Jedars, Algeria possesses a remarkable series of sepulchral monuments.

The Qabr-er-Rumia (best known by its French name, Tombeau de la Chrétienne, tradition making it the burial-place of Florinda, la Cava Rumía, the beautiful and unfortunate daughter of Count Julian) is near Kolea, and is known to be the tomb of the Mauretanian king Juba II and of his wife Cleopatra Selene, daughter of Mark Antony and Cleopatra, queen of Egypt. It is built on a hill 230 m above the sea. A circular stone building surmounted by a pyramid rests on a lower platform, 64 m square. Originally the monument was about 40 m in height, but it has been wantonly damaged. Its height is now 30.7 m: the cylindrical portion 11.1 m, the pyramid 19.6 m. The base, 60 m in diameter, is ornamented with 60 engaged Ionic columns. The capitals of the columns have disappeared, but their design is preserved among the drawings of James Bruce,

the African traveller. In the centre of the tomb are two vaulted chambers, reached by a spiral passage or gallery 2 m. broad, about the same height and 149 m long. The sepulchral chambers are separated by a short passage, and are cut off from the gallery by stone doors made of a single slab which can be moved up and down by levers, like a portcullis. The larger of the two chambers is 43 m long by 3.4 m broad and 3.4 m high. The other chamber is somewhat smaller. The tomb was early violated, probably in search of treasure. In 1555 Salah Rais, pasha of Algiers, set men to work to pull it down, but the records say that the attempt was given up because big black wasps came from under the stones and stung them to death. At the end of the 18th century Baba Mahommed tried in vain to batter down the tomb with artillery. In 1866 it was explored by order of the emperor Napoleon III, the work being carried out by Adrien Berbrugger and Oscar Maccarthy.

Medghasen is a monument similar to the Qabr-er-Rumia, but older. It was built about 150 B.C. as the burial-place of the Numidian kings, and is situated 56 km southwest of Constantine. The form is that of a truncated cone, placed on a cylindrical base, 60 m in diameter. It is 18 m high. The columns encircling the cylindrical portion are stunted and much broader at the base than the top; the capitals are Doric. Many of the columns, 60 in number, have been much damaged. When the sepulchral chamber was opened in 1873 by Bauchetet, a French engineer officer, clear evidence was found that at some remote period the tomb had been rifled and an attempt made to destroy it by fire.

The Jedars (Arabian “walls” or “buildings”) is the name given to a number of sepulchral monuments placed on hill-tops. A rectangular or square podium is in each case surmounted by a pyramid. The tombs date from the 5th to the 7th century of the Christian era, and lie in two distinct groups between Tiaret and Frenda. Frenda, which has largely preserved its old Berber character, has numerous dolmens and prehistoric rock sculptures close by.

Algeria contains many Roman remains besides those mentioned and is also rich in monuments of Saracenic art. For a description of the chief antiquities see the

separate town articles, including, besides those already cited, Lambessa, Tebessa, Tipasa and Timgad.

Since the author is originated from the region of Tlemcen (situated in the north-west of Algeria) and because of the richness of that region in monuments and archaeological sites, the next section is presented as a studied case dedicated to the description of the historical heritage of Tlemcen. The idea is to introduce the monuments of the region so that they will be subject to future studies with applying the different techniques presented in the next chapters. Note that the advisor suggested to apply retrofitting techniques to El-Ourit Bridge when he visited the country on May 2008, that's why a detailed presentation of that bridge is drawn at the end of the next section.

2.3.2 The city of Tlemcen

Located 170 Km from Oran, 600 Km from Algiers, Tlemcen is one of Algeria's great Islamic cities, where more than 80% of the Islamic heritage is there. It flourished as an Arab sultanate from 1282 until 1553 when it became part of the Ottoman Empire. The city is still set amidst olive groves and vineyards in one of Algeria's most beautiful regions and is redolent of its traditional heritage, marked by vestiges of Islamic architecture and the memories of the many great Algerian scholars and saints who lived and died there.

There is evidence of prehistoric habitation by cave dwellers in the area of Tlemcen. There are also remains of a Roman military encampment. The first Arab-Islamic settlement on the site was established in the 8th century by Idris I and named Agadir, which meant fortress.

In the 11th century (1080), with the installation of the Almoravids, the great commander Youssef bin Tashfin moved the site of the city a little further to the West: "Tagrart" (station) becomes, after Marrakesh, the second capital of the empire that encompassed the current Morocco and part of Western Algeria. During this period, he renamed it Tilimsan. Tlemcen flourished under the rule of the Zianid dynasty which dominated trans-Saharan trade.

Toward the end of the 13th century, the Merinids of Fez waged war against the Zianids for domination of the Magreb and laid siege to Tlemcen in 1299 and started constructing the city of Mansourah outside the walls of the city. The siege lasted until 1307 when the Merinid commander was assassinated and the Merinids withdrew from Mansourah.

The struggle between the Zianids and Merinids continued for decades and Tlemcen was besieged again between 1337 and 1359 until finally it fell and the Merinids returned to rule from Mansourah. The Zianid dynasty steadily declined during the 15th century, falling under Spanish influence and finally succumbed to the Ottoman rule. Throughout this period Tlemcen was dominated alternately by the Merinids of Fez and Hafsid of Tunis.

In 1555 Tlemcen was taken over by the Ottomans and suffered a period of neglect. The French invasion of Tlemcen in 1830 divided the city into two camps, the pro-French Kouloughlis, the mixed-race descendants of Turkish-Arab intermarriages, and the Berber and Arab partisans of Emir Abdel Kadir.

The Tlemcenis managed to fend off French occupation for over a decade until the city fell in 1842; but by then Tlemcen had been infused with the spirit of Algerian nationalism.

One of the city's sons, Ahmad Messali Hadj, founded Algeria's first independence movement in 1924 and became the leader of the MTLD (Mouvement pour le Triomphe des Libertés Démocratiques) which produced many Algerian revolutionary leaders.

Tlemcen is dotted with its magnificent monuments which gives it an authentic charm. Beautiful mosques dating from medieval times are among the finest and oldest in the Maghreb.

More or less 45 natural and historical sites in the region of Tlemcen are classified, we cite: The Great Mosque of Tlemcen, Sidi Boumedienne, the Medrassa or the Franco-Muslim high school, the tomb of the princess, Sidi Bel

Hassan, the Mechouar, El-Mansourah, the Great Basin, Bab Qarmadine, El-Kissariya, the old city of Agadir, Sidi Snoussi Mosque, Vestige of the palace Dar es Soltan, The Medina (city) of Tlemcen, Castle (near the hospital), The remains of Hassan Boukli, Sidi El Halloui, Sidi Bou Ishag Etayar, Bab El Khamis, the islamic Library.

A small presentation of the most important is given in the next sub-section. More detailed discussion is dedicated for El-Ourit Bridge, that is, for it the structural point of view an important cultural heritage structure where civil engineer can do lot. This structure was a subject to a recent article by the author [Boumechra and Hamdaoui, 2008].

2.3.2.1 The Great Mosque of Tlemcen

The Great Mosque of Tlemcen is the most interesting of mosques dating of medieval times in the city. This mosque has a remarkable architecture and is located downtown. It was built in the 12th century by Ben Ali Yusuf, a prince Almoravid, but Yaghmoracen, the founder of the dynasty Zianides, gave its final dimensions, adding the minaret and the Central Dome. Annexed to this mosque, a court is found in addition to a great Islamic university that was considered as one of the largest in the Maghreb. Many renowned savants have taught and inhabited. Today, these annexes no longer exist. The “mihrab”, richly worked, is of a wonderful architecture, its ornament is similar to the one of the Mosque of Cordoba.



Figure 2.15: The great mosque of Tlemcen.

2.3.2.2 Sidi Boumedienne

The area of El-Eubad that overlooks the city of Tlemcen, includes important monuments: the “kouba” (dome) Sidi Boumedienne, its mosque, its medrassa (school) and its “medina” (city).

The “kouba” Sidi Boumedienne shelter the patron saint of Tlemcen, who was a great savant in the 12th century. Its mausoleum still remains the most visited of Tlemcen’s monuments. The mosque of Sidi Boumedienne and its “medrasa” have been built in the 14th century by a sultan of Fez, the “black sultan”, at the second invasion Merinid (which lasted 7 years). In the Andalusian style of Granada, the minaret is decorated with bricks and polychrome ceramics.



Figure 2.16: The mosque of “Sidi Boumedienne”.

2.3.2.3 Machouar

Another major attraction is the Mechouar which literally means “advisory councils”. The citadel was built by Abd El Moumen. During the reign of Zianides, it became one of the main seats of the Kings of Tlemcen, meetings of state at the Mechouar . Yaghmorassan undertook major restoration work and beautification when he built his palace and its annexes. The Mechouar has a unique structure, its eastern side rests on a hill, and on the other part, the citadel rests on a layer of water. The main entrance door was probably a bridge called

Bab El Bounoude. During the long reign Ziyanide, this monument has been seen a great expansion, changes and enhancements in several stapes with a variety of edifices, outbuildings, annexes and other constructions as the two Bastions of Ziyanide Style of round columns, still remaining. Despite the destruction of the great building, its palaces and all the Eastern walls during the French colonization, its space remains fascinating and especially mysterious. Undoubtedly, great archaeological research should be undertaken in the coming years in order to penetrate the many mysteries surrounding the Mechouar, such as its underground channels, its exceptionally thick walls ...



Figure 2.17: El-Machouar citadel.

2.3.2.4 Mansourah

Another remarkable monument of this city is none other than Mansourah, that was a city built right next to Tlemcen. The Mansourah means “the victorious”. The only remains now are the minaret of the mosque with its framing in ruins. It was constructed to compete the commercial pole of Tlemcen. This city was founded by Sultan Mérinide Abu Yacoub in 1299 during the first Merinid siege. It should be noted that the life of the city of Mansourah was extremely brief. It extended over an area of 101 hectares with a wall all around (there are still a few remnants today). A trapezoid of 4000 meters of perimeter, supplemented by 80 tours and 4 opened doors. There were, in this city, sumptuous palaces, shops, baths and beautiful gardens with the great mosque where only its façade

remains today. The walls of this minaret that are 40m high are a prestigious sculpture.



Figure 2.18: Ruins of El-Mansourah.

2.3.2.5 El-Ourit Bridge

The bridge usually known as “El-Ourit bridge” and built in 1889 by the well known Engineer “Gustave Eiffel” (Figure 2.19), is a major component of the Tlemcen - Sidi Bel Abes railway line, 5 km from the entrance to the city of Tlemcen. The steel bridge is of great interest for its conception, its age and its position for the rail network. It permits to access the city of Tlemcen by crossing a very rugged region, the one of Oued Mefrouche.

Historical survey

The construction of this bridge has gone through the following steps:

1. The railway segment Tabia to Tlemcen (64 km), was authorized by a law of July 16, 1885. It was carried out by the “Compagnie des Chemins de fer de l’Ouest Algérien” (West Algerian Railroads Company) and finished in 1889 [Antoine, 1913], [Morton, 2003].

2. The projects of the masonry and the steel part of the structure were presented by the engineer of the “Compagnie des Chemins de Fer de l'Ouest Algerian”, for approval of the Ministry of Public Works, in Paris, on June 28 and August 31, 1888 respectively.
3. December 14, 1888, a decision of the General Governor of Algiers giving the green light to the proposed implementation of steel bridge and of the two masonry abutments. The aesthetics of masonry and its harmony with the surrounding site were considered and encouraged by the General Council of Bridges and Roads.
4. Realisation of the structure from 1888 to 1889. Louis Abadie described the bridge in the book “Tlemcen, au passé retrouvé” [Abadie, 1994]: The bridge, located between five tunnels had been built in a way to avoid the digging of cliff. It was sixty-eight metres and was tested in 1889 by installing a train of 250 tons. In that day, many Tlemceniens came, curious to attend the demonstration which turned out to be positive.
5. The amount of the project was estimated to 278.000,00 old French Francs, where 152.000,00 Francs for the steel part, say 55%.
6. The railway line started its service in 1890.
7. The structure was defined following the nomenclature PK 133 + 253 established by the department of railways.

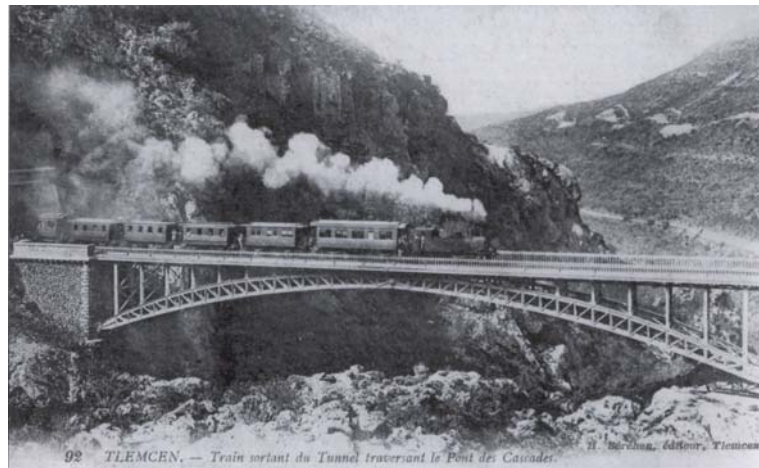


Figure 2.19: El-Ourit arched steel bridge (beginning of 19th century).

Location

The El-Ourit steel bridge is located on the east side of the city of Tlemcen, 7 km on the railway line Tlemcen - Sidi Belabes. It allows the passage of a very rugged mountain pass.

The neck, with total depth of 510m and a width of 2km, consists of Ech-Chouka mountain in the Northern side, Beniane and Tichtiouine mountains at the eastern side and Jebel Hanif in the Southern side, that culminates at 1279m of height. At the bottom downstream of this attitude is Djorf El Diab at 639m above sea level. From Tel-Terni upstream waters of the Oued Mefrouche is throwing in the neck in the form of majestic waterfalls (Figure 2.20). Since the great dryness of 80, these waterfalls are dry.

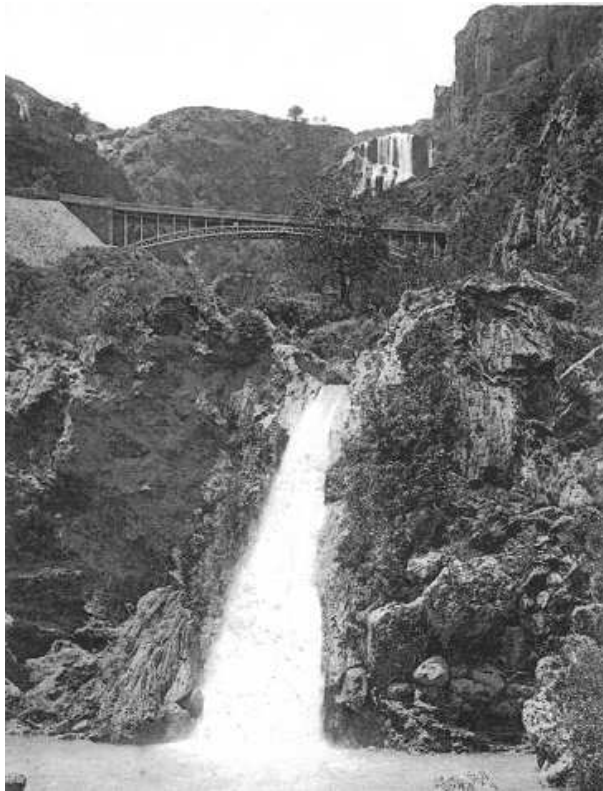


Figure 2.20: An old photo of the bridge with waterfalls.

The railway line bypasses to a downward altitude ranging from 847m to 810m (direction from Sidi Bel-Abbès to Tlemcen). On this circumvention, two tunnels were built: one in the east, of length 700m and the other to the west of length 80m. They were constructed in 1889-1890.

The mountains are of limestone formation, of lower Jurassic.

Formerly, this region was heavily wooded, especially in Aleppo. Over the last decade, several fires have decimated it.

Although the famous waterfalls of El-Ourit have disappeared, the region remains a tourist attraction by the natural and geological beauty it contains.

Description of the structure

The bridge is of 68m length and 8m height. It is composed of two beams, stiffened between them by the higher apron in addition to the horizontal and vertical diagonal wind-bracings. At mid-span, it presents a joint and an articulation connecting the two half spans. In addition to the articulation, the two parts of the bridge are connected by rods of pre-stressed ties placed in diagonals. This system was conceived to partially relieve the structure, therefore to increase its flexibility, considering the supports that are fixed on the abutments.

This choice was made to limit the problems of temperature variation and any possible geological movement.

The principal carrying element is the arched girder with lattice made up of two soles of variable thickness. This frame is simply supported on the abutments. The structure consists of steel elements riveted out of wrought iron. The principal carrying element is the bottom arc beam of a curvature radius of 300 m. This arc supports the apron via amounts and strengthened by horizontal and vertical wind-bracings. The transverse distance between the two arched girders is of 4.50 m. The physical and mechanical tests on metallic samples taken from steel elements of the same age of the bridge were made and gave the following results: density = 7.30 kN/m^3 , Young Modulus $E = 1,785.108 \text{ kN/m}^2$, Poisson ratio $\nu = 0.30$ and Yield stress $f_y = 245 \text{ N/mm}^2$.

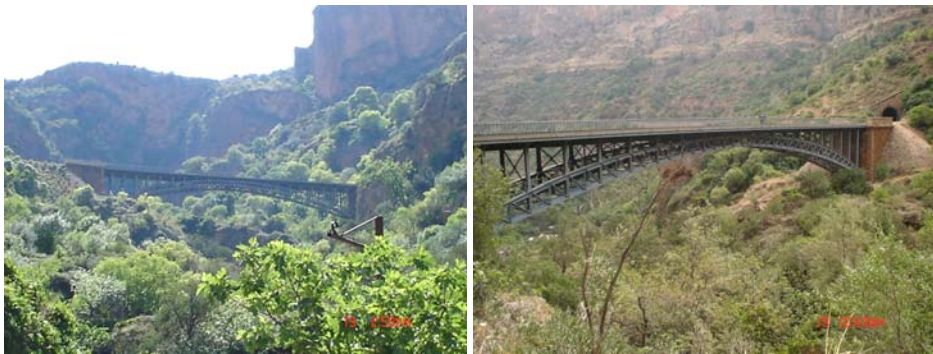
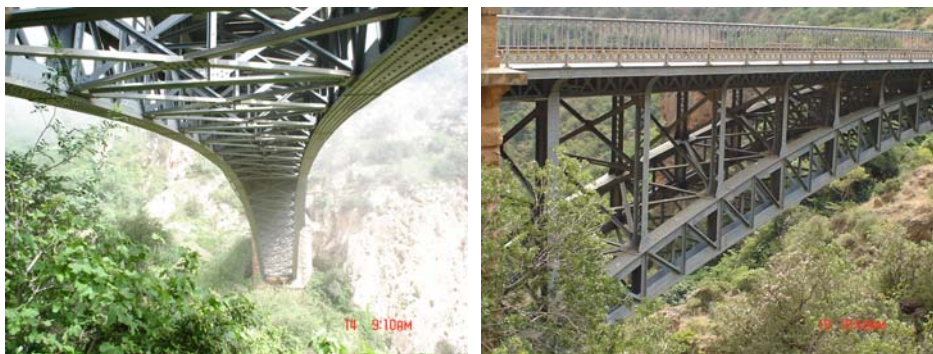


Figure 2.21: El-Ourit bridge, recent photos.



(a)

(b)



(c)

(d)

Figure 2.22: Different views of the bridge's structure: (a) Underside of the bridge, (b) The steel structure, (c) Support system, (d) Medium articulation.

References

1. Abadie L. (1994). *Tlemcen au Passé Retrouvé*, Editions Jacques Gandini. (In French).
2. Abdessemed-Foufa A. and Benouar D. (2005). "Atlas of Earthquake-Resistant Traditional Techniques in Algeria: The Case of the Casbah of Algiers", *European Earthquake Engineering journal*, EEE 2, 05, 2-29.
3. Aoudia A. and Meghraoui M. (1995). "Seismotectonics in the Tell Atlas of Algeria: the Cavaignac (Abou El Hassan) earthquake of 25.08.1922." *Tectonophysics*, 248, 263-276.
4. Aoudia A., Vaccari F., Suhadolc P. and Meghraoui M. (2000). "Seismogenic potential and earthquake hazard assessment in the Tell Atlas of Algeria", *J. Seismol.* vol. 4, 79-98.
5. Bendimerad F. (2004). "The 21 May 2003 Boumerdes Earthquake Lessons Learned And Recommendations", *13th World Conference on Earthquake Engineering*, Vancouver, B.C., Canada August 1-6.
6. Benouar D. and Laradi N. (1996). "A Reappraisal of the Seismicity of the Maghreb Countries – Algeria, Morocco, and Tunisia", *Natural Hazards*, vol. 13, no. 3, 275-296.
7. Benouar D. (1994). "Materials for the investigation of the seismicity of Algeria and adjacent regions during the twentieth century", *Special Issue of the Annali Di Geofisica* (Istituto Nazionale di Geofisica, Italy), vol. XXXVII, No. 4.
8. Bernard M.A. (1913). *Les chemins de fer algériens*, éditions A. Jourdan. (In French).
9. Bezzeghoud M. and Buforn E. (1999). "Source parameters of 1992 Melilla (Spain, MW= 4.8), 1994 Alhoceima (Morocco, MW= 5.8), and 1994 Mascara (Algeria, MW= 5.7) earthquakes and seismotectonic implications", *Bull. Seismol. Soc. Am.*, vol. 89, 359-372.
10. Boumechra N. and Hamdaoui K. (2008). "Dynamic and Fatigue Analyses of an 18th Century Steel Arch Bridge", *Proceedings of the 2008 Seismic Engineering International Conference "MERCEA'08"*, Reggio Calabria, Italy.

11. CGS- Centre de Genie Paraseismic, www.cgs-dz.org.
12. Chesneau M. (1892). "Notes sur les tremblements de terre en Algérie", *Annales des mines*, neuvième série, TI, Ed Dunod, Paris, France. (In French).
13. Comelin P. (1720). "Voyages pour la rédemption des captifs aux royaumes d'Alger et de Tunis", *Printed by J.Ritchie, Edinburgh*, vol. I, 277, 14-16. (In French)
14. CRAAG- Centre de Recherche en Astronomie, Astrophysique et de Géophysique. (1994). "Les séismes en Algérie de 1365 à 1992". *CRAAG Report*, Algiers, Algeria. (In French)
15. CTC. "Le Risque Sismique en Algérie". *Centre National de Recherche Appliquée en Genie Parasismique (CTC)*, Algiers, Algeria. (In French).
16. Delphin G. (1922). "Histoire des Pachas d'Alger de 1515 à 1745, Extrait d'une chronique indigène", *Extrait du Journal Asiatique (Avril-Juin 1922 et Janvier-Mars 1925)*, Paris, Imprimerie Nationale, 216-218. (In French).
17. EERI. (2003). "The Boumerdes, Algeria, Earthquake May 21, 2003", *An EERI Learning from Earthquakes Reconnaissance Report*, Earthquake Engineering Research Institute, Oakland, California.
18. Frizon de Lamotte D., Saint Bezar B., Bracenc R. and Mercier E. (2000). "The two main steps of the Atlas building and geodynamics of the Western Mediterranean", *Tectonics*, vol. 19, 740-761.
19. Grammont H. (1887). *Histoire d'Alger sous la domination turque 1515 - 1830*, Ed Levoux, Paris, France. (In French).
20. Harbi A. (2005). "Evaluation de l'aléa sismique en Algérie du Nord par la modélisation de l'input sismique dans les zones urbaines et l'établissement d'un catalogue", *Ph.D Thesis*. University of Algiers, Algeria. (In French).
21. Horne A. (2006). *A Savage War of Peace: Algeria 1954-1962* (New York Review Books Classics). 1755 Broadway, New York, NY 10019: NYRB Classics, 29-30.
22. La démographie figurée de l'Algérie, available on line: <http://gallica.bnf.fr/ark:/12148/bpt6k103772b>. (In French).

23. McKenzie D. (1972). "Active tectonics of the Mediterranean region", *Geophys. J. R. Astron. Soc.*, vol. 30, 109-185.
24. Meghraoui M. (1988). "Géologie des zones sismiques du nord de l'Algérie, tectonique active, paléo-sismologie et synthèse sismotectonique", *PhD dissertation*, University of Paris-Sud, France. (In French).
25. Mickus K. and Jallouli C. (1999). "Crustal structure beneath the Tell and Atlas Mountains (Algeria and Tunisia) through the analysis of gravity data", *Tectonophysics*, vol. 314, 373-385.
26. Morton P. (2003). "Le développement des chemins de fer en Algérie", *Extrait de la revue du Gamt*, no. 71/2003/3 and 72. (In French).
27. Press. (1716). *Gazette de France*, no. 8 of 10th and 20th, March.
28. Saidouni N. (1985). "El ahwâl ech-chakhsiâ wa al-wadh ed-dimoghrâfi fi al-djazâ'ir athnâa al-aahd al-othmâni". In *Revue d'Histoire du Maghreb*, no. 39-40, 431-445. (In Arabic)
29. Tapponier P. (1977). "Evolution tectonique du système Alpin en Méditerranée poinçonnement et écrasement rigide plastique", *Bull. Soc. Geol. Fr.*, vol. 19, 437-460. (In French).
30. Tassy L. (1830). *Histoire d'Alger et du bombardement de cette ville en 1816*, Librairie Piltan, Paris, France. (In French).
31. Wikipedia encyclopaedia, www.wikipedia.org.

Chapter 3

Pre-stressed SMA Wires for Structural Retrofitting: the Masonry Wall Model

3.1. Introduction

Ancient, or historical, buildings often present themselves as an assemblage of compact and un-reinforced stone elements. They are either simply held together by the gravity load effect or, in the best case, linked by means of old and/or weak mortar layer. Such structures are especially sensitive to vibrations induced by the surrounding environment, as well as to natural hazards: retrofitting is a must in view of preserving them to future generations.

Two main challenges are usually encountered when dealing with structures of this type: (i) the material properties are not directly estimable and the constitutive law shows a nonlinear behaviour under the existing stress-state; (ii) the damage and construction history spans centuries, thus making the current structural assessment quite difficult. Furthermore, standard restoration techniques often result inadequate and fail to meet the non-invasive requirement.

An innovative solution suggests of exploiting the special features of the SMA super-elastic behaviour under dynamic excitation. Pre-stressed SMA wires or trusses can be installed between the brick components, with the effects of limiting the vibration-induced relative displacements and, at the same time, allowing for energy dissipation [Casciati and Faravelli, 2004]. The ties are pre-

tensioned up to the stress level which characterizes the “plateau” of the alloy constitutive law, so that the value of the linking pre-stressing force is preserved at an increased strain level.

A specific Copper-based alloy was identified as particularly suitable for the envisioned application, due to its low cost and its wide temperature range. The author, as a member of the WIND-CHIME team active in Pavia, Italy, benefited of years of experimental tests that have provided a deep understanding of its mechanical behaviour [Casciati and Faravelli, 2003], [Casciati and Faravelli, 2004], [Casciati and Faravelli 2007], including the response to fatigue cycles [Casciati et al., 2007], [Casciati, 2007].

The potential offered by this innovative retrofitting technique was the topic of several research studies performed within some projects funded by the European Union: ISTECH, MANSIDE, CHIME, and WIND-CHIME. Broad spectrum reports of the achieved results can be found in [Auricchio et al., 2001], [Cardone et al., 1998], [Casciati and Osman, 2004] and [Casciati, 2006].

The need to preliminarily model, plan, and optimize a retrofit operation via SMA devices led the author to design and implement a step by step process, to be applied during the design phase of the retrofit. In this chapter, in order to investigate the effect of installing SMA pre-stressed device as retrofitting solution for historical buildings, a prototype built by superposed bricks -to reproduce the properties of a monumental structure- was empirically evaluated, without a thorough attempt to investigate the mechanical principles that underlie the collected data. At the top of the wall laboratory model, see Figure 3.1, a superimposed rigid steel plate was placed to simulate the weight of the upper wall portion. Shaking table tests were conducted, first, on the built model in its unprotected virgin state (without insertion of any pre-stressed SMA wires). Then the wall is tied by the pre-stressed wires to evaluate the improvement in term of seismic response. The advantages of deploying the proposed pre-stressed SMA wires in the restoration of historical monuments are, finally, illustrated with reference to the standard technique of using steel bars.

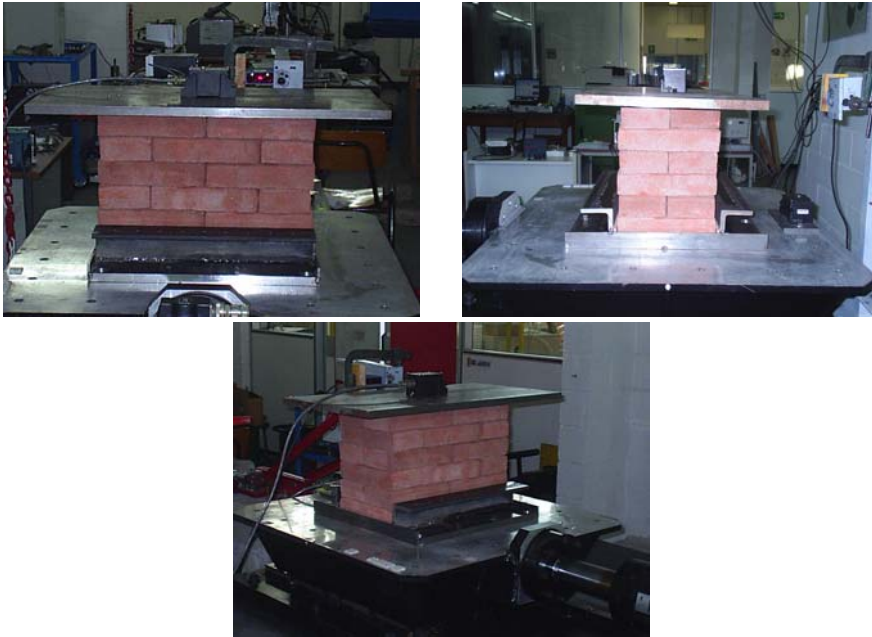


Figure 3.1: The proposed wall model placed on the shaking table.

3.2. Characterization of proposed masonry wall

3.2.1 Single brick characterization

The experimental tests carried out within the research activity reported in this chapter required the preliminary acquisition of a stock of bricks from the market. The geometry of a single brick is simply 25×12.5×5.5 cm (slightly bigger than the nominal dimensions), and its mass density is $\rho=1750 \text{ kg/m}^3$. A Poisson ratio of 0.15 is assumed. A material specimen of sizes 2.5×2.4×2.5 cm was cut from one of the bricks, in order to undergo a mono-axial compression test using the available universal testing machine. The sensor readings in Figure 3.2 suggest an average value of the Young modulus equal to 916 MPa, with a peak value of 935 MPa. However, the test results are affected by the specimen reduced dimensions (scale effect), the brick porosity, and the testing conditions.

To improve the Young modulus estimate, a further test is performed on a sample brick. The brick is vertically mounted on a steel base, and supports a steel plate with a mass on the top. The resulting system is a single degree-of-freedom oscillator which is placed on a shaking table. Its resonant frequency is estimated for different mass values. A synthesis of the result is given in Table 3.1.

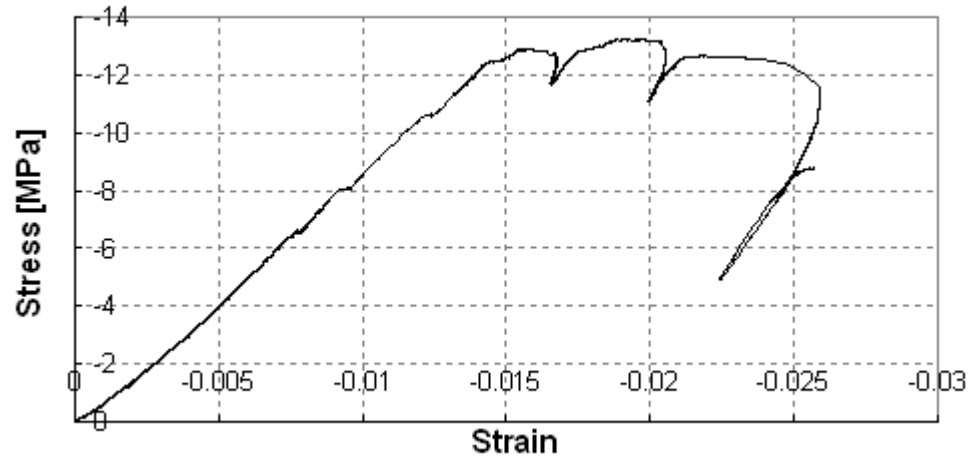


Figure 3.2: Stress-strain diagram from the compression test (i.e., negative stress values) on the material specimen obtained from a single brick.

Table 3.1: Estimates of the system natural frequency resulting from several shaking table tests on a single brick.

Case #	Mass [kg]	Peak bottom acceleration [m/s ²]	Frequency [Hz]	Young modulusEstimate [kPa]
1	31	0.4770	16.02	1078469.24
2	70	0.0703	10.03	1020597.74

3.2.2 The masonry specimen

The tested structure is a set of bricks assembled to form a typical masonry specimen (Figure 3.1 and 3.3), reproducing the design and the mechanical properties of a portion of monument as the ones met in historical cities. The specimen has the depth of two bricks ($b=25$ cm), two bricks length ($L=50$ cm), and the height of six layers of bricks (33 cm). Its weight, P , is 0.6 kN. A rigid steel plate of mass 50 kg and thickness 2 cm is mounted on its top, in order to ideally simulate the weight of an upper wall portion. As a secondary effect, the rigid plate avoids the out-of-plane collapse of the system during the vibrations of low intensity. In the following calculations, a height, h , of 34 cm (including half of the steel plate) is considered.

The model is tested using the uni-axial shaking table available at the Vibration Laboratory of the Structural Mechanics Department, University of Pavia [Casciati and Hamdaoui, 2008]. Two accelerometers are mounted: one on the shaking table and the other on the top of the wall. A no-contact, laser optic sensor is also deployed to measure the displacements: its readings are reliable only for large excitation intensities. Each single brick forming the masonry wall is of the same kind investigated in the previous section.

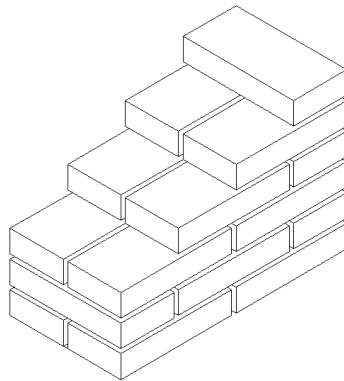


Figure 3.3: Details of the tested wall.

3.3. Methodology and testing procedure

The structural behaviour of the proposed masonry wall will be investigated for different number and position of the pre-stressed SMA wires. After the construction of the wall and the treatment of the SMA wires (thermally and mechanically), shaking table tests by assigning the displacement time history obtained from a realization of a filtered white noise acceleration were conducted with considering the following spans: 6 mm, 30 mm, 60 mm, 75 mm, 112.5 mm and 150 mm. The test aims to capture the accelerations at the top of the wall using very sensitive sensors. The first shaking test was conducted on the wall in its virgin state (without introducing any pre-tensioned SMA wire), then with one central wire at each site, two wires at each corner of each side and finally, with three equidistant wires at each side.

The modal frequencies and mode shapes are extracted by applying output-only modal identification techniques that are available in MATLAB [MATLAB, 2004] (SI using N4Sid algorithm (the unweighted principal component algorithm), Frequency Domain Decomposition and, Fourier Fast Transform). A three-dimensional finite element model of the structure, using the software package SAP 2000 [SAP, 2003], was developed and calibrated according to the modal parameters of each experimental test (without and with different number and position of wires). The calibration process will be conducted by enhancing the masonry mechanical characteristics to achieve a relation between the improvement due to the use of pre-stressing force from SMA wires and its effect on the masonry equivalent modulus of elasticity. The percentage of improvement in the mechanical properties is estimated.

Finally, the same tests were numerically simulated introducing steel bars instead of the SMA wires.

3.4. The wall in its virgin state

3.4.1 Laboratory tests

This first series of tests aim to identify the wall original behaviour. Table 3.2 reports the corresponding peak values of the recorded accelerations and the estimated parameters. The results in terms of resonant frequencies are estimated by using the Matlab “N4Sid” State space algorithm [Matlab, 2004].

Table 3.2: Experimental frequencies detected by using the “N4Sid” state space algorithm. The equivalent Young modulus is then estimated from the homogeneous material numerical model (FEM).

Case	Span [mm]	Shaking table peak acceleration [m/s ²]	<i>Estimated parameters</i>		
			Experimental Frequency [Hz]	FEM Equivalent Young Modulus [Mpa]	FEM Lumped Mass [kg]
1	6	0.04	11.10	9.480	96.95
2	30	1.44	8.74	5.875	96.91
3	60	4.79	8.73	5.865	96.96
4	75	7.13	6.45	3.200	96.92
5	112.5	10.17	4.78	1.758	96.95
6	150	12.35	4.60	1.628	96.94

The lack of linearity in their relation (very low peak accelerations are achieved when the intensity factor is either 0.1 or 0.5) depends on the response spectrum features of the available shaking table.

In terms of graph, Figure 3.4 shows a singular peak value in correspondence of the detected frequency. It is worth noticing that the second “hill” at 20 Hz is due to the resonance of the testing machine, and not to the tested specimen. The test

with the excitation signal of highest intensity (span 150 mm) had to be interrupted before its scheduled duration, due to the excessive brick openings.

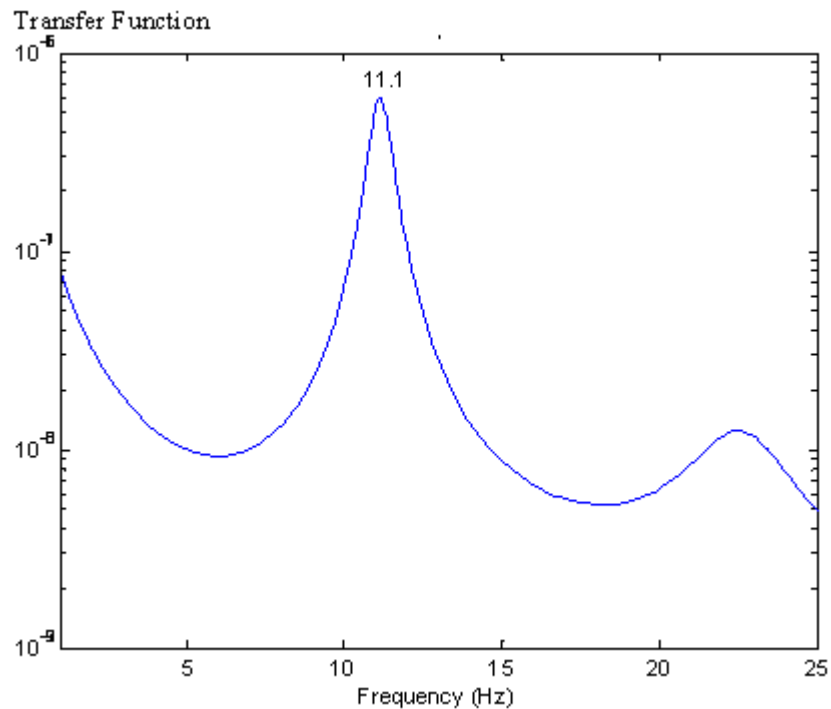


Figure 3.4: Natural frequency of the un-reinforced masonry wall, as detected with the transfer function estimated by excitation signal of the lowest intensity.

3.4.2 Finite element model and equivalent homogeneous material

In the standard finite element idealizations of masonry structures, a homogeneous and isotropic material model is adopted, with both compressive and tensile strengths different from zero. The elastic modulus of the so called “equivalent” material is fixed in such a way that the system under investigation

behaves consistently with the actual experimental response, as suggested in [El Borgi et al., 2005].

Within the SAP 2000 software (version 9), three-dimensional, eight-node, solid elements are selected to create a finite element model (FEM) of the wall specimen, as shown in Figure 3.5.

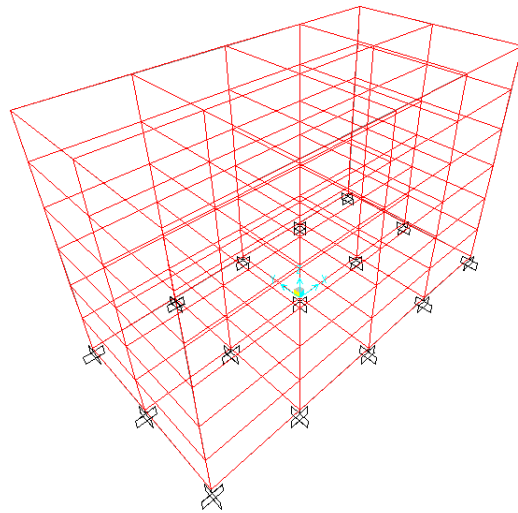


Figure 3.5: 3D, 8-noded, finite elements model of the masonry wall.

The rigid plate mass is schematized by assigning lump masses to the nodes at the top of the mesh. As mentioned above, the material is assumed to be homogeneous and the modulus of normal elasticity is set equal to an “equivalent” value, E_{eq} , which is selected so that the analyses lead to detect the same natural frequencies obtained from the experimental tests. In Table 3.2, a different value of E_{eq} is found for each considered experimental test. The simple cantilever scheme in Figure 3.5 has the stiffness properties governed by the following relation

$$k = \frac{3E_{eq}J}{h^3} \quad (3.1)$$

being J the weak moment of inertia of the wall constant cross-section. By recalculating the lumped mass of the top nodes as

$$m_L = \frac{(2\pi f)^2}{k} \quad (3.2)$$

Approximately, the same value is obtained for all the analyzed cases, as indicated in the Table 3.2.

3.4.3. Accounting for a reduced effective cross-section

In the previous section, different values of the masonry equivalent Young modulus, E_{eq} , were estimated from excitation signals of increasing intensities (Table 3.2). The present section is dedicated to show that the dependence of E_{eq} on the excitation amplitude is only fictitious, being the differences in the experimental frequencies related to the geometrical changes of the masonry cross-section under the excitations of highest intensities.

In the absence of mortar, indeed, each brick can rotate around the three spatial axes, giving rise to openings as the ones in Figure 3.6. This behaviour is unrespectful of the continuity assumption on which the beam theory relies. Thence, Eq. (3.1) is just an approximation.

The openings between two bricks, one over-standing the other, prevent to transmit the tensile stresses between them to the adjacent bricks, thus implying the inability of the cross-section to react under traction. As a consequence, the specimen effective cross-section is reduced to the compressed zones, whose width b_c is computed as follows.

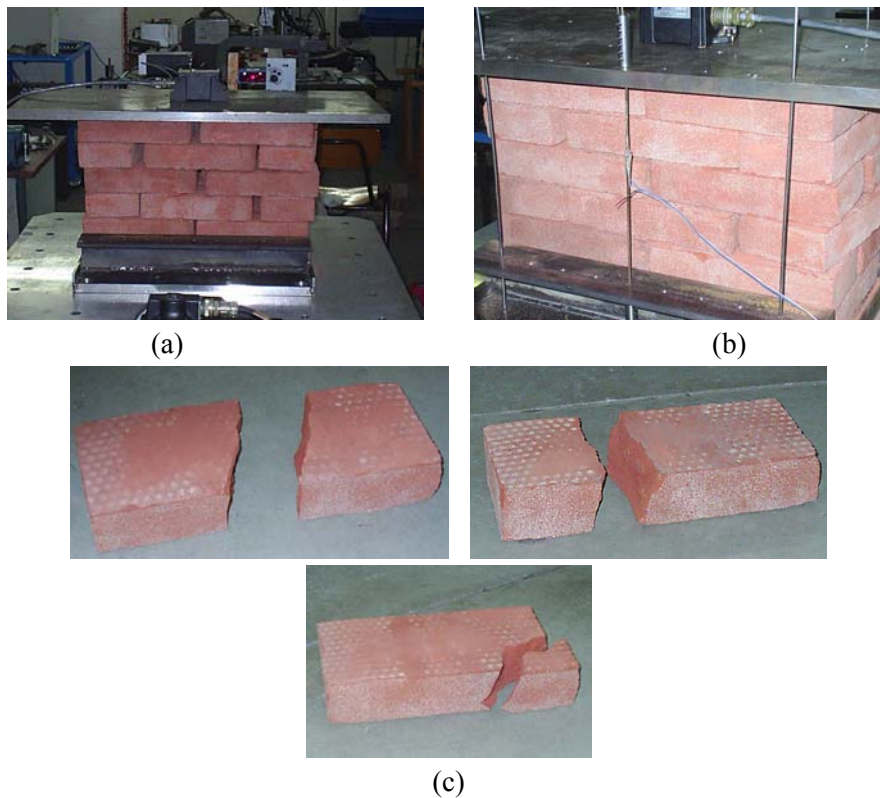


Figure 3.6: Examples of the brick openings at the end of the tests with the shaking table: (a) lateral displacements; (b) twisting around the vertical axis; (c) cracked bricks.

The goal is to build the structural scheme of a cantilever beam with variable cross-section (Figure 3.7). Under dynamic excitation, the effect of the rigid plate mass lumped at the top, together with the wall mass, is represented by an inertial force, $F = m_L a$, with a the horizontal acceleration at the top of the wall. The weight of the rigid plate also results in a centred axial load, N_{top} , acting on the free edge of the wall. The resultant of F and N_{top} is aligned with

the mid-point of the cross-section width, b . Thus, at the free edge, the cross-section is fully compressed.

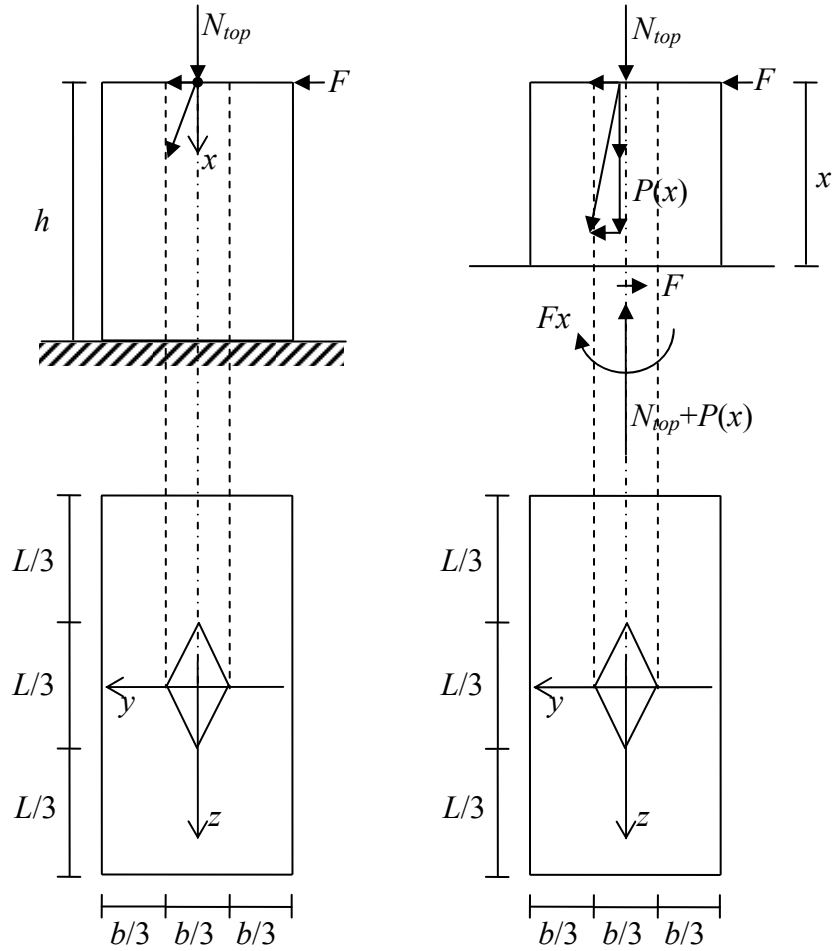


Figure 3.7: The cantilever beam model and the inertial properties of its cross-section: (a) fully resistant section at top; (b) free body diagram of the wall upper portion.

Let x denote the spatial coordinate that follows the beam axis from the free edge to the bottom. Along x , the axial load gradually increases due to the self-weight

of the increasing wall portion, $P(x) = \rho g A x$, where $g = 9.81 \text{ m/s}^2$ is the gravity acceleration and $A = bh$. From the free-body diagram of Figure 3.7, the moment balance around the free edge requires that, at level x , the eccentricity $e(x)$ of the total axial force is given by

$$e(x) = \frac{Fx}{N_{top} + P(x)} \quad (3.3)$$

For $e(x) \leq b/6$, the wall cross-section is fully reacting, being it subjected to only compressive stresses.

If h_c is the height at which the eccentricity $e(x)$ reaches the value of $b/6$, for $x > h_c$ the effective cross-section starts reducing due to the rising of tensile stresses. Within the range $b/6 < e(x) < b/2$, the depth, $b_c(x)$, of the compressed zone is given by

$$b_c(x) = 3 \left(\frac{b}{2} - e(x) \right) \quad (3.4)$$

and it results from assuming a triangular re-distribution of stresses, whose resultant is aligned with the pressure point.

If x becomes greater than the level h_c^* at which $e(x) = b/2$, the wall cross-section is fully non reactive. The survival of the system is due to the dynamic nature of the excitation, while a static force would have caused the overturning of the wall.

The resulting moment of inertia, $J(x)$, of the effective cross-section has the following distribution along the beam axis

$$J(x) = \begin{cases} \frac{1}{12} Lb^3 & \text{for } 0 < x < h_c \quad (0 \leq e(x) \leq b/6) \\ \frac{1}{12} L[b_c(x)]^3 & \text{for } h_c < x < h_c^* \quad (b/6 < e(x) \leq b/2) \\ 0 & \text{for } h_c^* < x < h \quad (b/2 < e(x)) \end{cases} \quad (3.5)$$

In a static context, the stiffness k_F , against the horizontal force at the top, F , can be estimated assuming an elastic behaviour for such a variable cross-section cantilever. Indeed, its inverse, $1/k_F$, representing the flexibility associated with the given value of the force F , is computed as the displacement of the free edge under an unitary force, $F = 1$. For the numerical calculations, when $x > h_c^*$, a constant value slightly greater than zero is assigned to $J(x)$. The Young value modulus also needs to be a priori known. In the following, one assumes that it is equal to the value of the equivalent Young modulus, E_{eq} , estimated from the test with the excitation of low intensity. The lower values estimated from the other tests can be considered just as the result of an artifice to account for the actual inertial moment reductions, when they are not explicitly included in the analyses.

When the excitation of low intensity is considered, the masonry cross-section is fully reactive along the entire height of the structure, and the stiffness k is given by Eq. (3.1), since no openings are forming. The flexibility is constant and equal to $1/k$.

In the intermediate cases, where the maximum eccentricity is kept within the range $b/6 < e(x) < b/2$, $J(x)$ is also a function of time, and the actual behaviour of the wall consists of alternating fully reactive states with the formation of openings, and viceversa. The nonlinear behaviour causes the tangent flexibility to vary from $1/k$ to $1/k_F$, with F the current level of the

force. Reference can be made to Figure 3.8, which plots the flexibility as a function of the top force F . For a given force \bar{F} , the area under the graph within $0 \leq F \leq \bar{F}$ is the static displacement under the force \bar{F} . The wall secant stiffness, k_{sec} , associated with this maximum value of the force is the ratio between the force and the area.

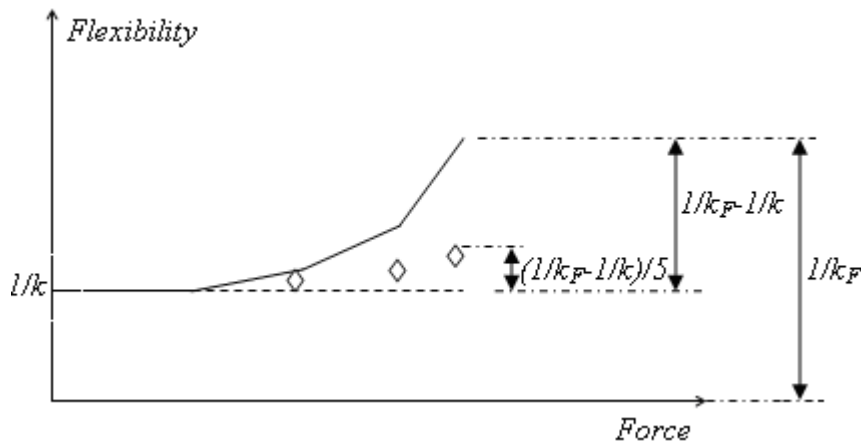


Figure 3.8: Flexibility versus force.

The test on the shaking table is of a dynamic nature, but the spectral analysis performs a sort of linearization by identifying a sort of equivalent secant stiffness k_c , as different from the secant stiffness k_{sec} associated with the maximum value of the force. Therefore, the identified stiffness k_c will assume an intermediate value between the static secant stiffness, k_{sec} , and the one computed by Eq. (3.1) for a fully reacting cross-section. Once k_c is determined, the system frequency can be re-calculated by the equivalent of Eq. (3.2).

Empirically, one finds a good agreement with the experimental frequencies of Table 3.2 by estimating k_c from the flexibility curve of Figure 3.8, after reducing its ordinates by a factor of 1/5 in the range of F exceeding the linear

field. This observation holds for excitation intensities that cause a maximum eccentricity within the range $b/6 < e(x) < b/2$. From the test results, within this range, the value of k_c does not exceed an upper bound equal to αk , with k given by Eq. (3.1) and α is a coefficient lower than one, whose value depends on the height h_c of the actually reacting part of the cantilever beam.

For excitations of higher intensities, a stiffness lower bound of βk , with β also depending on h_c , is experimentally found. Therefore, a linear interpolation between αk and βk can be performed for the intermediate cases.

The results are summarized in Table 3.3, which reports, in the third row, a reduction of the fixed-edge effective cross-section that corresponds to $\alpha = 0.6$. The last row of the table refers to the excitation of highest intensity. Since the associated test was interrupted because of failure, its results cannot directly be compared with the others. However, a stiffness lower bound with $\beta = 0.15$ is identified. A linear interpolation on the base accelerations is performed for the intermediate cases.

3.5 Adding SMA ties

As proposed in section 3.3, the masonry specimen will be tested now with mounted SMA ties. For the selected alloy, and, before being used as wall's reinforcement, was thermally and mechanically treated. Additionally, experimental repeat loading-unloading tension cycles test, at ambient temperature, was driven on the same specimen to deeply know its characteristics.

Table 3.3: Justification of the detected frequencies by simple geometry modifications (the value in italic was obtained by interpolation, it is not the results of the test): $N_{top} = 0.5$ kN.

Shaking table peak acc. [m/s ²]	Top peak acc. [m/s ²]	Max. Eccentricity [m]	b_c [m]	$10^4 J_{min}$ (at bottom) [m ⁴]	h_c [m]	kc [kN/m]	Re-calculate Freq. [Hz]	Exp. Freq. [Hz]
0.039	0.1170	0.0035 < $b/6$	0.25	6.51	0.34	471.09 (Eq. 1)	11.1	11.10
<i>0.52</i>	<i>1.388</i>	0.0417 = $b/6$	0.25	6.51	0.34	471.09 (Eq. 1)	11.1	
1.44	2.846	0.085 < $b/2$	0.1193	0.71	0.1022	282.65 = $0.6 k$	8.60	8.74
4.79	4.406	> $b/2$	0	0.01	0.0590	272.25	8.43	8.73
7.13	4.289	> $b/2$	0	0.01	0.0607	180.35	6.87	6.45
10.17	5.108	> $b/2$	0	0.01	0.0495	116.47	5.52	4.78
12.35	4.757	> $b/2$	0	0.01	0.0537	70.66 = $0.15 k$	4.30	4.60

3.5.1 The Alloy's treatments

Labelled AH140 and supplied by the French company "Trefilmetaux", the 2.85 mm SMA wires utilised to sew the tested wall have the following chemical composition in weight percentage:

$$Al = 11.8\%; \quad Be = 0.5\%; \quad Cu = 87.7\%.$$

The following values were provided by the producer for the transformation temperature:

$$M^{0s} = -18^\circ C; \quad M^{0f} = -47^\circ C;$$

$$A^{0s} = -20^\circ C; \quad A^{0f} = 2^\circ C.$$

The “M” and “A” mean here the martensite and austenite temperatures respectively, where the indices “s” and “f” denote respectively “start” and “finish”.

The SMA devices are subjected first to a preliminary thermal treatment [Casciati, 2007]. They are heated in an oven at 850°C for a specific time period. In general, this period ranges between 1 and 5 minutes and depends on the specimen’s cross section. Since the nominal diameter of SMA wires used to reinforce the masonry wall is 2.85 mm, a thermal treatment of 3 minutes is imperative. For other specimen dimensions, Table 3.4 is adopted [Casciati and Faravelli, 2004]. Once this procedure is finished, the cooling is made by direct immersion in water. To complete the process, the wires are treated for 120 minutes in an oven at 100°C, and then cooled to ambient temperature (22°C).

Table 3.4: Thermal treatment.

Specimen Dimensions (mm)	Heating Time (minutes)
1	1
3	3
6	4
2 x 20	5

The mechanical treatment is resumed by subjecting the wires to a number of loading-unloading cycles up to a certain limit.

3.5.2 Loading-unloading tests

Results from repeated loading-unloading tension cycles test conducted on the 2.85mm non-treated and thermally treated SMA wire (same conditions as the wires used for the reinforcement the built wall) are presented here. The test’s speed was maintained to 0.001mm/s and the deformation was measured by an extensometer using the MTS 858 Microbionix II universal material testing machine.

3.5.2.1 Tests drawn on the non-treated SMA wires

First, a test with 26 cycles was driven in deformation control along the loading phase and in force control along the unloading one, the tested specimen was subjected to 20 cycles in the range from 0 to 1% of measured strain, followed by 3 cycles in the range from 0 to 2%, and finally, by further 3 cycles from 0 and 3% of deformation. The stress-strain plot got from this test is presented in Figure 3.9.

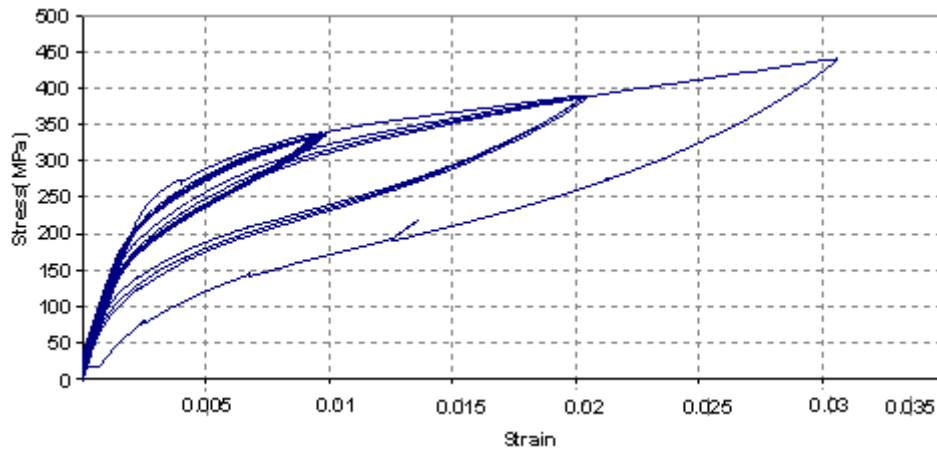


Figure 3.9: Repeated cycles test at ambient temperature: 20 cycles from 0 and 1% of strain, 3 from 0 to 2% and 3 between 0 and 3% drawn on non-treated wires. Test's speed: 0.001mm/s.

3.5.2.2 Tests drawn on the treated SMA wires

Several tests were conducted on the 2.85mm SMA wires treated in the same conditions of those used to reinforce the masonry wall. The SMA wires was subjected, in the first test, to 20 loading-unloading cycles from 0 to 1% of deformation, then, to 6 additional sequences: 3 between 0 and 2% and other 3 between 0 and 3% of strain. The plot in Figure 3.10 shows the results.

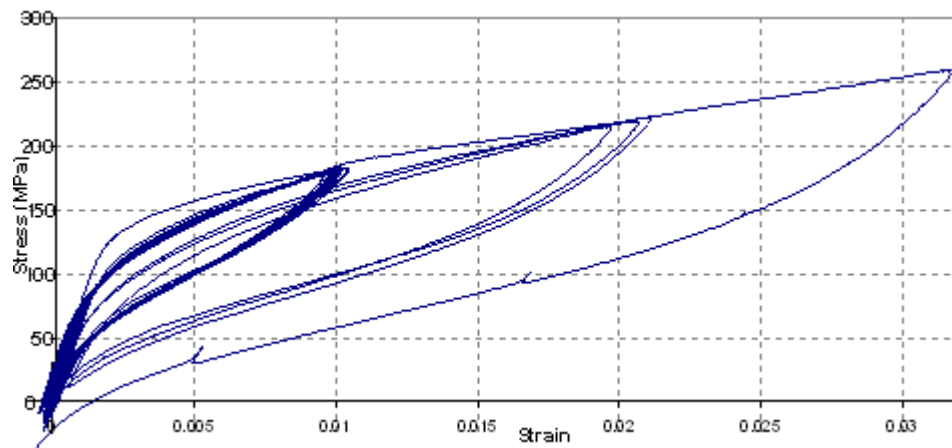


Figure 3.10: Repeated cycles test at ambient temperature: 20 cycles from 0 and 1%, 3 from 0 to 2% and 3 between 0 and 3% drawn on thermally treated SMA wires. Test's speed: 0.001mm/s.

When comparing Figure 3.10 with Figure 3.9, it is worth noting the significant reduction of the stress value at which the linear elastic branch is abandoned.

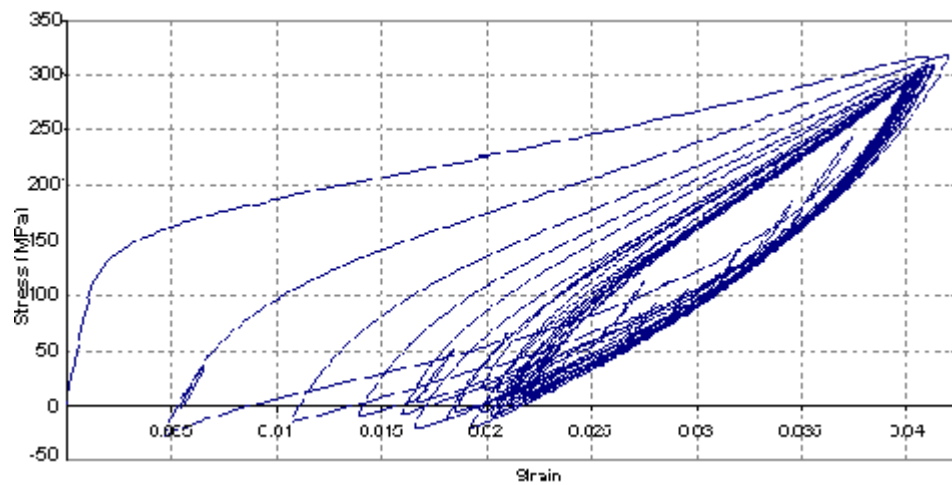


Figure 3.11: Repeated cycles test at ambient temperature: 20 cycles from 0 and 4% for a SMA thermally-treated wire specimen. Test's speed: 0.001mm/s.

In the following tests, the preliminary 20 cycles, which form the so-called training, are conducted to a higher level of deformation. Namely, in Figure 3.11, the cycles are up to 4% of strain and one note how there is martensite production which reduces the actual deformation range to a mere 2% after ten cycles.

Other two loading-unloading tension cycles tests, always at ambient temperature, were conducted. The test's speed was maintained to 0.001mm/s and the deformation was measured by the extensometer.

In the first test, a total of 30 cycles were made: 20 in the strain interval of 0 to 2% and 10 between 1 and 3% of deformation. For the second test of this couple, the first 20 loading-unloading cycles were drawn from 0 to 3% of deformation, then the addition 10 cycles between 1 and 3%.

These repeated cycles tests are summarized in terms of stress-strain curves which are plotted in Figures 3.12 and 3.13, respectively.

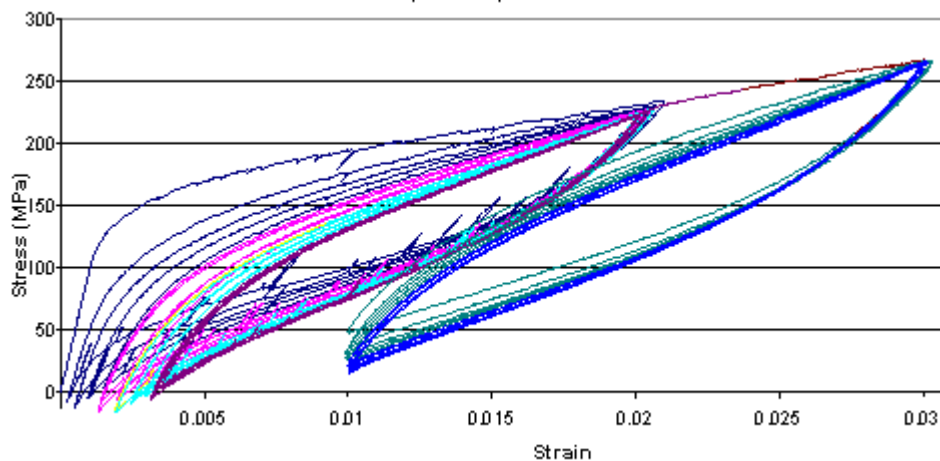


Figure 3.12: Repeated cycles test at ambient temperature: 20 cycles between 0 to 2%, plus 10 cycles between 1 and 3%. Test's speed: 0.001mm/s.

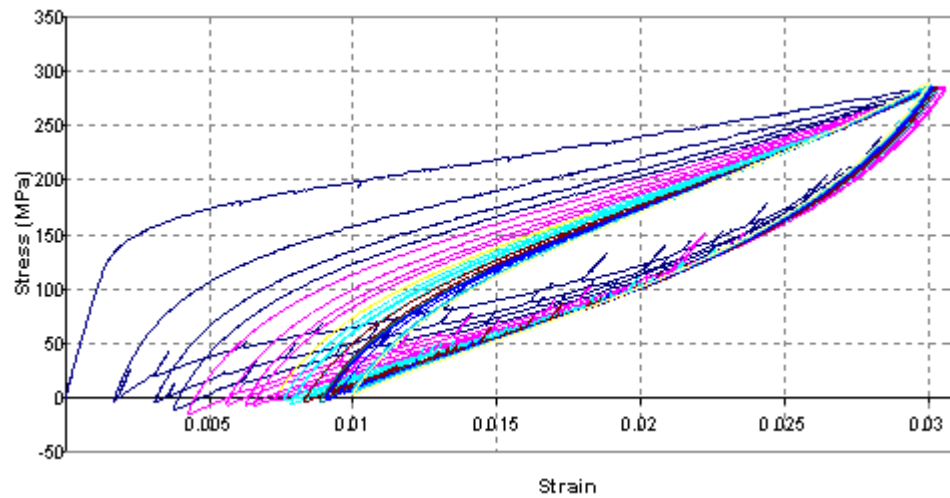


Figure 3.13: Repeated cycles test at ambient temperature: 20 cycles from 0 to 3%, plus 10 cycles between 1 and 3%. Test's speed: 0.001mm/s.

The training pursued at 3% of strain produces a large amount of martensite resulting in a full unloading when the strain is driven down to 1%. A better behaviour shows the training at 2% of strain, in the sense that a minimal pre-stressing level is always granted during the cycles which simulate the externally induced vibration.

3.5.3 Test setup and experimental results

A shaking table test is performed to capture the accelerations at the top level of the structure. This will be used extract the modal frequencies of the wall. A pre-tension is then given to the wires that are installed along the wall longitudinal sides (Figure 3.14).

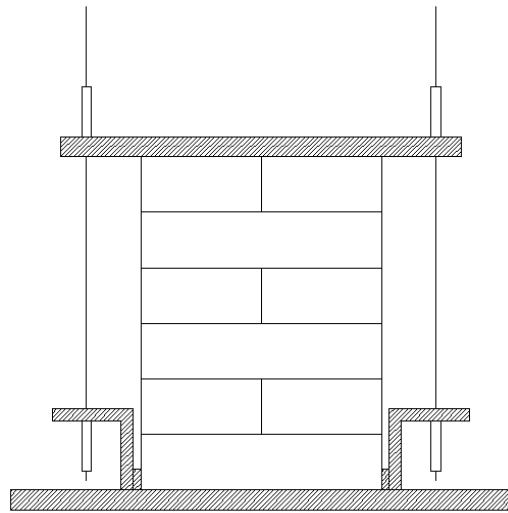


Figure 3.14: Cross-section of the tied wall.

An increasing number of couples of wires is considered by mounting: (a) a central wire on each of the opposite sides (Figure 3.15); (b) a wire at each specimen corner (Figure 3.16); and (c) three equidistant wires on each of the opposite sides (Figure 3.17). The test's setup is the same as the precedent driven on the wall in its virgin state. Recall that six different spans: 6, 30, 60, 75, 112.5 and 150 mm were proposed.

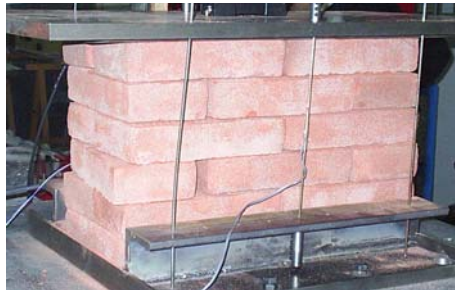


Figure 3.15: Tested wall with one central SMA wire.



Figure 3.16: Tested wall with two SMA wires at the corners.



Figure 3.17: Tested wall with three equidistant SMA wires.

Before presenting and discussing the results, the pre-stressing procedure of SMA wires is explained in the next sub-section.

3.5.3.1 Pre-stressing procedure

A special device (Figure 3.18), that was manufactured at the University of Pavia, was used to strain the SMA wires approximately in the middle of their super-elastic plateau (deformation from 1 to 5 %) (see Figure 3.19). The device is built in steel. The two strain gauges were implemented to built a half bridge circuit (that permit to eliminate the temperature effect). The idea is resumed in the fact that the applied pre-tensioning force on the SMA wires is naturally transmitted to the pre-stressing device, and using the LabView software, the strain readings (measured in millivolts) gathered from the applied force are

saved. The measured strains are then converted to the corresponding applied force by using an equation extracted from a preliminary calibration test drawn on the pre-stressing device.

The strain/force calibration process was achieved to know the transmitted pre-stressing force by simple reading on the measured voltage from the strain gauges. Using the load cell of the universal material testing machine, MTS 858 Microbionix II, also available at the Vibration Laboratory of Department of Structural Mechanics of the University of Pavia, a tension force ranging from 0 to 1.7 kN was applied to the SMA wires. The strain readings and its corresponding applied tension force were respectively saved using a laptop computer (serving as a central processing for strain monitoring, see Figure 3.20) and a desktop computer directly connected to the MTS machine. The converting equation is extracted from the graph shown in Figure 3.21 resulting from the experiment. The results are summarized in Table 3.5.

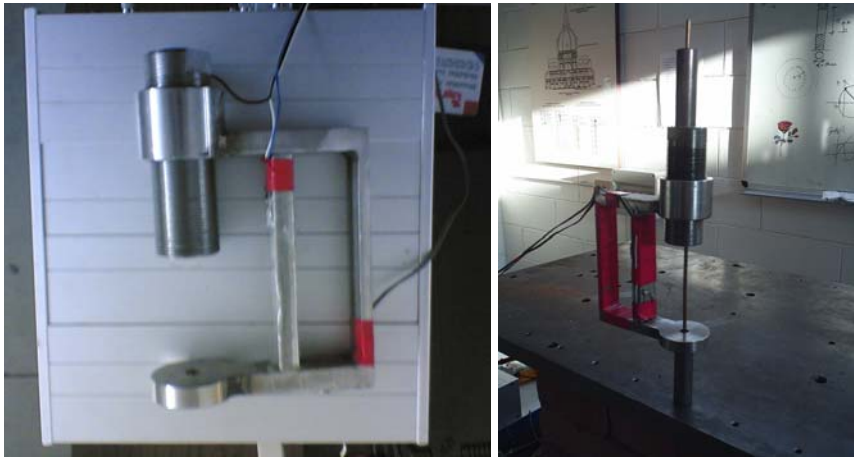


Figure 3.18: Device used for pre-stressing the SMA wires.

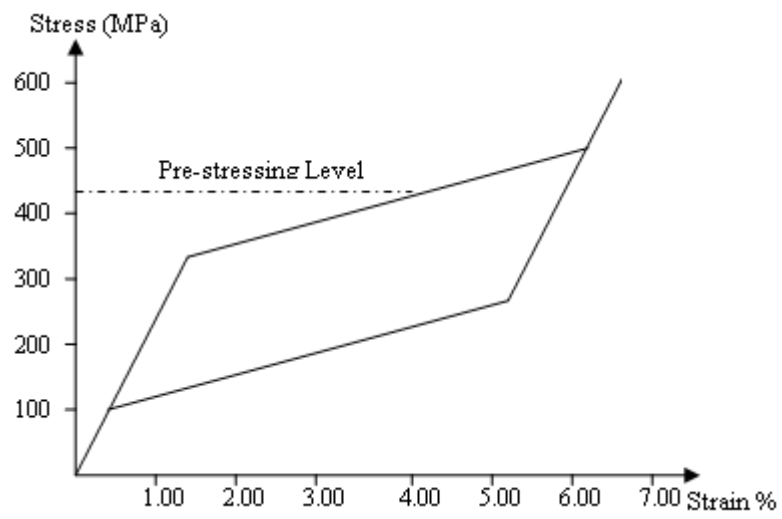


Figure 3.19: Pre-stressing stain level in SMA wires.

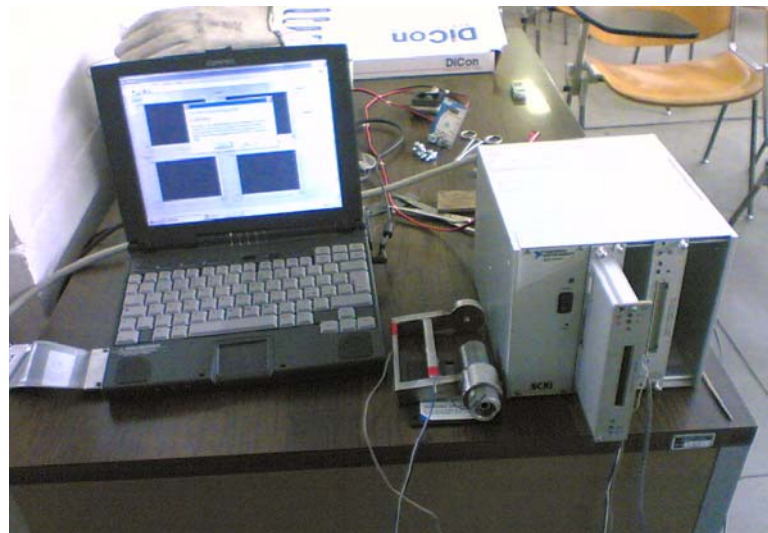


Figure 3.20: Equipment to monitor the strain in the pre-stressing device.

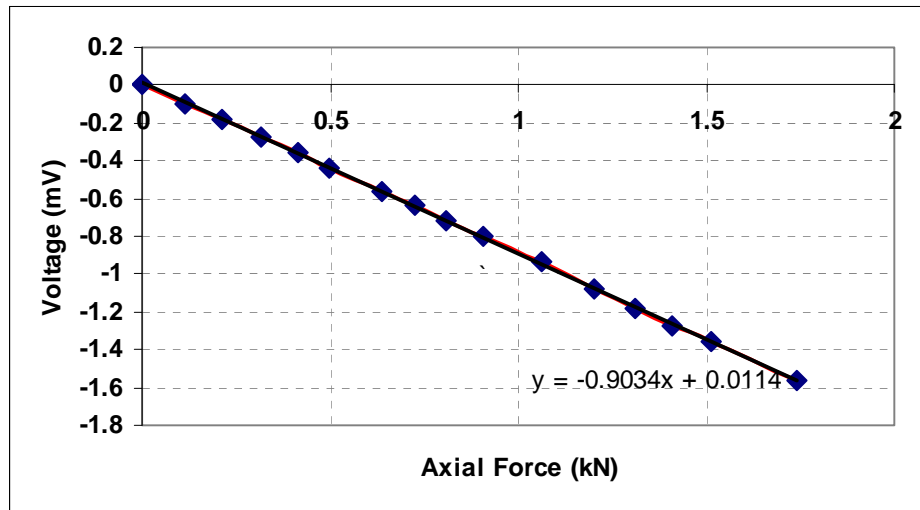


Figure 3.21: Axial force versus strain.

Table 3.5: Axial applied force and its corresponding strain.

Axial Force (kN)	Corresponding Voltage (mV)
0	0
0.116	-0.0977
0.215	-0.181
0.316	-0.273
0.416	-0.361
0.499	-0.439
0.638	-0.56
0.725	-0.64
0.806	-0.713
0.906	-0.801
1.06	-0.933
1.203	-1.08
1.31	-1.18
1.41	-1.27
1.515	-1.36
1.74	-1.56

3.5.3.2 The results

The results collected by applying the “N4Sid” state space algorithm to the recorded signals are summarized in Table 3.6, for all the considered structural configurations and excitation amplitudes.

Two considerations have to be made:

1. When using only two SMA wires, the test with excitation of highest intensity (large span) causes the wires to fail;
2. The excitation of lowest intensity (small span) produces signals whose amplitudes are so low that the machine resonance (at 20 Hz) corrupts the estimate of the system modal parameters. The Fourier transform plot in Figure 3.22, which refers to the case of six wires, gives evidence to the latter statement. As a consequence, the values in the first row of Table 3.6 are disregarded by the following elaborations, while the values in the second row are assumed as frequency estimates for the case of fully reacting cross-section.

Table 3.6: Resonant frequencies of the tied specimen, as computed by “N4Sid”.

Case	Span	Detected frequencies			
		Without SMA	With 2 SMA	With 4 SMA	With 6 SMA
1	6	11.10	18.53	19.17	20.2
2	30	8.74	15.46	15.79	16.95
3	60	8.73	13.56	13.77	16.00
4	75	6.45	13.40	13.76	15.69
5	120	4.78	12.84	13.57	15.49
6	150	4.60	-	13.66	15.02

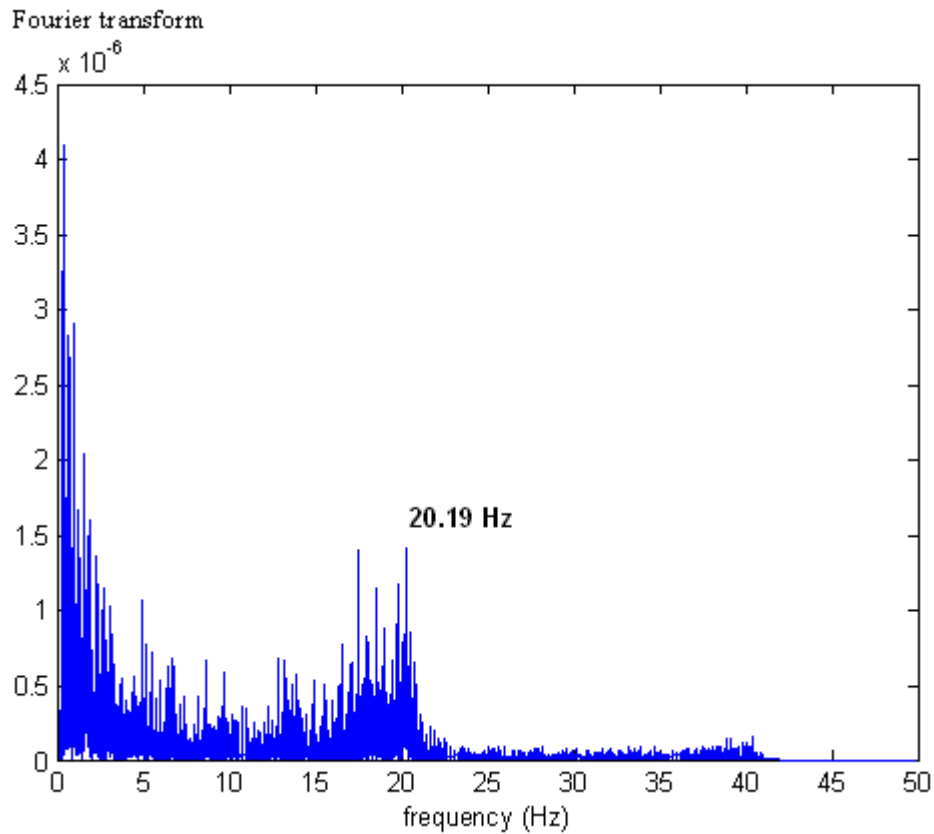


Figure 3.22: Fourier transform of the top acceleration, showing the interaction between the wall frequency and the testing machine resonance.

3.5.4 Elaboration of the numerical model

In the 3-D, 8-node, solid finite elements model of the wall discussed in the subsection 3.4.2, the pre-tensioning effect of the SMA wires is simulated by applying compressive forces at the top of the model. In other words, when working on the plateau of the alloy constitutive law, no structural elements need to be introduced in order to model the wires presence; only couples of forces are considered at the application points. Figures 3.23a, 3.23b, and 3.23c show the

finite element model with the forces corresponding to the cases of two, four, and six SMA wires, respectively.

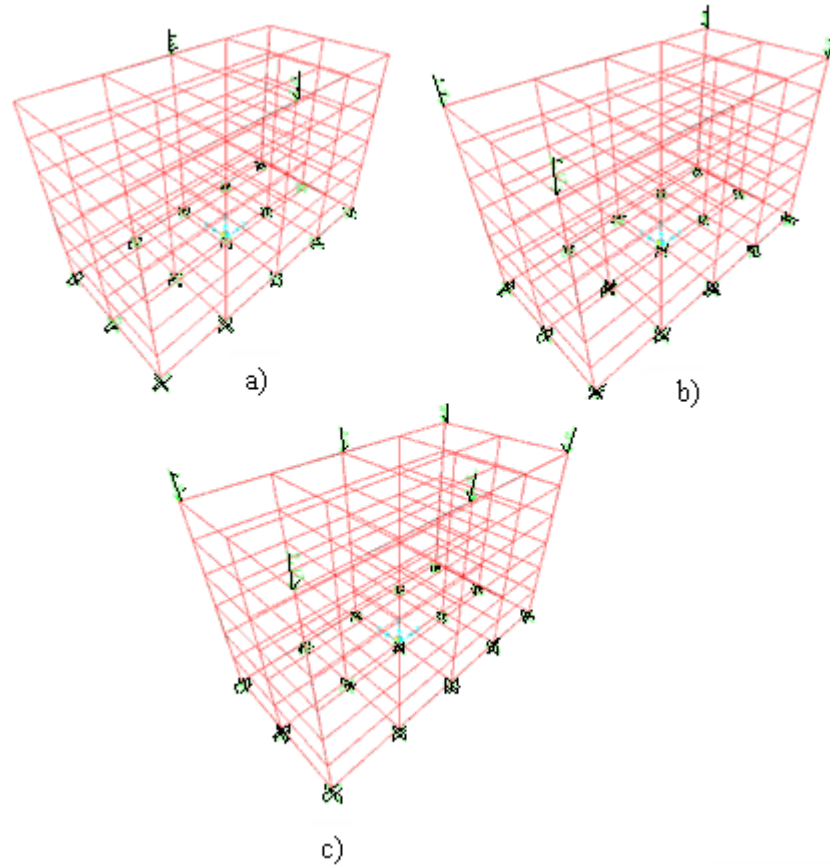


Figure 3.23: Finite element model under different configurations of the compressive forces: (a) 2 central forces, (b) 4 forces at the corners, (c) 6 forces (3 equidistant forces on each side).

At the measured strain level of 4%, the stress in the SMA wires is about 250 MPa, and it falls approximately in the middle of the super-elastic plateau. In order to simulate the corresponding compressive effect on the masonry wall, a value of 1.59 kN per wire is assigned to the forces in Figure 3.23.

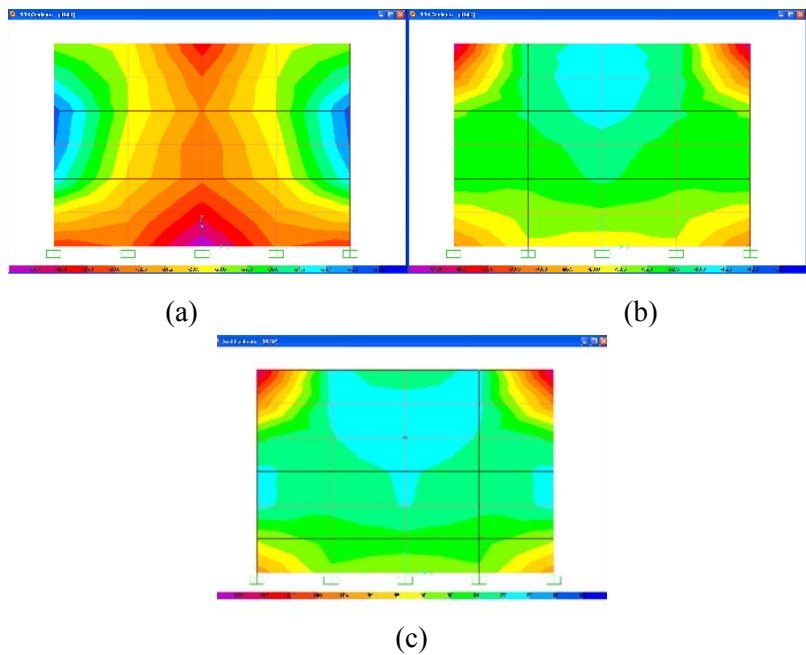


Figure 3.24: Lateral view of the stress flow under the three loading conditions of Figure 3.23: (a) two central forces, (b) four forces at the corners, (c) three equidistant on each side.

Figure 3.24 shows a lateral view of the vertical component of the stress flow in the masonry wall, under the three considered loading conditions. For the cases using a number of SMA wires greater than two, Figure 3.24b and 3.24c show a quiet homogeneous distribution of the stress induced by the pre-stressed ties. Conversely, in Figure 3.24a, the maximum stress values are reached only in the vicinity of the applied loads. Therefore, when only two wires are used, the regions in the vicinity of the devices must be distinguished from the rest of the structure.

3.5.5 Modal analyses accounting for the effective cross-section

The improvement due to the pre-stressing effect is now simulated by changing the equivalent modulus of elasticity, E_{eq} , of the wall. Once again, the aim is to achieve the same natural frequencies detected from the experimental tests (Table 3.7).

Table 3.7: Detected frequencies using N4Sid State space algorithm and equivalent Young modulus from the numerical model (FEM).

Number of SMA wires	Span [mm]	Estimated parameters		
		Experimental Frequency [Hz]	FEM Equivalent Young modulus [Mpa]	FEM Lumped mass [kg]
2	30	15.46	18.59 (20.66+16.53)	98.03
4	30	15.79	19.18	96.94
6	30	16.95	22.10	96.91

The calculations presented in sub-section 3.4.3 are repeated with N_{top} accounting for the additional pretension force. The results are organized in the Tables 3.8, 3.9, and 3.10 for the three cases of 6, 4, and 2 wires, respectively. In Tables 3.8 and 3.9, α is equal to 0.75 and the eccentricity is always lower than its upper limit.

Table 3.8: Justification of the detected frequencies by simple geometry modifications (the value in italic was obtained by interpolation): 6 SMA ties and $N_{top} = (0.5 + 9.569) \text{ kN}$.

Table peak acc. [m/s ²] (test)	Top peak acc. [m/s ²] (test)	Max. Eccentricity [m]	b_c [m]	$10^4 J_{min}$ [m ⁴] at the bottom	h_c [m]	k_c [kN/m]	Re-estimated Freq. [Hz]	Freq. [Hz] (test)
0.078	0.078	0.0002 <i>< b/6</i>	0.25	6.51	0.34	1098.21 (Eq. 1)	16.95	16.95
2.92	6.706	0.0209 <i>< b/6</i>	0.25	6.51	0.34	1098.21 (Eq. 1)	16.95	16.95
<i>5.84</i>	<i>13.9715</i>	0.0417 <i>= b/6</i>	0.25	6.51	0.34	1098.21 (Eq. 1)	16.95	
6.82	21.237	0.0662	0.176	2.28	0.222	1061.80 <i>> 0.75k</i>	16.67	16.00
8.24	25.655	0.0800	0.135	1.02	0.184	966.79 <i>> 0.75k</i>	15.90	15.69
11.44	28.462	0.0887	0.109	0.54	0.166	879.59 <i>> 0.75k</i>	15.17	15.49
13.84	31.153	0.0971	0.084	0.24	0.151	823.66 <i>= 0.75k</i>	14.68	15.02

Table 3.9: Justification of the detected frequencies by simple geometry modifications (the value in italic was obtained by interpolation): 4 SMA ties and $N_{top} = (0.5 + 6.380)$ kN.

Table peak acc. [m/s ²] (test)	Top peak acc. [m/s ²] (test)	Max. Eccentricity [m]	b_c [m]	$10^4 J_{min}$ [m ⁴] at the bottom	h_c [m]	k_c [kN/m]	Re-estimated Freq. [Hz]	Freq. [Hz] (test)
0.117	0.117	0.0006 <i>< b/6</i>	0.25	6.51	0.34	1098.21 (Eq. 3)	15.79	15.79
1.48	4.367	0.0209 <i>< b/6</i>	0.25	6.51	0.34	1098.21 (Eq. 3)	15.79	15.79
<i>2.94</i>	<i>8.690</i>	0.0417 <i>= b/6</i>	0.25	6.51	0.34	1098.21 (Eq. 3)	15.79	
4.40	16.726	0.0801	0.135	1.02	0.183	826.89 <i>> 0.75k</i>	14.70	13.77
5.65	20.625	0.0988	0.079	0.20	0.147	714.83 <i>= 0.75k</i>	13.67	13.76
8.69	23.861	0.1143	0.032	0.014	0.133	714.83 <i>= 0.75k</i>	13.67	13.57
9.47	24.095	0.1154	0.029	0.01	0.125	714.83 <i>= 0.75k</i>	13.67	13.57

Table 3.10: Justification of the detected frequencies by simple geometry modifications (the value in italic was obtained by interpolation): 2 SMA ties and $N_{top} = (0.5 + 3.19)$ kN.

Table peak acc. [m/s ²] (test)	Top peak acc. [m/s ²] (test)	Max. Eccentricity [m]	b_c [m]	$10^4 J_{min}$ [m ⁴] at the bottom	h_c [m]	k_c [kN/m]	Re-estimated Freq. [Hz]	Freq. [Hz] (test)
0.078	0.078	0.0004 < $b/6$	0.25	6.51	0.34	1098.21 (Eq. 1)	15.46	15.46
1.48	3.938	0.0356 < $b/6$	0.25	6.51	0.34	1098.21 (Eq. 1)	15.46	15.46
3.46	<i>4.667</i>	0.0417 = $b/6$	0.25	6.51	0.34	1098.21 (Eq. 1)	15.46	
4.44	13.139	0.118	0.019	0.01	0.123	693.03 = $0.75k$	13.39	13.56
5.77	16.882	> $b/2$	0	0.01	0.095	664.99	13.18	13.4
7.44	19.027	> $b/2$	0	0.01	0.083	601.81	12.96	12.84
0.078	0.078	0.0004 < $b/6$	0.25	6.51	0.34	1098.21 (Eq. 1)	15.46	15.46

In Table 3.10 (only two SMA wires), the eccentricity reaches the upper limit, α is equal to 0.75, and β is fixed at 0.6. For the case in which the wall is retrofitted by only two SMA wires (one on each longitudinal side), the simulation process is still pursued by changing the modulus of elasticity of the wall, E_{eq} , but a value of $(1.25E_{eq})$ is used to enhance the characteristics of the wall region near the wires emplacement. The E_{eq} value is, instead, assigned to the regions far away from the central wires, as suggested by Figure 3.24a. Indeed, the stress distribution reported in this figure shows in the middle higher values than laterally, and the ratio between the relevant stresses is about 1.25. Figure 3.25 illustrates the areas characterized by different values of the

equivalent Young modulus. Conversely, Figure 3.24b and 3.24c justify the assumption of a uniform distribution of E_{eq} in the entire wall specimen, for the cases where more than two wires are used.

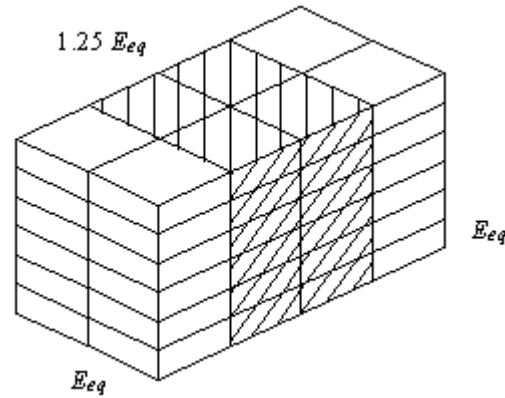


Figure 3.25: Central zone (dashed) with $1.25E_{eq}$ and lateral zones with E_{eq} .

3.5.6 Discussion

A three-dimensional diagram is given in Figure 3.26 It explains the relationship between the experimental frequencies obtained with different excitation amplitudes, and the number of wires used in the retrofit of the studied masonry wall.

The developments of this paper have emphasized that the dependence of E_{eq} on the vibration intensity is fictitious, because it is a consequence of the inability of the masonry to sustain tension stresses. If this aspect is directly taken into account by considering the reduced moment of inertia of the effective cross-section, a constant equivalent Young modulus can be assumed in the analyses, independently of the applied excitation intensity.

The graph of Figure 3.27 is therefore of most interest: it reports the variation of the equivalent modulus of elasticity E_{eq} versus the average stress in the wall (see Figure 3.8).

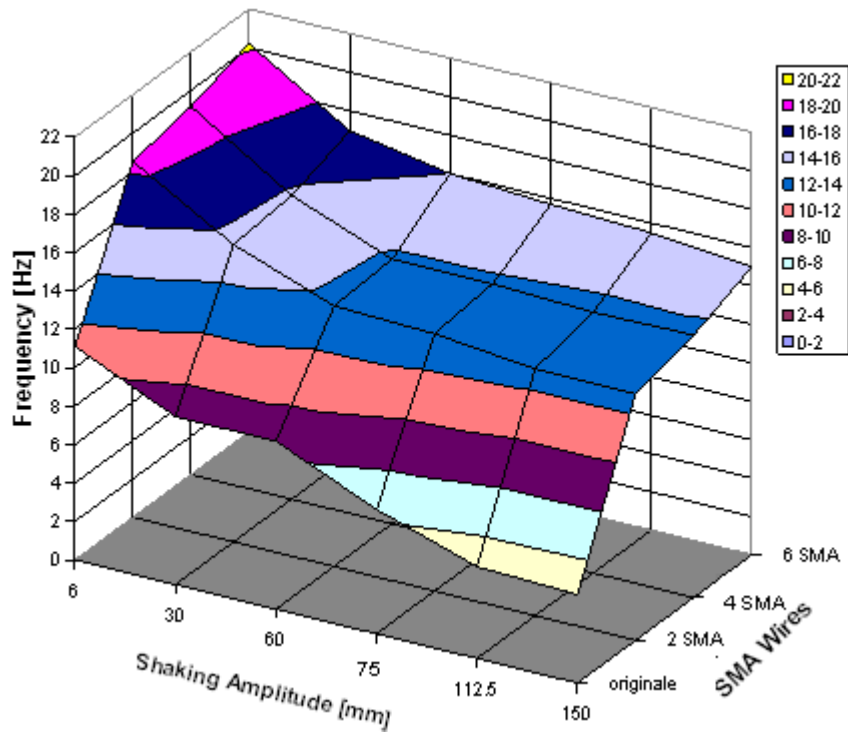


Figure 3.26: 3-D representation of the frequency vs. the amplitude and number of wires according to the experimental tests.

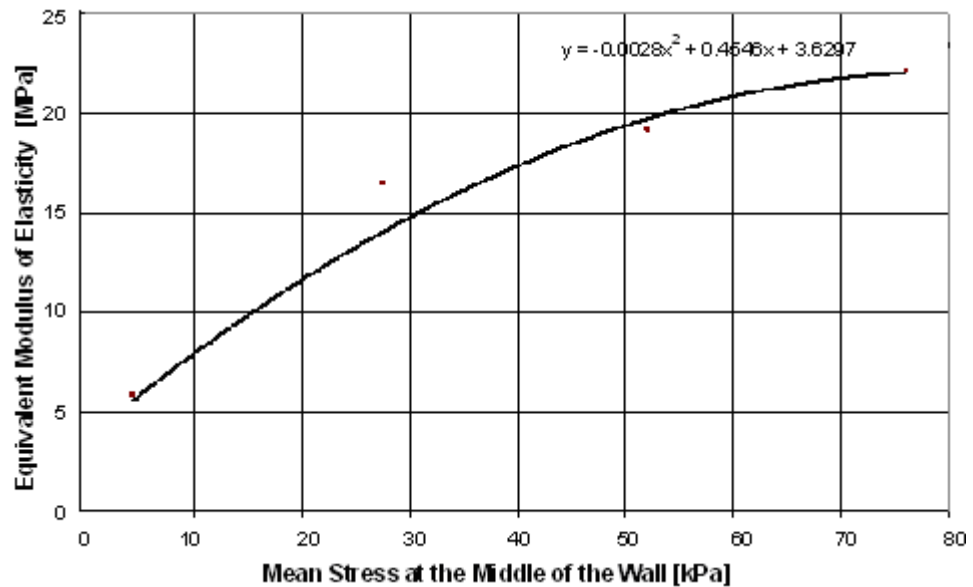


Figure 3.27: Equivalent modulus of elasticity vs. the stress in the wall for the cases of fully reacting section.

Nevertheless, the retrofitting not only improves the masonry behaviour by increasing the value of the equivalent Young modulus, but it also plays a very significant role in delaying any sort of progressive failure, thus providing to the structure the feature of robustness.

3.6 Comparison of using SMA versus steel ties

The response of the wall FEM incorporating the SMA ties under 20% of El-Centro earthquake applied in the weak direction is evaluated. In order to compare the effects of using steel instead of SMA ties, the analyses are repeated by inserting “link” elements at the same locations of the compressive forces in Figure 3.23. Under the assumption that the steel wires provide the same compressive effect as the SMA ties, the values of the masonry equivalent Young modulus are still the ones identified in Table 3.7. However, the steel devices not only enhance the structural performance by exerting linking forces,

but they also increase the structural stiffness. To account for both these effects, it is necessary to actually insert in the wall mesh additional elements modelling the steel devices and acting as elastic springs. For this purpose, the steel elastic properties ($E = 210$ MPa) are assigned to “link” elements of length $l = 33$ cm and diameter $\phi = 3$ mm. The resulting additional stiffness per wire is given by:

$$k_{(steelwire)} = \frac{E\pi\phi^2}{l} = 4498.10kN/m \quad (3.8)$$

The number of wires and their placement reflect the three retrofitting scenarios envisioned when using SMA ties. The results, obtained for the lowest excitation amplitude with reliable results (second row of Table 3.7), are collected in Tables 3.11 and compared to the corresponding cases using SMA ties. In particular, the system natural frequency and the maximum displacement of the wall top, in the same direction of the excitation, are reported. The driving excitation is here the 1940 El-Centro accelerogram scaled by 20%. When adopting steel wires, larger frequencies and smaller displacements are found with respect to the corresponding cases using SMA ties. As expected, a stiffer behaviour of the wall is achieved by adding steel elements, with negative effects in terms of energy dissipation.

Table 3.11: SMA ties versus steel ties.

Structural Configuration	E_{eq} [kPa]	Frequencies with SMA [Hz]	Frequencies with steel [Hz]	Max Displacement SMA [mm]	Max Displacement Steel [mm]
Original	5875	8.739	8.739	4.457	4.457
2 wires	20665	15.461	16.847	1.514	1.305
4 wires	19180	15.789	17.938	1.463	0.919
6 wires	22100	16.949	20.542	1.151	0.811

3.7 Conclusions

This chapter discusses the design aspects related to the adoption of SMA ties to sew structures that are essentially assembled by masonry blocks. The main drawback is the rising of inelastic permanent deformations under high intensity excitations.

The results of laboratory tests suggested the development of a numerical model incorporating the effects of the SMA devices. First, the structure is analyzed in its original state, without any retrofit attempt. The effects of several retrofitting solutions are then experimentally evaluated and included in the numerical model by accordingly changing the equivalent Young modulus. The response under 20% of 1940 El Centro accelerogram is compared to the ones of the initial structure and the structure mounting steel ties, in order to quantify the effectiveness of the retrofit and its advantages with respect to traditional techniques.

In conclusion, ties of SMA in austenitic phase offer three main benefits:

1. By prescribing that the assigned pre-tension must reach the plateau of the super-elastic constitutive law, no additional stress is transferred to the masonry at higher strain levels. Therefore, no springs need to be added to the numerical model, with consequent possibility of mutual displacements between the masonry blocks, i.e., energy dissipation;
2. Further energy dissipation is achieved by the hysteresis loop of the hyper-elastic stress - strain relation [Auricchio et al., 2001];
3. The ties are able to re-centre themselves in the initial position, without any residual displacement.

References

1. Auricchio F., Faravelli L., Magonette G. and Torra V. (Eds.) (2001). *Shape Memory Alloys: Advances in Modelling and Applications*. CIMNE, Barcelona.
2. Cardone D., Dolce M. and Nigro D. (1999). "Experimental test on SMA based seismic devices", *Proceedings of MANSIDE Project Final Workshop*, Rome, Italy.
3. Casciati F. (2006). "Structural monitoring for the diagnostic and the retrofitting of the monumental heritage", *Proceedings of Structural Health Monitoring and Intelligent Infrastructures*, Shenzhen University, Taylor and Francis, London, 49-54.
4. Casciati F. and Faravelli L. (2004). "Experimental characterization of a Cu-based shape memory alloy toward its exploitations in passive control devices", *Journal de Physique IV*, vol. 115, 299-306.
5. Casciati F., Casciati S. and Faravelli L. (2007). "Fatigue characterization of a Cu-based shape memory alloy", *Proceedings of the Estonian Academy of Sciences – Physics Mathematics*, vol. 56, no. 2, 207-217.
6. Casciati S. (2007). "Thermal treatment optimization for Cu-based shape memory alloys", *Proceedings of the First International Conference on Self-healing Materials*, Noordwijk, Netherlands.
7. Casciati S. and Faravelli L. (2003). "Thermo-mechanic properties of a Cu-based shape memory alloy", *Proceedings of SMART03*, Warsaw, Poland.
8. Casciati S. and Faravelli L. (2007). "Structural components in shape memory alloy for localized energy dissipation", *Computer & Structures*, vol. 86, no. 3-5, 330-339.
9. Casciati S. and Osman A. (2005). "Damage assessment and retrofit study for the Luxor Memnon Colossi", *J. Struct. Control Health Monitoring*, vol. 12, no. 2, 139-156.
10. Casciati S. and Hamdaoui K. (2008). "Experimental and Numerical Studies toward the Implementation of Shape Memory Alloy Ties in Masonry Structures", *J. Smart Structures and Systems*, vol. 4, no. 2, 153-169.

11. El-Borgi S., Choura S., Ventura C., Baccouch M. and Cherif F. (2005). "Modal identification and model updating of a reinforced concrete bridge", *Smart Struct. Sys.*, vol. 1, no. 1, 83-101.
12. Matlab [Computer Program]. Version 7 (R14). *The MathWorks Inc*; 2004. Available: <http://www.mathworks.com>.
13. SAP 2000. (2003). [Computer Program]. Version 8, Computer and Structures, Inc.

Chapter 4

Pre-stressed SMA Wires for Structural Retrofitting: the Aqueduct of Larnaca

4.1. Introduction

The richness of the Mediterranean area in archaeological sites and monuments suggests that many civilizations have flourished in the region. In addition of their vital role in the touristic and economic life, cultural heritage structures are valued for their historical importance and attractive construction. Unfortunately, the majority of them are in continuous and silent degradation that is usually due to aging, weathering and human factors. Countries of the basin, that have the privilege to own such structures, are interested in conserving them for future generations. This requires a high level of protection against any probable destructive event [Syrmakezis, 2002].

Preserving ancient monuments presents many difficulties and is directly related to the amount of damage that structure is expected to undergo through future earthquake actions. In civil engineering, this field is called “Structural Health Monitoring” (abbreviated SHM) [Doebeling et al., 1996], [Zonta, 2000], [Hamdaoui, 2006]. It tries to monitor the structure “health”, which may be defined as the level of deterioration or damage within a building.

During the last twenty years, monitoring and repair has become an economically viable alternative to the demolition and replacement of old civil engineering structures [Rytter, 1993] and a must for structures of high

importance. That's why; various researchers have put considerable efforts into the development of new, more reliable and less time consuming detection methods [Kullaa, 2003].

Any intervention in the structural system of monuments should be in a way that it neither violates their original form nor changes drastically their structural behaviour and most importantly should be reversible. In addition, the materials to be used must be compatible with the ones the monument is constructed of. The traditional seismic retrofitting techniques have the disadvantage that most of them violate the above conditions. An alternative to the above is the use of innovative seismic-protection techniques, such as shape memory alloy (SMA) based devices. Such devices can be made very inconspicuous and therefore not violating the form of the monuments and at the same time can be very effective in dissipating the energy generated by earthquakes and hence protect the monuments.

Several efforts have been made towards the study of the behaviour of SMAs [Faravelli, 2003], [Casciati and Faravelli, 2004], [Faravelli and Casciati, 2003]. The application of SMA and other innovative devices in protecting monuments are reported by [Biritognolo et al., 2000], [Crocì, 2000], [Chrysostomou et al., 2003], [Chrysostomou et al., 2004], [Chrysostomou et al., 2005], [Chrysostomou et al., 2008a] and [Chrysostomou et al., 2008b].

Such techniques have been evaluated within, "Wide-Range Non-Intrusive devices toward Conservation of Historical Monuments in the Mediterranean Area (WIND-CHIME)" project.

In this chapter the aqueduct of Larnaca in Cyprus is selected as a case-study to incorporate SMA devices. The monument is described, along with a system identification study which includes measurements and computational models. The models will be used to test the effectiveness of SMA pre-stressed devices and SMA dampers in protecting the monument from future catastrophic earthquakes. The results of the application of the SMA devices and their effects are presented and discussed.

4.2. Description of the monument

A description of the aqueduct is given by Philokypros in the Great Cyprus Encyclopedia. The aqueduct is known with the name Kamares, which means arches. It was the aqueduct of the city of Larnaca and it was built in the mid 18th century (Ottoman Empire period). This monument is located to the west of the city. It is known by the name Aqueduct of Bekir Pasa, from the name of the Turkish Pasa who built it (Figure 4.1).

Abu Bekir Pasa was a wealthy Turk who was the District ruler of Larnaca in 1746, and the same year he became the Governor of Cyprus until 1748. The construction started in 1746 and was completed in 1747. The construction cost was 50.000 grosia (6.200 pounds) and was undertaken in full by Bekir Pasa. It is noted by Mass Latri, that stones from the ancient city of Kition were used for the construction of this large (for that period of time and conditions prevailing in Cyprus) monument.

The aqueduct was built to provide water to the city of Larnaca and to its port, both from small springs and the river Tremithos. For a long length of its course, which is about 10.5 km, the water was transported in an open duct, but in three places where the ground was low, arches were built, on top of which runs the duct. These three parts consist of 30, 12 and 33 arches, giving a total of 75 arches. Their width and height varies.

The aqueduct operated during the British occupation of the Island of Cyprus, until 1939, when the supply of water to the city of Larnaca was effected through pipes. A view of the aqueduct was printed on the back side of the Cyprus pound that circulated in 1961 and was replaced recently.



Figure 4.1: The aqueduct of Larnaca.

4.3. Structural health monitoring and System identification

4.3.1 Introduction to SHM

SHM methods are either based on the “on-line” or “periodical” measurements. Of course, the on-line measurements [Doebbling et al., 1996] category is the most reliable but also the most expensive one. Therefore, many scientists have concentrated their research on the development of reliable methods based on periodical inspection [Caicedo, 2001].

The periodical inspections aim to detect deteriorations at an early stage to guarantee adequate safety and low cost of repair. Short descriptions of the mainly utilized method for structure’s monitoring are provided in the next section.

4.3.1.1 Periodic Visual Inspection

The predominant examination approach utilized in either civil engineering structures (buildings, bridges, off-shore platforms or dams) or monuments is the “periodic visual inspection” [Beck and Dionisio, 2001]. This inspection is imperative to determine how much damages the structure has experienced whenever an earthquake occurs. The examination work is generally done in two phases [Abed et al., 2005]. The first one, named “phase A”, consists of a summary evaluation of damages. At this stage, engineers and experts have to fill technical sheets evaluating the state of deterioration and writing reports adopting the first urgent measures. Edifices are classed here according to their damages into three categories: green, orange, or red. In the second phase (or “phase B”), a profundity heighten study specifying techniques of repair is drawn. This second phase is concern only with constructions signed in orange.

However, in most cases, this manual process is hindered by the fact that the structural elements (beams, columns, connections...) are usually covered by non-structural ones. At this time, significant efforts are necessary to access these areas for visual inspection [Dyke et al., 2000]. Alas, the situation if undetected would pose extreme danger for occupants during future earthquakes.

In certain cases, visual inspections can be performed using “localized experimental methods” (known as SHM localized techniques) such as radiographs, X rays, magnetic or ultrasonic methods but these are local in nature and can not provide information on the overall health of the structural system.

4.3.1.2 Vibration-Based Health Monitoring

An alternative to visual inspections and localized tests techniques, “SHM based on vibration signals” (or SHM global techniques) is being aggressively investigated in various engineering disciplines [Fritzen, 2005]. It is based on the theory saying that each structure has its typical dynamic behaviour which may be addressed as vibrational signature [Ambient Vibration Response, 2008], [Zonta, 2000], and any damage in the structure leads to change (decrease) in the

load carrying capacity, consequently, changes in the physical properties (mass, stiffness or damping). That modification has a significant impact on the dynamic behaviour of the whole structure.

This can be illustrated by Figure 4.2; it shows two frequency response functions of a vibrating pre-stressed reinforced concrete (PRC) panel, fixed at the edges [Zonta, 2000]. Measurements were taken at the middle-span. The undamaged panel is referred by the bold line, the light one to the panel after cracking. It is obvious that there is a slight difference in frequencies before and after damaging, that suggests the use of the dynamic response characteristic for the evaluation of quality and structural integrity.

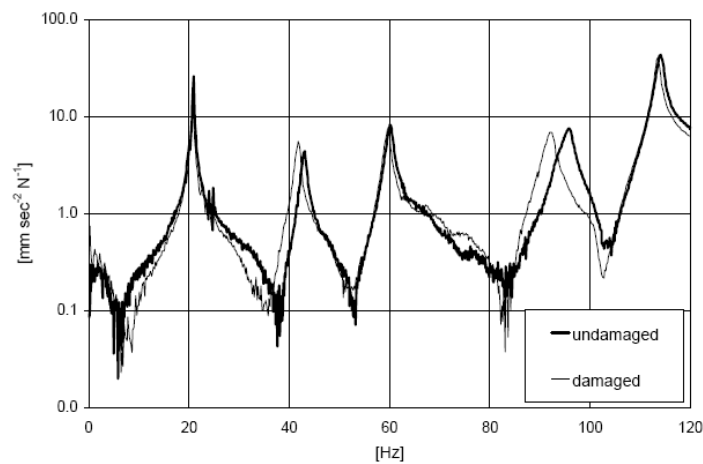


Figure 4.2: Change in dynamic response of a pre-stressed reinforced concrete (PRC) element before and after damage [Zonta, 2000].

Global SHM system consists of a set of sensors (accelerometers, anemometers, inclinometers, displacement transducers, temperature sensors, strain gauges) distributed over the structure for system identification. By using cables, each accelerometer communicates with a data acquisition system which is connected to a central processing unit.

The main advantage of SHM global techniques is that measurements at only one location are enough to assess the state of the whole structure. Also, they are very attractive to civil engineers because they can be used devoid of direct admittance to the structural members and no previous information of damage in the structure is needed, consequently, time and cost to assess damage in a structure is minimized.

Note that the basic principles of health monitoring are the same in bridges, buildings or any other type of structure. A historical building is usually built of traditional natural materials collected in the area of the structure, with techniques based on experience, and without any special design. These structures are generally more complex than other ones [Wenzel, 2006] and are constructed from less defined materials that have nonlinear behaviour under heavy load

The present thesis focuses on global techniques. From this point, the term of SHM will refer to global techniques.

4.3.2 SHM and System Identification

In vibration-based health monitoring, lots of measurement data are generated. Therefore, there is need to compress the amount of data by estimating an experimental model of the structure that essentially contains the same information as the original vibration data. The process of finding a model from data is called System Identification (abbreviated SI).

The main idea of SI is modelling dynamic systems by studying their behaviour from experimental data. This general definition indicates that system identification is applicable in many fields [Andersen, 1997]:

- In medicine: Analysis of dynamic biological functions, such as heart rate control and effects of drugs;
- In industry: Identification of industrial processes and industrial plant control;
- In economic science: Modelling of stock prices in economics;

- In mechanic industry: Performance study of automotives, ranging from aerospace vehicles and automobiles to railway carriages;
- In civil engineering: Identification of the dynamic properties of civil engineering structures, such as towers, dams, bridges, offshore structures.

The first step to do in SI of civil engineering structures is the modal analysis. It is based on the analysis of modal parameters of built structures from experimental data, and consists to apply sufficient magnitude of force to the structure in order to produce useful response amplitudes that lead to more prominent excitation of the modes of vibration. Modal parameters are:

- Modal frequencies or natural frequencies (eigenvalues);
- Modal vectors or mode shapes (eigenvectors) that is the way the structure moves at a certain natural frequency;
- Modal damping or damping ratio that is the degree to which the structure itself is able to damp out vibrations;
- Modal scaling that is characterized by modal masses and residues.

The second step is used for “health monitoring” of structures. It consists of measuring the dynamic characteristics of the structure during its life time, and uses them (dynamic characteristics) as a basis for identification. The experimentally obtained periodic modal testing provides information about the structure’s state of damage during its existence since they are directly related to the mass and the stiffness. Comparing the series of sets of modal parameters offer us an idea about the structure’s health.

4.4. Experimental Analysis

4.4.1 Ambient vibration test

In theory, the measurement of structural parameters can be best made on a structure subjected to strong earthquake and being able to conduct strong motion recordings of the input forces and of the response through instrumentation [Magpantay, 2006]. However, this requires continuous monitoring of a structure since predicting the occurrence of earthquakes is, up

to now, unattainable by science. Fortunately, several experimental techniques are available now to excite artificially the structures. The basic idea of tests such as forced vibration, shaking table, transient vibration, micro-tremor excitations, ambient vibration and free vibration [Aghakouchak et al., 2000] is to apply sufficient magnitude of force to the structure in order to produce useful response amplitudes, and study their dynamic characteristics.

For complex, large and heavy civil engineering structures, the artificial excitation is simply impossible (as in the case of tall buildings, towers, bridges etc.). This intricate task can be avoided by using methods that identify the structure exclusively on the basis of measurements of the output caused by ambient vibration [Wenzel and Pichler, 2005]. For this kind of tests, only output vibrations are recorded.

As said in previous sections, experimental modal analysis of historical structures [El Borgi et al., 2005] is generally carried out using non-destructive output-only measured data. Furthermore, these structures are generally more difficult to model than others, and are constructed from inhomogeneous materials that have nonlinear behaviour under heavy load.

4.4.2 Testing procedure and FE model

It was decided to measure the dynamic properties of the last part of the aqueduct, which consists of 33 arches and is close to the city of Larnaca.

The aqueduct on its south west side is supported laterally by two buttresses, one between the 19th and 20th arch and the other between the 29th and 30th arch. Due to the massive nature of these buttresses it seemed prudent to make measurements between the buttresses since they provided firm out-of-plane support to the aqueduct. In addition, the aqueduct between the buttresses is practically straight with a length of 104 m.

In order to obtain the periods of vibration of the aqueduct so as to be able to tune the computational model, the Kinematics Model VSS-3000 Vibration

Survey System was used, together with a triaxial EpiSensor force balance accelerometer (model FBA ES-T). The EpiSensor has user-selectable full-scale recording ranges of ± 4 g, ± 2 g, ± 1 g, $\pm 1/2$ g or $\pm 1/4$ g and a bandwidth of DC to 200 Hz. The recording range used in this work was $\pm 1/4$ g and the sampling rate 1000 points per second.

The dynamic characteristics of the aqueduct were determined twice: the first in June 2004 and the second in May 2007. The need for this arose from the fact that the application of the SMA devices on the structure (May of 2007) was performed three years after the characteristics of the structure were determined, and it was therefore considered prudent to re-determine those characteristics so as to confirm the starting point. As it will be explained below, there was a considerable difference in the behaviour of the monument between those two measurements. The main contributing factor was the effect of the level of the water in the nearby salt lake. In June 2004 the lake was dry while in 2007 the water level was high and it was obvious that the foundation of the structure was under the ground water table. Both results are presented below.

Following the measurements on the aqueduct and the establishment of the first few periods of the structure, for both cases, computational models were developed so as to model the measured behaviour of the aqueduct as closely as possible. The program SAP2000, (2007) was used with shell elements. First, the results of the initial test were used and by considering the foundation as fixed, the modulus of elasticity was varied until agreement between the measured and the calculated frequencies was reached. Considering this as the initial condition, springs were added at the foundation to simulate the soil-structure interaction. The stiffness of the out-of plane springs were varied until agreement of the results was reached. The details of these two model updates are described below.

4.4.2.1 June 2004 test

Measurements

The EpiSensor was positioned at 21 different locations on the aqueduct indicated with numbers 1 to 21 (see Figure 4.3), and a rubber impact hammer was used to induce vibrations in the aqueduct in addition to ambient vibrations. One impact location was used indicated in Figure 4.3 with the letter A. The x -axis, y -axis and z -axis of the EpiSensor were aligned with the longitudinal, perpendicular to its plane and vertical directions of the aqueduct, respectively.

The measurements were analyzed using the software DaisyLab 5.6. A Fast Fourier Transform (FFT) was used with a low pass Butterworth filter of 25 Hz and a Hanning data window. The results have shown that at least the first six frequencies recorded were in the y -direction. This is further verified from the results obtained by the computational model described later in this chapter. Figures 4.4 and 4.5 show the FFT for positions 7 and 19, respectively.

From the results it is clear that the first six dominant frequencies arranged in increasing order of magnitude are: 2.08 Hz, 2.20 Hz, 2.38 Hz, 2.56 Hz, 2.81 Hz, and 3.11 Hz (see Table 4.1). The corresponding periods in decreasing order of magnitude are: 0.48 s, 0.45 s, 0.42 s, 0.39 s, 0.36 s, and 0.32 s. It should be noted that, as expected, these values appear consistently irrespective of the location of the instrument, except for the frequency 2.08 Hz, which starts appearing after location 14 (see Figure 4.3). The reason for this is closely related to the first mode shape obtained by the computational model that will be presented in the next section.

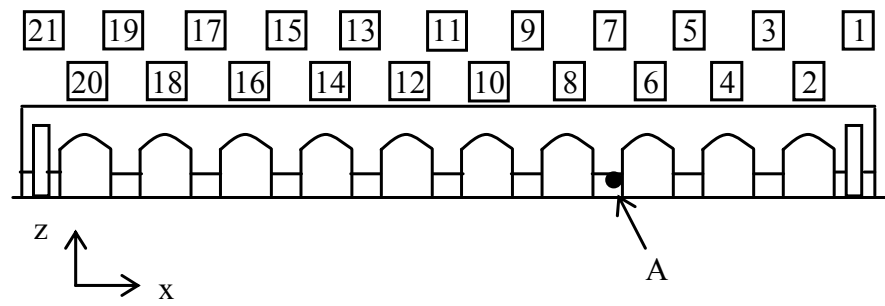


Figure 4.3: Location of accelerometer and excitation.

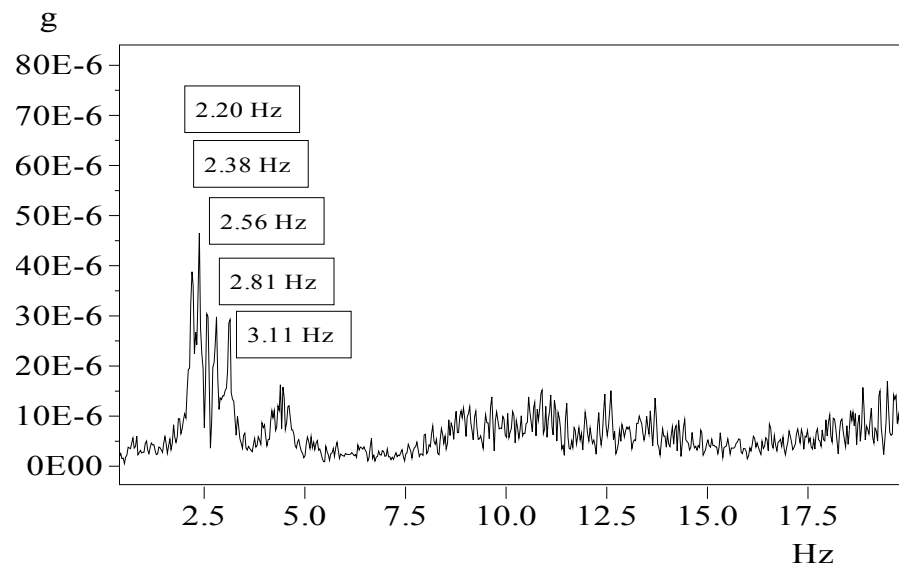


Figure 4.4: FFT for position 7 (Figure 4.3).

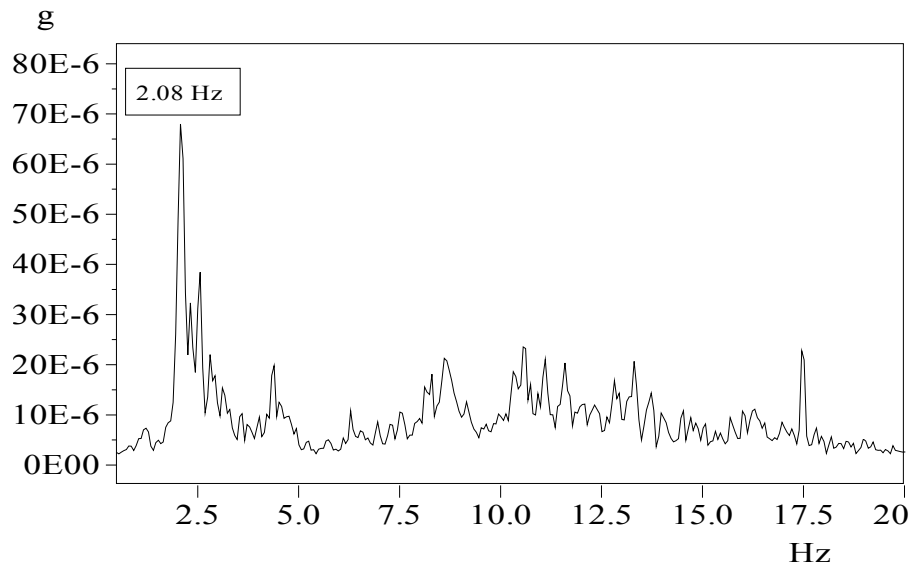


Figure 4.5: FFT for position 19 (Figure 4.3).

Table 4.1: Measured frequencies of vibration of aqueduct (June 2004).

Mode	Frequency (Hz)	Period (s)
1	2.08	0.48
2	2.20	0.45
3	2.38	0.42
4	2.56	0.39
5	2.81	0.36
6	3.11	0.32

FE built Model

The aqueduct is made of calcareous sand-stone (based on information obtained from the Geological Survey Department of Cyprus, such stones have unit weight of the order of 21.6 kN/m³) built in isodomic construction (see Figure 4.6). The modelling of such a construction presents many problems especially in establishing the modulus of elasticity of the matrix. The methodology used in

this research was to vary the modulus of elasticity of the shell elements representing the wall until the periods calculated by the eigenvalue analysis matched, as closely as possible, the measured ones.



Figure 4.6: Pier of the aqueduct.

The span of the arches varies from 5.05 m to 6.60 m while the height of the bottom of the channel varies from 6.75 m (position 1 in Figure. 4.3) to 9.4 m (position 21 in Figure 4.3). The thickness of the aqueduct is on the average 1.85 m for the lower part of the aqueduct (varying in height from 1.95 m to 4.10 m) and 0.85 m for the top part of the aqueduct. The total thickness of the two sides of the channel and its depth is on the average 0.50 m.

A first trial analysis of the model using a modulus of elasticity of 2 kN/mm², resulted in a fundamental period of vibration of 0.39 s. The relationship between the original fundamental period of vibration, $T_{original}$ and modulus of elasticity, $E_{original}$, and the targeted ones ($T_{targeted}$ and $E_{targeted}$) is given by Eq. (3.1)

$$\frac{T_{original}}{T_{targeted}} = \sqrt{\frac{E_{targeted}}{E_{original}}}. \quad (3.1)$$

Substituting in Eq. (3.1) the original values given above and the targeted period of vibration of 0.48 s obtained from the signal processing, the modulus of elasticity was then calculated as 1.35 kN/mm².

The eigenvalue analysis of the model with the new modulus of elasticity resulted in the mode shapes shown in Figure 4.7 and the following periods of vibration: 0.48 s, 0.44 s, 0.41 s, 0.38 s, 0.36 s and 0.33 s. The comparison of the measured and computed periods of vibration for the first six modes is shown in Figure 4.8. It should be noted that there is a very close agreement between the calculated and the measured periods of vibration. All of these modes have mass participation factor in the y -direction. The analysis has shown that the first mode in the x -direction appears in the 17th mode while in the z -direction no mode appears in the first forty modes of vibration.

The fact that the first period of vibration (Figure 4.5) started appearing in the recorded signals after point 14 is confirmed by the computational model in which the first mode of vibration consists, primarily, of movement of the arches in that region (Figure 4.7a).



(a) First mode



(b) Second mode



(c) Third mode



(d) Fourth mode



(e) Fifth mode



(f) Sixth mode

Figure 4.7: Perspective plan view of the first six modes of vibration (Model for June 2004).

Another important observation is that points 1 and 21, at which the buttresses are located, behave as fixed points due to the high lateral stiffness provided by the buttresses (Figure 4.7). This supports the decision of analyzing only this part of the aqueduct ignoring the rest of the structure.

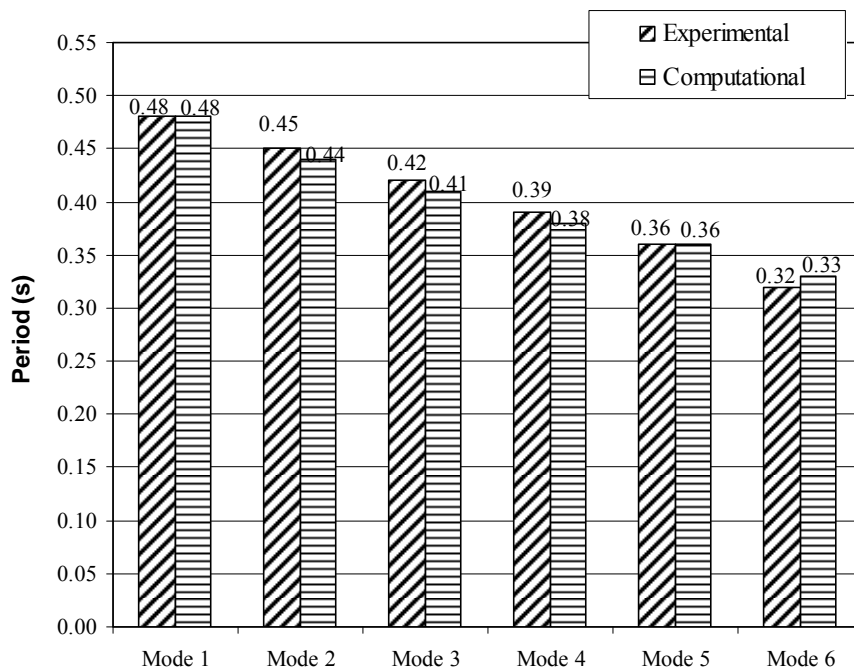


Figure 4.8: Comparison between measured and calculated periods of vibration (June 2004).

4.4.2.2 May 2007 test

Measurements

Two EpiSensors were positioned at 2 different locations on the aqueduct indicated with numbers 1 and 2 (see Figure 4.9), and a rubber impact hammer was used to induce vibrations in the aqueduct in addition to ambient vibrations. One impact location was used indicated in Figure 4.9 with the letter A. The x -axis, y -axis and z -axis of the EpiSensors were aligned with the longitudinal, perpendicular to its plane and vertical directions of the aqueduct, respectively.

The measurements were analyzed using the software DaisyLab 9.0. A Fast Fourier Transform (FFT) was used with a low pass Butterworth filter of 10 Hz,

a high pass Butterworth filter of 0.6 Hz and a Hanning data window. Figure 4.10 shows the FFT for position 1.

From the results it is clear that the first five dominant frequencies arranged in increasing order of magnitude are: 0.73 Hz, 0.85 Hz, 1.01 Hz, 1.25 Hz, and 1.43 Hz (see Table 4.2). The corresponding periods in decreasing order of magnitude are: 1.37 s, 1.18 s, 0.99 s, 0.80 s and 0.70 s. It should be noted that, as expected, these values appear consistently both in location 1 and location 2.

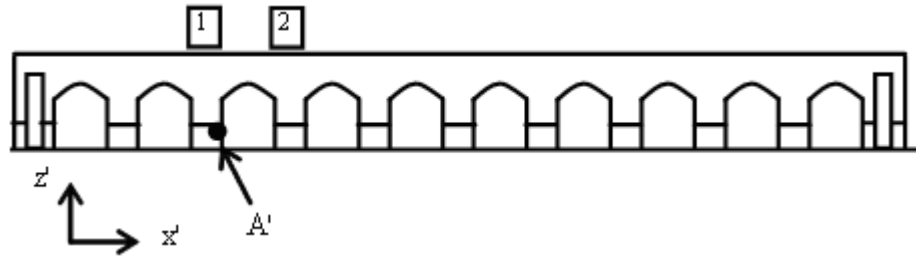


Figure 4.9: Location of accelerometers and excitation (May 2007).

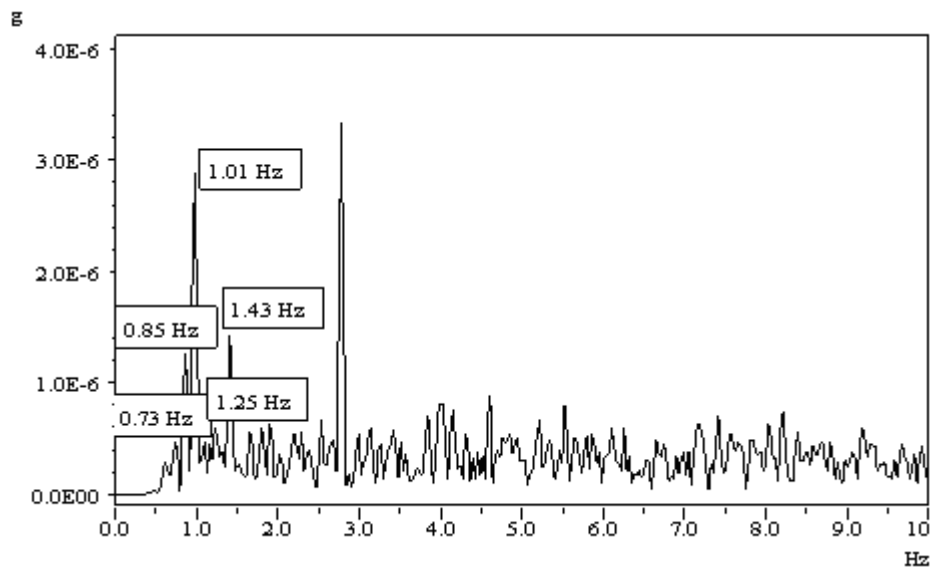


Figure 4.10: FFT for position 1 (Figure 4.9).

By comparing the values of Tables 4.1 and 4.2 we can see that there is a considerable shift of the measured frequencies of the aqueduct from 2.08 Hz in 2004 to 0.73 Hz in 2007. This shows a softening of the structure since the fundamental period of vibration shifts from 0.48 s to 1.37 s. Since the properties of the structure have not been changed, then a possible explanation is the soil-structure interaction.

Table 4.2: Measured frequencies of vibration of aqueduct (May 2007).

Mode	Frequency (Hz)	Period (s)
1	0.73	1.37
2	0.85	1.18
3	1.01	0.99
4	1.25	0.80
5	1.43	0.70

Since the aqueduct is located at the shore of a salt lake, the level of the water of the salt lake affects the condition of the foundation of the aqueduct. In 2004 the measurements were performed in the end of June when the salt lake was dry. In 2007 the salt lake was full due to some out-of-season rainfall giving rise to a high ground-water table. Therefore, in the latter test the foundation of the aqueduct was under the ground water table. This was confirmed by digging close to the foundation and finding out that the ground water table was a few centimetres below the ground level.

FE built model

The model developed in the previous section was used as the starting point for the updating of the finite element model to match the results of the signal processing of May 2007. The supports were replaced by springs so as to be able to vary their stiffness in order to simulate soil-structure interaction. No attempt was made to obtain the properties of the soil and use soil-structure interaction models to simulate the behaviour. Rather, a trial and error approach was used.

At first very stiff springs were used that gave the same results as the ones obtained in the previous section with fixed supports. The stiffness for the linear springs was set to 1×10^5 kN/m while the one for angular ones to 1×10^8 kNm/degree.

Then, the angular spring that corresponded to out of plane rotation was changed until matching was obtained between the fundamental period of vibration obtained from the measurements and the eigenvalue analysis of the model. To avoid repetitive calculations three trials were made, with spring constants 2000, 5000 and 10000 kNm / degree which gave periods of vibration 2.21 s, 1.56 s and 1.19 s, respectively. Then a regression equation (Eq. (3.2)) was obtained using the above results.

$$T = 41.278 \times K^{-0.3847} \quad (3.2)$$

Substituting in Eq. (3.2) the targeted period of 1.37 (Table 4.2), the resulting spring constant is $K = 7000$ kNm/degree.

The eigenvalue analysis of the model with the above spring constant resulted in the mode shapes shown in Figure 4.11 and the following periods of vibration: 1.37 s, 1.16 s, 0.98 s, 0.80 s and 0.68 s. The comparison of the measured and computed periods of vibration for the first five modes is shown in Figure 4.12. It should be noted that there is a very close agreement between the calculated and the measured periods of vibration.



(a) First mode



(b) Second mode



(c) Third mode



(d) Fourth mode



(e) Fifth mode

Figure 4.11: Perspective plan view of the first six modes of vibration (Model for May 2007).

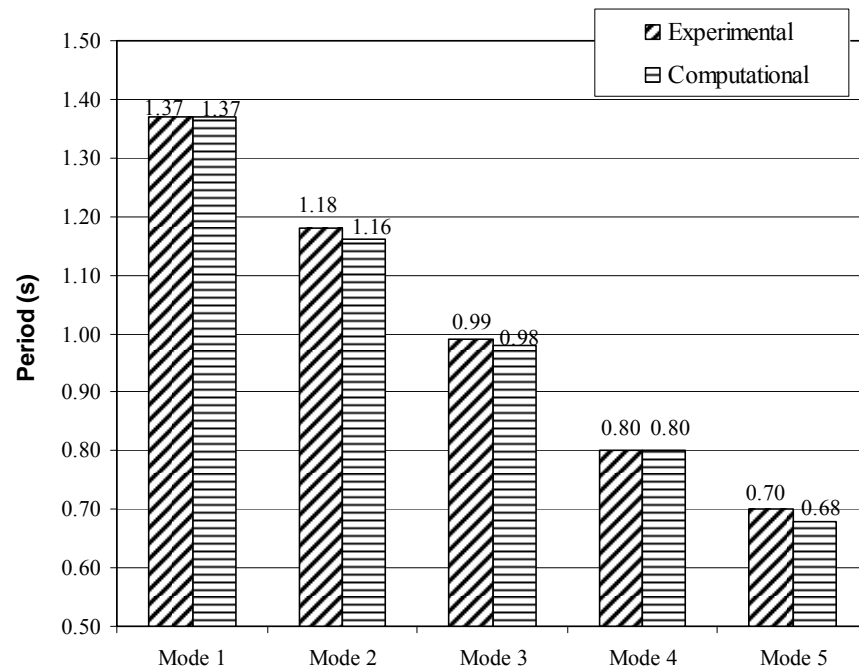


Figure 4.12: Comparison between measured and calculated periods of vibration (May 2007).

4.5 Measurements with using SMA wires

4.5.1 Characteristics of the utilized SMA wires

The pre-tensioned wires used in this study are of diameter 3.5 mm and are labeled AH140. As the implemented ties in the tested masonry wall (discussed in the previous chapter), SMA have the same chemical composition by weight that are, again:

Al = 11.8%; Be = 0.5%; Cu = 87.7%.

The transformation temperatures provided by the French producer are, again:

$$M^{0s} = -18^{\circ}\text{C}; \quad M^{0f} = -47^{\circ}\text{C};$$

$$A^{0s} = -20^{\circ}\text{C}; \quad A^{0f} = 2^{\circ}\text{C}.$$

Recall also that “M” and “A” mean here the martensite and austenite temperatures respectively, where the indices “s” and “f” denote respectively “start” and “finish”.

These wires were also subjected to a thermo-mechanical treatment. They were heated in an oven at 850°C for 3 minutes (Table 6.4), then cooled to ambient temperature by direct immersion in water. They were also treated for 120 minutes in an oven at 100°C, and cooled again to ambient temperature. It is interesting to note that the thermal treatment has as an effect the reduction of the stress of the material from 500 MPa to 250 MPa for the same strain of 6%.

4.5.2 Experimental setup

4.5.2.1 Methodology

After obtaining permission from the Antiquities Department of Cyprus for applying the SMA pre-stressing devices on the aqueduct, an effort was made to design the experiment in such a way so as to minimize any damage that the experiment would cause on the monument. For this reason it was decided to fix the wires at the base of one of the piers using bolts and at the top to support the wires on a rigid base (Figure 4.13) that would transfer the force onto the aqueduct. This of course resulted in a setup that is not inconspicuous, but since this experiment was performed to test a hypothesis it is considered acceptable. In the event that such devices will be applied on the monument, then a discussion should be made with the Department of Antiquities to find the most inconspicuous way of applying the devices that would also serve the purpose of their application.



Figure 4.13: Rigid base to support the upper end of the SMA pre-stressing assembly.

Twenty 60 cm long SMAs, as the ones shown in Figure 4.14, were prepared by adding fixing devices at each of their ends. These devices were then connected to steel strands (Figure 4.15) that extended from the top to the bottom of the pier of the aqueduct.



Figure 4.14: Sixty centimetres long SMA wires of diameter 3.5 mm.



Figure 4.15: Connection of the steel cable to the SMA wire.

In order to be able to apply a pre-stressing force, the pre-stressing devices shown in Figure 4.16 were used by placing them along the length of the steel strand. Two such devices were used for each strand, in order to be able to provide the required strain, taking into account the elongation of the SMA wire and that of the steel strand.



Figure 4.16: Pre-stressing device.

The use of 10 wires on each side of the pier would require the drilling of 20 holes. This was considered excessive damage to the monument, therefore it was decided to connect two wires on a rigid pipe, which was in turn connected to one steel strand. This resulted in a decrease of the required holes from 20 to only 10.

Figure 4.17 shows 10 of the wires hanging from the rigid base at the top of the pier. Every two wires are connected to a steel pipe which is in turn connected to one steel strand. Each of the strands is connected to two pre-stressing devices,

which are placed in series (Figure 4.18), which is anchored on a bolt at the bottom of the pier (Figures 4.18 and 4.19).

Having setup all twenty wires, tensioning of the wires took place in a symmetric manner. First the four central wires were tensioned. At first the pre-stressing devices were used to remove any slack that existed in the assembly. When that was done, the initial length of the SMA devices was measured, as shown in Figure 4.17. This length was used to calculate the strain in the wire as the tensile force was increased by turning the pre-stressing devices. It was decided that a 2% strain would be applied in the SMA wires since that constituted the centre of the plateau.



Figure 4.17: SMA wires supported at the rigid base at the top of the pier of the aqueduct.



Figure 4.18: Pre-stressing devices used to apply tension in the assembly.



Figure 4.19: Bolts used to fix the assembly at the bottom of the pier.

As it can be observed from Figure 4.17 only two of the SMA wires (on each side of the pier) appear to be stretch since the experiment started by applying a pre-stressing force to only 4 of the 20 wires (wire no. 5, 6, 15 and 16 in Figure 4.20). Two more measurements were taken and in each case 8 more wires (4 on each side) were pre-stressed giving a total of 12 and 20 wires, respectively, by

stressing first wires no. 1, 2, 9, 10, 11, 12, 19 and 20, and then wires no. 3, 4, 7, 8, 13, 14, 17 and 18. Then an unloading cycle took place by removing first the central 4 wires (wires no. 5, 6, 15 and 16) resulting in a 16 wire loading and then removing 8 more wires (wires no. 1, 2, 9, 10, 11, 12, 19 and 20) resulting in an 8 wire loading.

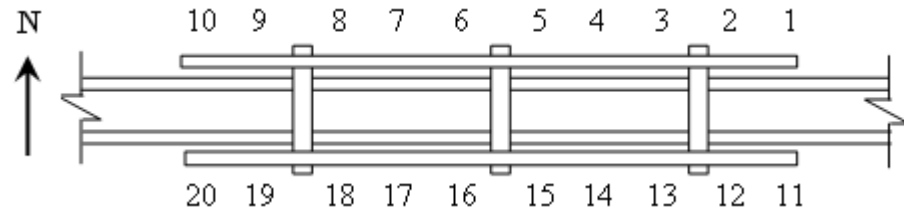


Figure 4.20: Plan view of the top support showing the numbering of the SMA wires.

The length measurements and the strain calculations for the loading phase are shown in Table 4.3. It should be noted that during unloading no measurements were taken since from checks that were made, there was insignificant change in the length of the loaded wires when either the number of loaded wires was increased or decreased. It can be observed from the table that wire no. 11 has a small strain. This is due to the fact that the thread of the pre-stressing device failed and no additional load could be applied. Although it was very difficult to reach the 2% strain in all the wires, an attempt was made to have the strains between 1% and 3%. As it can be seen from the table on the average the strain in the wires at each side of the pier was very close to 2%.

Table 4.3: Strains in the loaded wires.

Wire No	Initial Length (cm)	Final Length (cm)	Strain (%)	Wire No.	Initial Length (cm)	Final Length (cm)	Strain (%)
1	53.5	55.0	2.80	11	53.8	54.5	1.30
2	51.6	53.6	3.88	12	54.2	55.2	1.85
3	51.0	52.1	2.16	13	52.1	53.2	2.11
4	52.1	52.9	1.54	14	53.1	54.0	1.69
5	52.5	53.5	1.90	15	53.0	54.3	2.45
6	52.5	53.9	2.67	16	54.0	55.6	2.96
7	53.0	53.5	0.94	17	52.0	53.0	1.92
8	52.3	53.0	1.34	18	53.0	54.3	2.45
9	53.0	53.8	1.51	19	53.3	54.0	1.31
10	53.5	54.8	2.43	20	53.8	54.9	2.04
Average strain			2.12	Average Strain			2.01

4.5.2.2 System Identification

Based on the measurements and the May 2007 computed model, used to extract the dynamic characteristics of the monument and described in sub-section 4.4.2.2, a second identification test is performed in the aim to see the improvements in terms of natural frequencies and periods of the studied Aqueduct. Results obtained from signal analysis and the first five frequencies that were identified are shown in Figure 4.10. Note that signals were obtained from two triaxial accelerometers (EpiSensors) positioned at two different locations on the aqueduct indicated with numbers 1 and 2 as in Figure 4.9

It is important to recall that the eigenvalue analysis of the model resulted in the following periods of vibration: 1.37 s, 1.16 s, 0.98 s, 0.80 s and 0.68 s. The comparison of the measured and computed periods of vibration for the first five

modes is shown in Figure 4.12, showing that there is a very close agreement between the calculated and the measured periods of vibration.

Two EpiSensors were positioned now at 2 different locations on the aqueduct indicated with numbers 1 and 2 (see Figure 4.9), and a rubber impact hammer was used to induce vibrations in the aqueduct in addition to ambient vibrations. One impact location was used indicated in Figure 4.9 with the letter *A*. The *x*-axis, *y*-axis and *z*-axis of the EpiSensors were aligned with the longitudinal, perpendicular to its plane and vertical directions of the aqueduct, respectively.

The measurements were analyzed using the software DaisyLab 9.0. A Fast Fourier Transform (FFT) was used with a low pass Butterworth filter of 10 Hz, a high pass Butterworth filter of 0.6 Hz and a Hanning data window.

As explained before, five loading conditions were applied on the structure by pre-stressing 4 wires, 12 wires and 20 wires in a loading cycle, and then by removing the load in 4 wires, hence leaving 16 wires loaded, and finally removing 8 wires leaving 8 wires loaded. The results of the FFT analysis of the signal at position 1 are shown in Figures 4.21 to 4.25. It should be noted that the same results were obtained by the sensor which was placed at position 2.

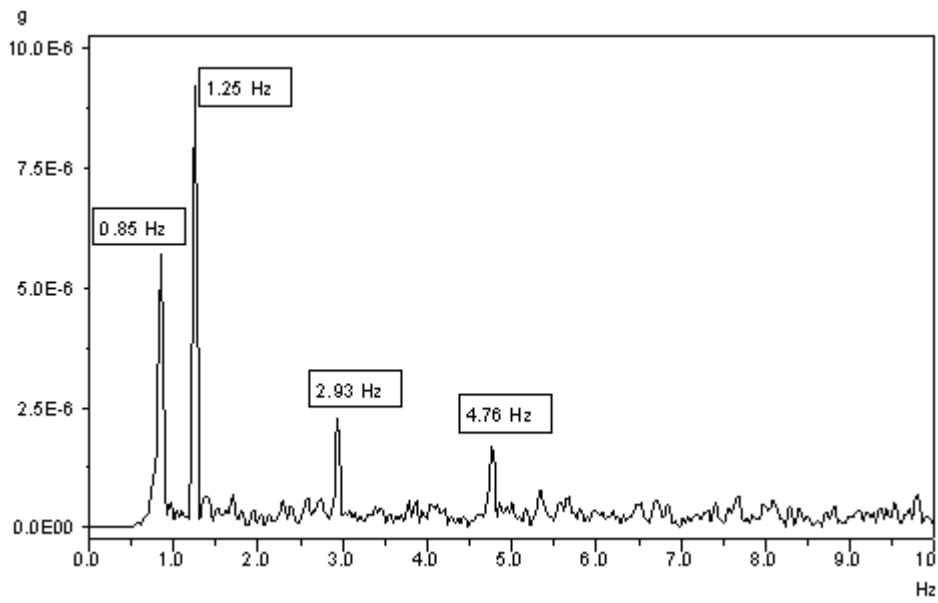


Figure 4.21: FFT for position 1 with 4 SMA wires loaded.

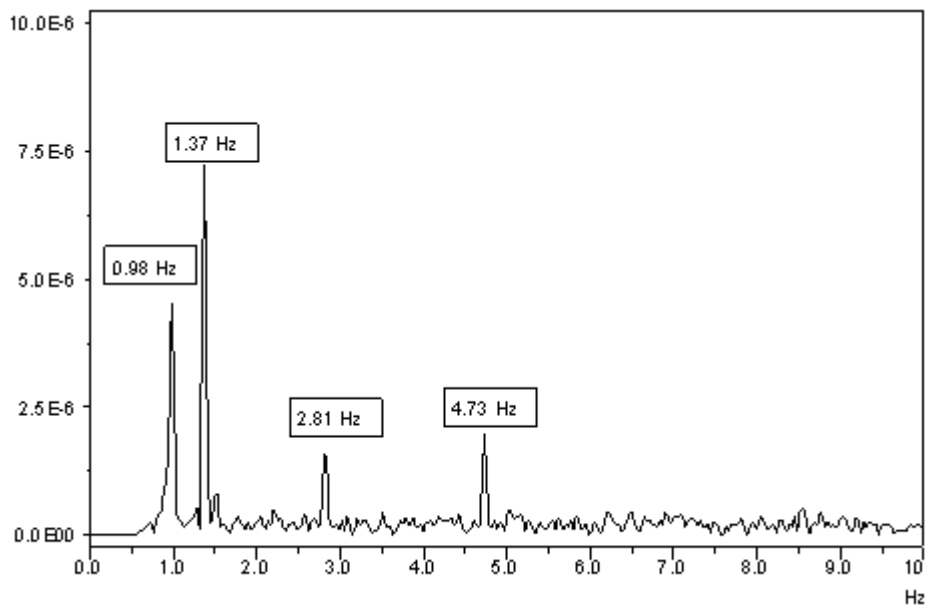


Figure 4.22: FFT for position 1 with 12 SMA wires loaded.

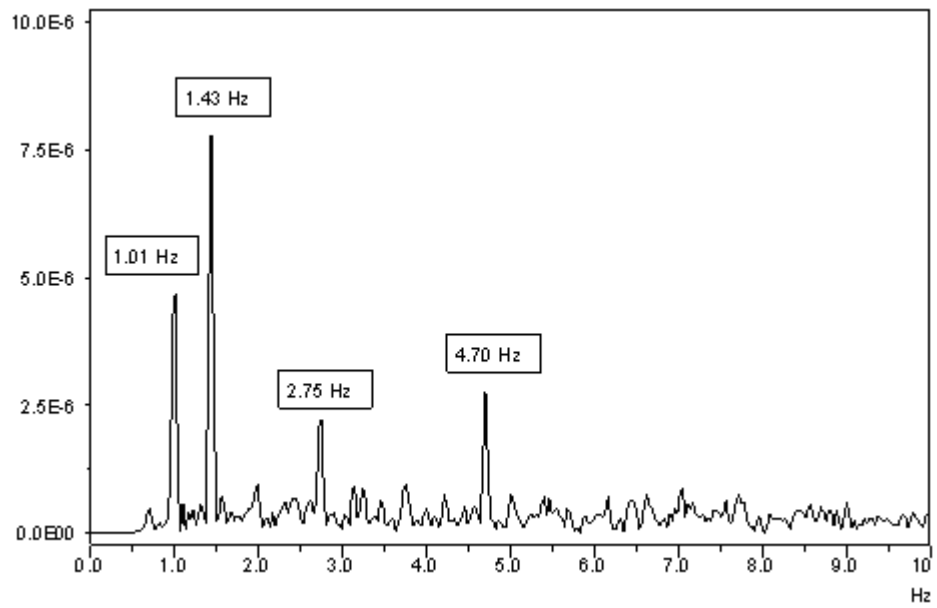


Figure 4.23: FFT for position 1 with 20 SMA wires loaded.

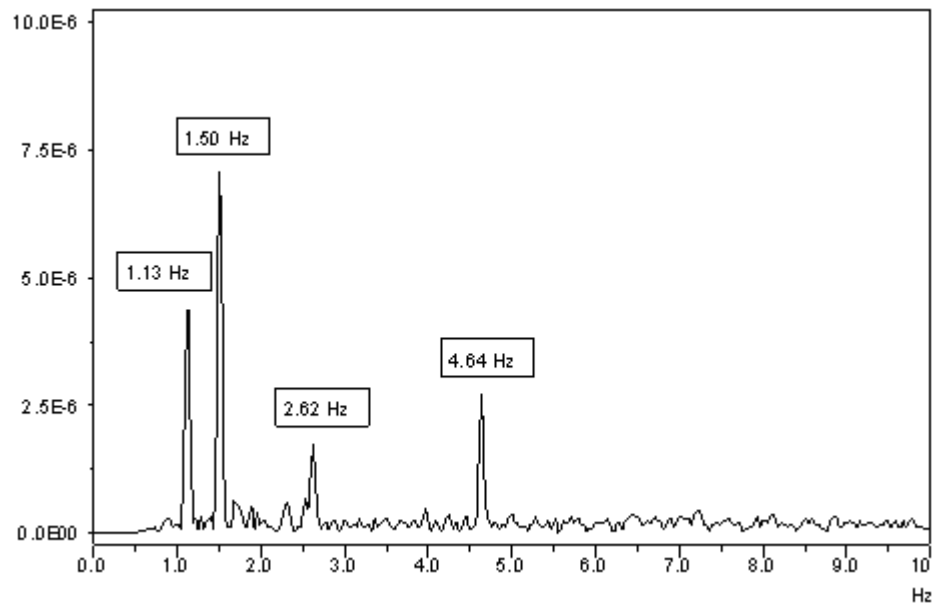


Figure 4.24: FFT for position 1 with 16 SMA wires loaded.

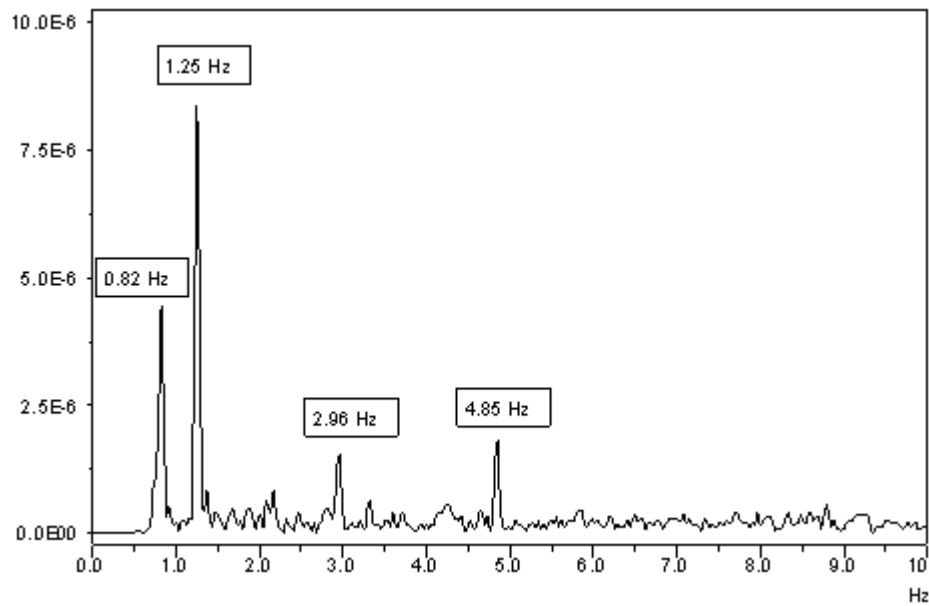


Figure 4.25: FFT for position 1 with 8 SMA wires loaded.

4.6 Discussion

In comparing Figures 4.21 to 4.25 with Figure 4.10 it is obvious that the application of the SMA wires have a significant effect on the dynamic behaviour of the aqueduct. While in the case that there are no wires on the structure the obtained signal is complex and only a few distinct frequencies appear, as soon as the SMA wires are applied, the signal in all the cases clears-up and four distinct frequencies appear. It is obvious that there may exist additional frequencies between these distinct frequencies and in particular between the second and the third and the third and the fourth ones, but since there is no means to establish them in a definite way, then no attempt is made to report any of those.

The results presented in Figures 4.21 to 4.25 are summarized in Table 4.4. It is obvious from the results that as the number of wires increases from 4 to 20, there is a shift of the fundamental frequency from 0.85 Hz to 1.01 Hz (period

shift from 1.18 s to 0.99 s). The same is observed for the second recorded frequency. This indicates a stiffening of the structure due to the application of a pre-stressing force. This stiffening can be explained by the increase in contact between the masonry units and hence the increase of its stiffness through the increase of the modulus of elasticity of the masonry matrix. For the third and the fourth frequencies though a slight decrease is recorded with the increase of the number of wires, from 2.93 Hz to 2.75 Hz and from 4.76 Hz to 4.70 Hz, respectively.

In the case of unloading, the same behaviour is exhibited by the structure. For the first two recorded frequencies, as the number of wires decreases from 16 to 8 there is a decrease in the measured frequency, which indicates softening of the structure due to the removal of a pre-stressing force and hence decrease of the effective modulus of elasticity of the masonry matrix. For the other two frequencies the reverse takes place; that is as the number of wires decreases the measured frequencies increase slightly.

Table 4.4: Measured frequencies for the various loading cases.

Loading Cycle	Loading			Unloading	
	No. of wires	4	12	20	16
Frequency 1 (Hz)	0.85	0.98	1.01	1.13	0.82
Frequency 2 (Hz)	1.25	1.37	1.43	1.50	1.25
Frequency 3 (Hz)	2.93	2.81	2.75	2.62	2.96
Frequency 4 (Hz)	4.76	4.73	4.70	4.64	4.85

A discrepancy appears to exist between the results for the 20 wires compared to those for the 16 wires. Although the pre-stressing force is decreased, the magnitude of the first two measured frequencies increases, while that of the other two decreases. An explanation for this can be the difference in the load pattern that was applied due to the difference in the sequence of pre-stressing the wires as explained under the section of experimental setup. By removing the four wires in the middle to go from the 20 to the 16 wires in the unloading cycle, a different load pattern was formed compared to the loading one, in

which the four middle wires were the first to load. Therefore, since there was a difference in the loading distribution then the loading and unloading cycles should be treated as distinct cases.

The results presented in Table 4.4 and discussed above are plotted in Figure 4.26. From this figure it is obvious that the increasing slope for frequencies 1 and 2 for the loading cycle is the same, while the decreasing slope for frequencies 3 and 4 is also the same. The exact same pattern is observed for the unloading cycle with a slight difference in the slopes of the lines.

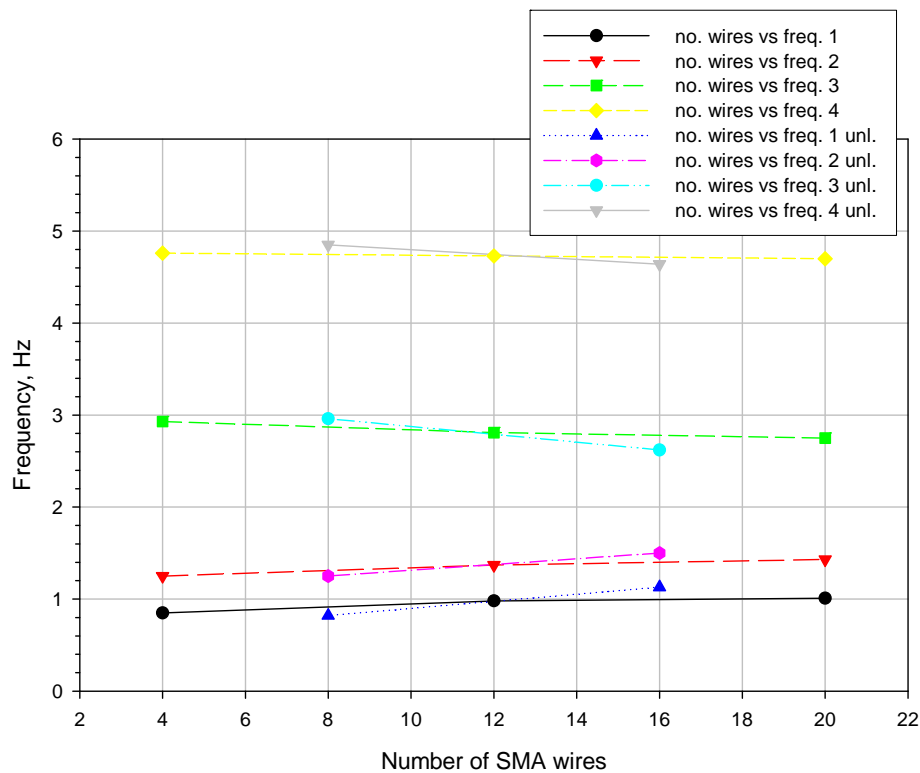


Figure 4.26: Variation of the measured frequencies with the number of SMA wires for the loading and unloading (unl.) cycles.

Since the strain in the wires is not the same (Table 4.2), then the loading in the wires is also different. This means that plotting the variation of frequencies as a function of the number of wires may not give meaningful results. Using the data in Table 4.2 and the stress-strain relationship of the tested alloy, the load in each of the 3.5mm diameter wires were calculated as shown in Table 4.5. Then the total load for each of the loading cases was calculated by adding the loads in the participating wires. The results of this calculation are shown in Table 4.6 and the plots of the frequencies versus the load in the SMA wires are shown in Figure 4.27.

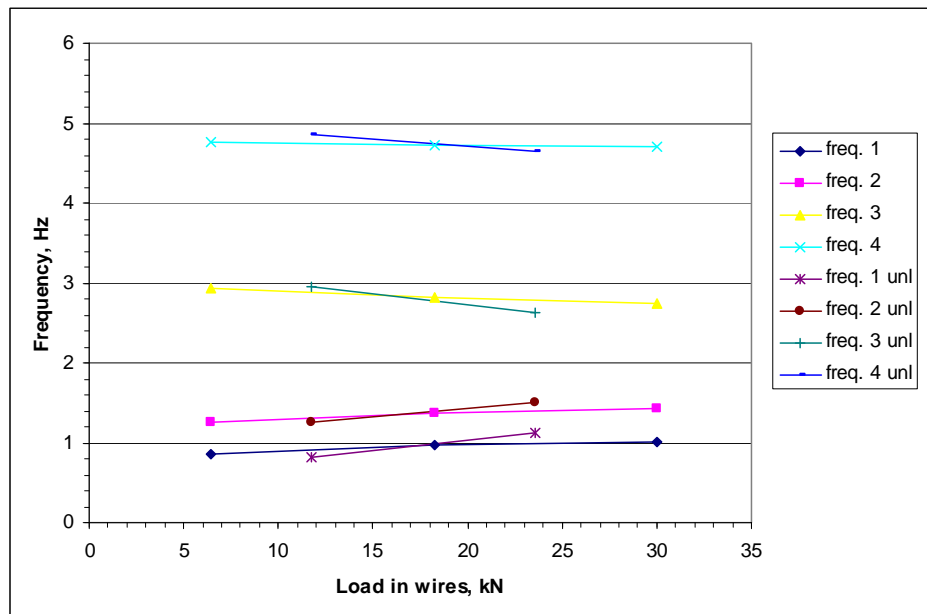


Figure 4.27: Variation of the measured frequencies with the load in clusters of SMA wires for the loading (4, 12, 20 wires) and unloading (16, 8 wires) cycles.

In comparing Figures 4.26 and 4.27 it can be observed that they give the same trends, although there may be some difference in the slopes of the curves. Therefore it can be stated that provided that there is not a large variation in the

strains in the loaded wires, the plots of frequency versus wire number and frequency versus load, give similar results.

Table 4.5: Load in the wires.

Wire No.	Strain	Stress (N/mm ²)	load (kN)	Loading case 1 (kN)	Loading case 2 (kN)	Loading case 3 (kN)	Loading case 4 (kN)	Loading case 5 (kN)
1	2.80	173.5	1.669		1.669	1.669	1.669	
2	3.88	195.9	1.885		1.885	1.885	1.885	
3	2.16	160.7	1.546			1.546	1.546	1.546
4	1.54	147.8	1.422			1.422	1.422	1.422
5	1.90	155.4	1.495	1.495	1.495	1.495		
6	2.67	170.9	1.644	1.644	1.644	1.644		
7	0.94	133.5	1.284			1.284	1.284	1.284
8	1.34	143.2	1.378			1.378	1.378	1.378
9	1.51	147.1	1.415		1.415	1.415	1.415	
10	2.43	116.2	1.118		1.118	1.118	1.118	
11	1.30	142.2	1.368		1.368	1.368	1.368	
12	1.85	154.3	1.485		1.485	1.485	1.485	
13	2.11	159.7	1.536			1.536	1.536	1.536
14	1.69	151.0	1.453			1.453	1.453	1.453
15	2.45	166.6	1.603	1.603	1.603	1.603		
16	2.96	176.6	1.699	1.699	1.699	1.699		
17	1.92	155.6	1.497			1.497	1.497	1.497
18	2.45	166.6	1.603			1.603	1.603	1.603
19	1.31	142.5	1.371		1.371	1.371	1.371	
20	2.04	158.3	1.523		1.523	1.523	1.523	
			Total Load	6.441	18.275	29.995	23.553	11.719

Using now the results shown in Figure 4.27 for the loading cycle, second order polynomials were fitted to the results as shown in Figure 4.28. From the

equation for the fundamental frequency, it can be predicted that the fundamental frequency of the structure when no wires are applied is 0.737 Hz. This is shown in Figure 4.29, in which the fitted line was used to extrapolate backwards to zero load at which the intercept is 0.74 Hz. In comparing with the measured fundamental frequency of the structure (Figure 4.10), it is obvious that there is a close match and therefore this equation can be used for the prediction of the modification of the fundamental frequency of the structure as a function of the applied load in the SMA wires.

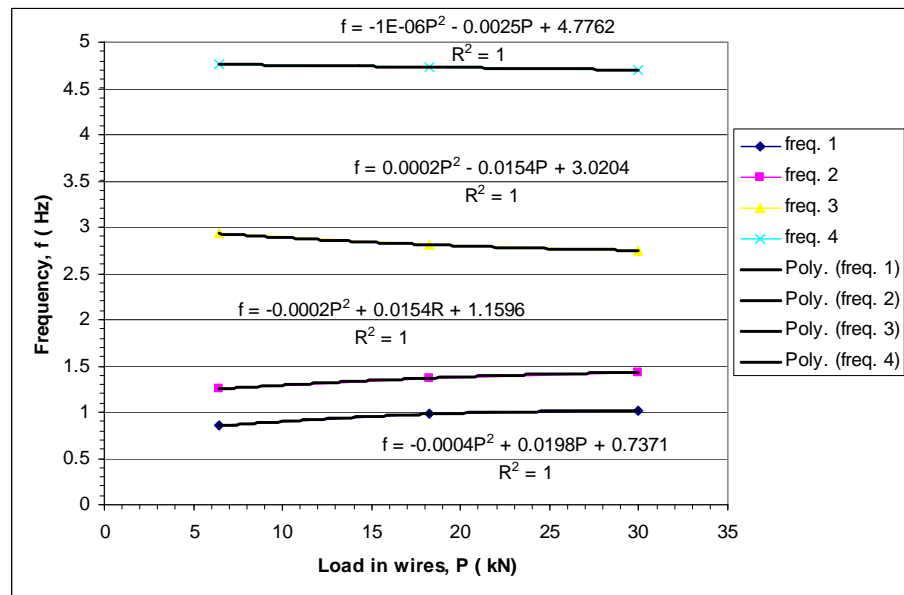
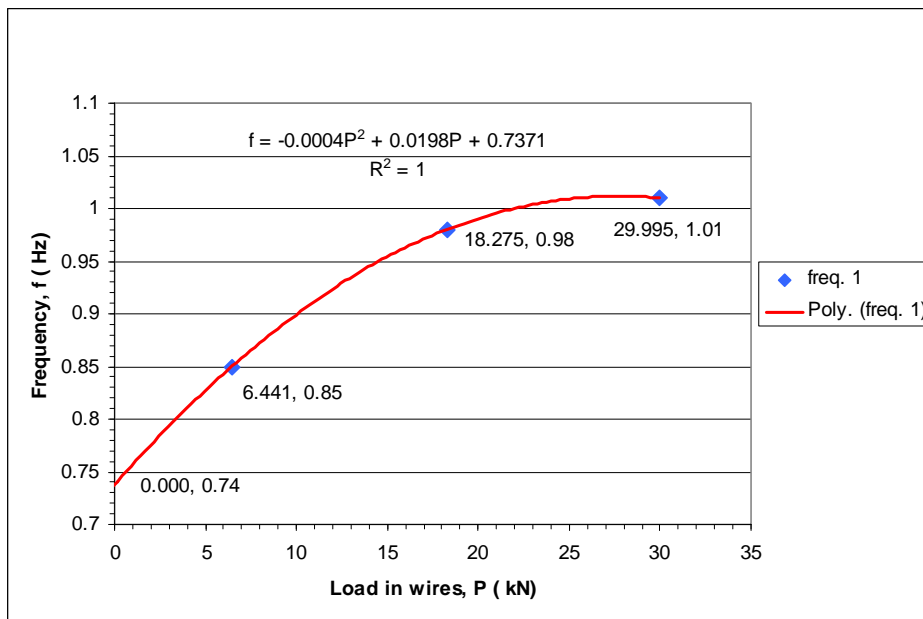


Figure 4.28: Fitted curves of the variation of the measured frequencies with the load in clusters of SMA wires for the loading (4, 12, 20 wires) cycle.

Table 4.6: Load in the wires and corresponding frequencies.

Loading Cycle	Loading			Unloading	
	No. of wires	4	12	20	16
Load in wire cluster (kN)	6.441	18.275	29.995	23.553	11.719
Frequency 1 (Hz)	0.85	0.98	1.01	1.13	0.82
Frequency 2 (Hz)	1.25	1.37	1.43	1.50	1.25
Frequency 3 (Hz)	2.93	2.81	2.75	2.62	2.96
Frequency 4 (Hz)	4.76	4.73	4.70	4.64	4.85

**Figure 4.29:** Extrapolation of the fitted curve of the 1st frequency to zero-load for the loading (4, 12, 20 wires) cycle.

4.7 Conclusion

In this chapter the methodology used to obtain the periods of vibration of the aqueduct of Larnaca was presented along with the computational models for the

monument. Considerable differences were noted between the measurements of 2004 and those of 2007, which are attributed to the modification of the soil conditions due to the level of the water in the nearby salt lake. It is therefore important, before performing the system identification and planning the retrofitting of a monument, to consider all possible parameters that may affect its behaviour, including seasonal effects. This seasonal change in the behaviour should lead to the design of adaptive retrofitting schemes that will be able to accommodate the considerable change in the dynamic characteristics of the structure. In both cases the measured frequencies of vibration are very closely matched by the ones obtained from the eigenvalue analysis of the computational models.

This model is used to form the basis for the analytical studies of the effects of shape memory alloy (SMA) pre-stressed devices on the behaviour of the monument.

Then, the results of the application of copper-based shape-memory-alloy pre-stressing devices on an ancient aqueduct are presented and the dynamic characteristics of the monument without the application of SMA are reported.

From the measurements it is clear that the SMAs have a significant effect on the dynamic characteristics of the monument. It was observed that the application of the wires had as a result the significant modification of the recorded signal. While for the case of no wires the signal was rather complicated, the application of the wires had as an effect the cleaning of the signal and the recording of 4 predominant frequencies, irrespective of the number of wires applied.

References

1. Abed M., Bouarfa H. and Boulaghmen F. (2005). "Assistance a L'évaluation Post-Séismique des Constructions par Raisonnement Basé sur des Cas", *Proceedings du Congres International Réhabilitation des Constructions et Développement Durable*, May 3-4, Algiers, Algeria, vol. 2, 272-277. (In French).
2. Aghakouchak A.A., Kiamehr H. and Ghafouripour A. (2000). "An Overview of System Identification Methods and Applications Part I: Methods of System Identification and Dynamic Tests", *Proceedings of the 4th International Conference on Coasts, Ports & Marine Structure*, Shahid Rajaei Port Complex, Bandar Abbas, Iran.
3. Ambient Vibration Response (Output-only) based System Identification. Available from URL <http://www.cse.polyu.edu.hk/~dynamics/si.htm>
4. Andersen P. (1997). "Identification of Civil Engineering Structures using Vector ARMA Models", *Ph.D. Dissertation*, Department of Building Technology and Structural Engineering, Aalborg University, Denmark.
5. Beck J. and Dionisio B. (2001). "A Benchmark Problem for Structural Health Monitoring", *Earthquake experimental Techniques*, vol. 25, no. 3, 49-53.
6. Biritognolo M., Bonci A. and Viskovic A. (2000). "Numerical models of masonry façade walls with and without SMADs", *Proceeding of Final Workshop of ISTECH Project - Shape Memory Alloy Devices for Seismic Protection of Cultural Heritage Structures*, 117-140, Joint Research Centre, Ispra, Italy.
7. Caicedo J.M. (2001). "Two Structural Health Monitoring Strategies Based on Global Acceleration Response: Development, Implementation, and Verification", *Master Thesis*, Department of Civil Engineering. Washington University, St. Louis. Missouri, U.S.A.

8. Casciati F. and Faravelli L. (2004). "Experimental characterisation of a Cu-based shape memory alloy toward its exploitation in passive control devices", *Journal de Physique IV*, vol. 115, 299-306.
9. Chrysostomou C.Z., Demetriou T. and Pittas M. (2003). "Conservation of historical Mediterranean sites by innovative seismic-protection techniques", *Proceedings 3rd World Conference on Structural Control*, Como, Italy, vol. 2, 947-954.
10. Chrysostomou C.Z., Demetriou T., Pittas M. and Stassis A. (2005). "Retrofit of a church with linear viscous dampers", *J. Struct. Cont. Health Monit*, vol. 12, no. 2, 197-212.
11. Chrysostomou C.Z., Demetriou T., Stassis A. and Hamdaoui K. (2008a). "Seismic Protection of an Ancient Aqueduct Using SMA Devices", *Proceedings of the 2008 Seismic Engineering International Conference "MERCEA '08"*, Reggio Calabria, Italy.
12. Chrysostomou C.Z., Stassis A., Demetriou T. and Hamdaoui K. (2008b). "Application of Shape Memory Alloy Prestressing Devices on an Ancient Aqueduct", *J. Smart Structures and Systems*, vol. 4, no. 2, 261-278.
13. Chrysostomou C.Z., Demetriou T. and Stassis A. (2004). "Seismic protection of an aqueduct by innovative techniques", *Proceedings 3rd European Conference on Structural Control*, Vienna, Austria.
14. Croci G. (2000). "General methodology for the structural restoration of historic buildings: the cases of the tower of pisa and the basilica of assisi", *J. Cultural Heritage*, vol. 1, 7-18.
15. Doebling S.W., Farrar C.R., Prime M.B. and Schevitz D.W. (1996). "Damage Identification and Health Monitoring of Structural and Mechanical Systems from Changes in their Vibration Characteristics: A Literature Review", *Los Alamos Report*, LA-13070-MS.

16. Dyke S.J., Caicedo J.M. and Johnson E.A. (2000). "Monitoring of a Benchmark Structure for Damage Identification", *Proceeding of the Engineering Mech. Specialty Conf.*, May 21–24, Austin, Texas, USA.
17. El-Borgi S., Choura S., Ventura C., Baccouch M. and Cherif F. (2005). "Modal identification and model updating of a reinforced concrete bridge", *Smart Structures and Systems*, vol. 1, no. 1, 83-101.
18. Faravelli L. (2002). "Experimental Approach to the Dynamic Behaviour of SMA in Their Martensitic Phase", in F. Casciati (ed.), *Proceedings of the 3rd word conference on structural control*, John Wiley & Sons, Chichester: UK, vol. 2, 163-168.
19. Faravelli L. and Casciati S. (2003). "Dynamic behavior of a shape memory alloy structural devices: numerical and experimental investigation", K. Watanabe and F. Ziegler (eds.), *Dynamics of Advanced Materials and Smart Structures, IUTAM series*, Kluwer Academic Publishers, Dordrecht, Netherlands, 63-72.
20. Fritzen C.P. (2005). "Recent Developments in Vibration-Based Structural Health Monitoring", *Proceedings of the 5th International Workshop on Structural Health Monitoring*, Sep 12-14, Stanford University, Stanford: C A, 42-60.
21. Hamdaoui K. (2006). "Historical Monument Health Monitoring Based On Ambient Vibrations", *Master Thesis*, Department of Civil Engineering, Jordan University of Science and Technology, Irbid, Jordan.
22. Kullaa J. (2003). "On line Structural Health Monitoring", *Proceedings of the 3rd Word Conference on Structural Control*, Como, Italy, vol. 3, 133-138.
23. Magpantay H.A. "Modal Identification from Ambient Vibration Measurement: a Technology for Optimization of the Performance of Civil Engineering Structure". [Online], Available from URL <http://www.adnu.edu.ph/Research/gibon4v1n1.asp> --

24. Rytter A. (1993). "Vibration Based Inspection of Civil Engineering Structures", *Ph.D. Dissertation*, Department of Building Technology and Structural Engineering, Aalborg University, Denmark.
25. Syrmakziz K. and Sophocleous A. (2002). "Passive Control Techniques for the Seismic Protection of Historical and Monumental Masonry Structures", *Proceeding of the 3rd World Conference on Structural Control*, Come, Italy, vol. 2, 955-960.
26. Wenzel H. "Structural Assessment of the Cultural Heritage", Available online from URL <http://www.brimos.com/pdf/cultural.pdf>
27. Wenzel H. and Pichler D. (2005). *Ambient Vibration Monitoring*, England. John Wiley and Sons.
28. Zonta D. (2000). "Structural Damage Detection and Localization by Using Vibrational Measurements", *Ph.D. Dissertation*, University of Bologna. Bologna, Italy.

Chapter 5

SMA Bars as Base Isolation Device

5.1. Introduction

In the highly seismic areas of several countries as Japan, USA, Italy and India, hundreds of our civil engineering structures are protected nowadays by the so called base isolators. Most of the constructions that have been built using this concept (either completed or still under construction) use large rubber isolation bearings, even though there are other sorts based on sliding of one part of the building relative to the other. These buildings are not rigidly fixed to their foundations and the key feature of the base isolations is the fact that they add flexibility to the structure. They are also manufactured to absorb energy and consequently add damping to the system so that the structure that is decoupled from the ground gets a much lower fundamental frequency than the ones predominant in the excitation. The building moves, then, and deflects without absorbing any kind of lateral motion energy!

The quite simple idea behind the concept of base isolation is explained through the example of Figure 5.1. The edifice (Figure 5.1a) that rests on frictionless rollers does not move during the earthquake ground motion since the rollers freely roll. Consequently, no transmission of forces (due to the ground vibration) to the system will happen and the building does not experience the earthquake. Attention may be made, in this case, to the dimension of the gap between the structure and the vertical wall of the foundation to avoid a hit between the edge of the building and the pit during the ground motion.

If the building is rested on flexible padding offering resistance against horizontal movements as shown in Figure 5.1b, only a reduced effect of the shaking forces induced by earthquake motion will be transferred to the built structure, say up to 5 times smaller in large earthquakes and 3 times less in a small one, than those in regular building resting directly on ground (Figure 5.1c). The small seen movement of the building (Figure 5.1b) is then accompanied with large movement in the isolators. A laboratory test drawn when using rubber pads is shown in Figure 5.2. Flexible pads are called here base isolators, where the base isolated building is the structures to be protected by means of base isolators.

Note that base isolations are not suitable for all type of buildings: high-rise buildings or those built on soft soil are not suitable for this kind of technology, conversely, the most suitable candidates are the low or medium-rise buildings rested on hard soil, and, of course, the deck of bridges.

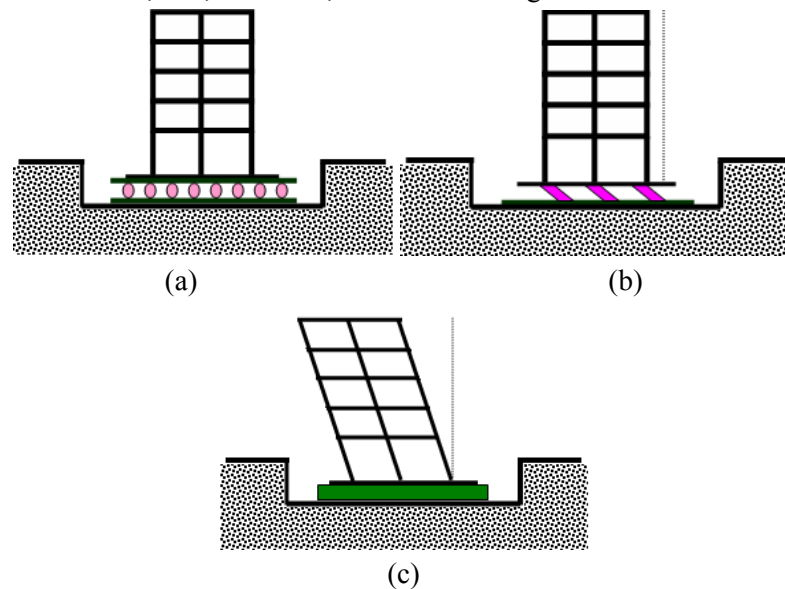


Figure 5.1: (a) Building rollers without any friction: no motion of the building will be seen. (b) Building on flexible padding: less shaking of the building will be seen. (c) Building resting directly on ground: violent shaking will be seen.

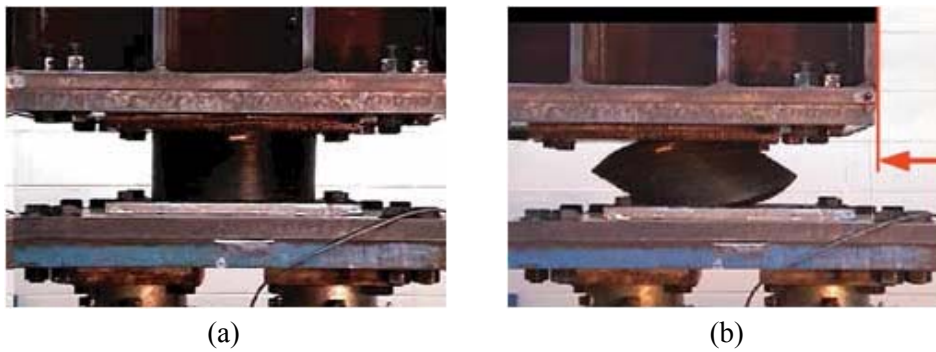


Figure 5.2: Base isolators in laboratory tests: (a) Un-deformed isolator. (b) Deformed isolator.

The relatively recent base isolation technology is applied in numerous real buildings over the world since the 80s.

The base isolation solutions are discussed in detail in [Soong-Dargush, 1997]. This book makes evident how a dissipative component is also welcome.

In this chapter, a new concept of base isolator realized by metallic bars instead of the commonly used rubber-steel layers was presented at the first time in [Casciati et al., 2006]. The papers [Casciati et al., 2007a], [Casciati et al., 2007b], [Casciati et al., 2007c] and [Casciati et al., 2007d] collect the preparatory design studies of the new proposed passive device, presented in this chapter. First found results have been published recently in [Casciati et al., 2007e] and [Casciati and Hamdaoui, 2008]. More sophisticated solution can be reached in a semi-active framework as in the book [Casciati et al., 2006].

In the concept of the isolator system presented here, the inverse pendulum that explains the physical model consists of a number of bars that are made in a Cu-base shape memory alloy (SMA) and assembled in a special geometry. The energy dissipation is guaranteed here by the SMA hysteresis within the super-elastic constitutive law characterizing the selected alloys. The claimed self-healing aspect is its recovering capability [Tahirji et al., 2004].

5.2 Base isolation of works of art and monuments

Base isolation technology can be also very useful for the retrofitting of important building and historical monuments [Takayoshi and Takafumi, 2008]. In Japan, after the Hanshin-Awaji earthquake, demand for seismic isolation for works of art and monuments in existing museums has greatly increased. In some museums, the seismic isolation has been applied to the entire building not only to protect the exhibits but also to retrofit the building structures. Conversely, and in many other museums, the seismic isolation has been applied only to the individual showcases containing the valuable exhibits. Many types of isolation devices developed and used for the applications, some examples of which are described in the following.

Figure 5.3 shows the National Museum of Western Art in Tokyo, that is the first retrofitted museum by base isolation (1998). For “the Gate of Hell” (Figure 5.4a) created by Auguste Rodin and located in the garden of the museum, seismic isolation system, as seen in Figure 5.4b, has been used since 1999. The Gate of Hell has an outer size of 5.4 x 3.9 x 1.0 m and a weight of 7.0 t. The seismic isolation system used for this bronze monument consists of 5 isolation devices using roller bearings and 2 viscous dampers. The isolation device comprises 2 stages of the roller bearings and circular rails which provides a linear restoring force. In the seismic isolation of the Gate of Hell, the natural period of 4 s is achieved by using the isolation devices.

Restoration and reconstruction of the cultural heritages are the national undertakings. Reconstruction of the Daigokuden (Figure 5.5) which located on the “Heijokyo”, old capital of Japan at Nara, has been started from 2001. original structure was not strong enough against earthquakes, so the base isolation was applied. Rubber bearings, linear and viscous dampers were used for the isolation devices (Figure 5.6)

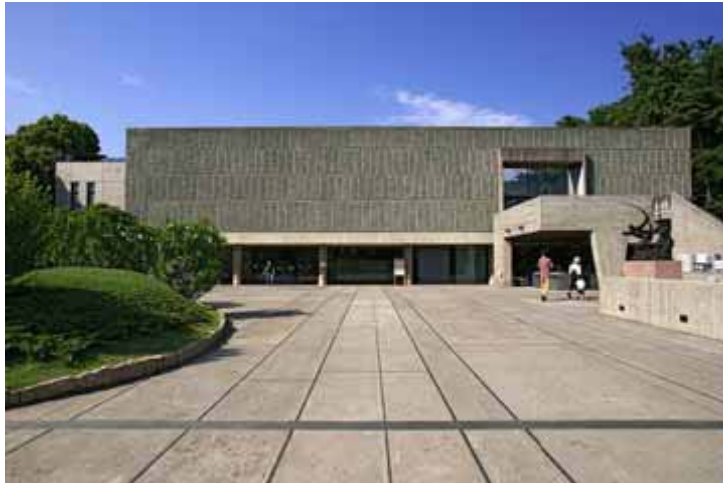
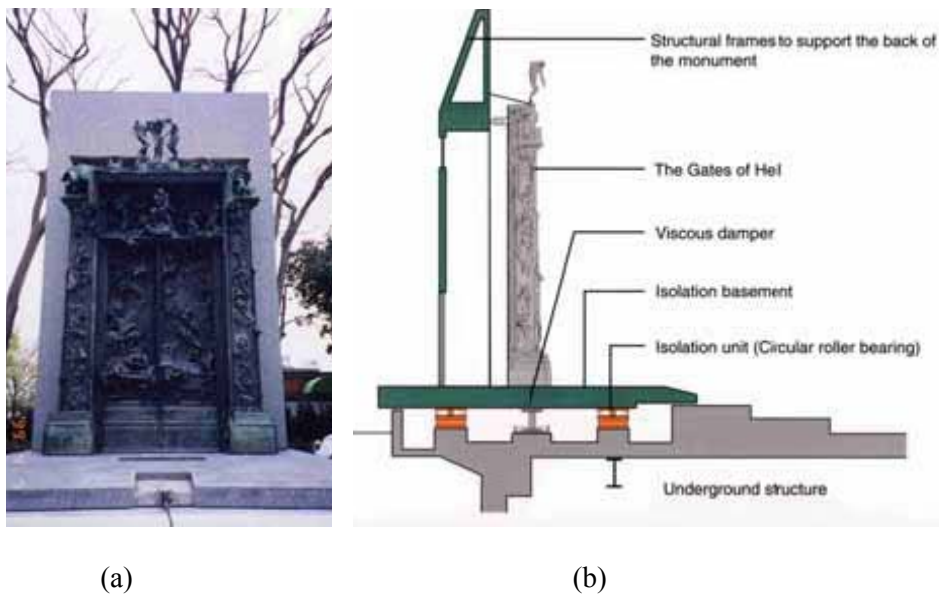


Figure 5.3: The national museum of Western art, Tokyo.



(a)

(b)

Figure 5.4: (a) The gate of hell, (b) Seismic isolation of the gate of hell.

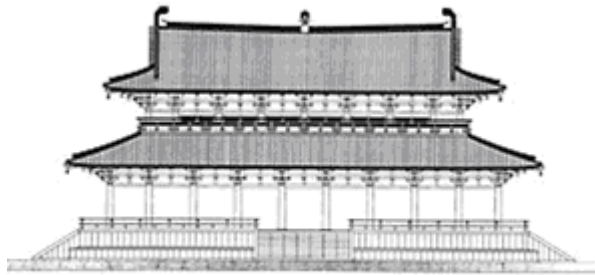


Figure 5.5: Daigokuden (Main structure).

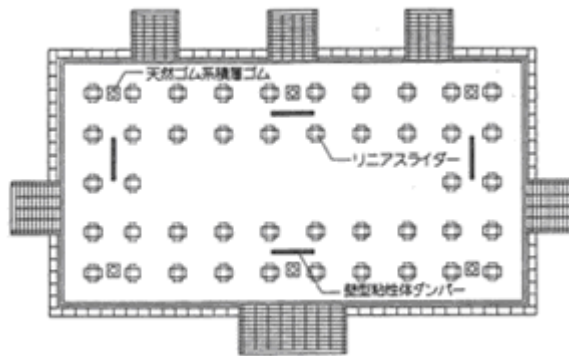


Figure 5.6: Isolation plan.

5.3 The proposed device

The idea behind the selection of the device shown below as base isolator is the sculpture of the Spanish artist Eusebio Sempere (1923-1985). It was realized in 1971 and it is still exposed in a museum in Barcelona, Spain. The Figure 5.7 evinces the details of the device to be studied as a base isolator system made by shape memory alloys bars.



Figure 5.7: Photo of the sculpture proposed as passive device.

The system shown in the Figure 5.7 above is designed to support a steel plate serving as superimposed tray, where the system to be isolated is mounted. Bars are displayed in a manner to contrast their falling under any vertically applied load on the superimposed tray. In the proposed device, the number, diameter, inclination and the geometric disposition of the Cu-base SMA bars represent the design variables of the system.

Consequently, the geometry realizes, rather than an inverse pendulum, a cantilever with good axial strength and with bending properties assigned to the elastic-plastic behaviour of the bars' material (stainless steel, for instance). But remind that in this case, hysteretic cycles would require excursions in the plasticity area, and the associated displacements would have an irreversible nature.

Conversely, when using the super-elastic SMA as bars' material instead of the elastic-plastic one, [Auricchio et al., 2001] [Casciati and Faravelli, 2004], the dissipation is ensured by the super-elastic hysteresis and, when the load is removed, the relative displacement disappears, allowing the re-centring of the system.

5.4 ANSYS finite element code as workbench environment for SMA implementation

The finite element method that is originated from the needs for solving complex structural analysis problems in civil and aeronautical engineering is usually used for the verification and validation of product designs through the use of structural analysis simulation models. Its development is traced back by the civil engineer Alexander Hrennikoff and the mathematician Richard Courant in the early of 1940s [Wikipedia encyclopaedia, 2008].

The method has been generalized later in the 1970s into a branch of applied mathematics for numerical modelling of physical systems in a wide variety of engineering disciplines, e.g., electromagnetism and fluid dynamics. The development of the finite element method in structural mechanics is often based on the energy principle, e.g., the virtual work principle or the minimum total potential energy principle, which provides a general, intuitive and physical basis that has a great appeal to structural engineers.

Developing a parametric model of the selected device is the key to allow a quick performing and the efficacy for design iterations, since the entire analysis process can be automated. In the ANSYS software [ANSYS, 2003], two options are routinely used to perform these automated analyses [Barrett and Cunningham, 2004]:

- 1. ANSYS Parametric Design Language (APDL):** scripts used to automate common tasks or even develop the model by generating key-point, line, area, and volume geometry in ANSYS. The APDL commands are the true

scripting commands that encompass a wide range of other features such as repeating a command, meshing, analysis and post-processing, macros, if-then-else branching, do-loops, vector and matrix operations. The downside to this method is that the development of the APDL geometry script can be very time consuming. Also the lack of robustness of re-generation using ANSYS Boolean operations can sometimes lead to geometry failures.

2. **GUI mode:** the model is built using features based on the CAD package or the ANSYS DesignModeler tool. The analysis is performed by importing the parametric geometry model into the ANSYS Workbench Simulation Tool. Using the Workbench DesignXplorer tools, the sensitivity of the design to changes in the geometry is determine, materials or loading conditions also.

For the base isolator studied here, only the APDL scripting technique is used. This analysis illustrates the use of the super-elastic law of this kind of smart material already implemented in ANSYS code [ANSYS, 2003] to simulate their structural response. The available routine (in ANSYS code) for shape memory alloys depends on the definition of six parameters that describe the stress-strain behaviour in both loading and unloading for the uniaxial stress-state. They are (Figure 5.8):

- SIG-SAS or σ_S^{AS} (C1): Starting stress value for the forward phase transformation;
- SIG-FAS or σ_F^{AS} (C2): Final stress value for the forward phase transformation;
- SIG-SSA or σ_S^{SA} (C3): Starting stress value for the reverse phase transformation;
- SIG-FSA or σ_F^{SA} (C4): Final stress value for the reverse phase transformation;
- EPSILON or ε_L (C5): Maximum residual strain;

- ALPHA or α (C6): Parameter accounting for material responses in tension and compression.

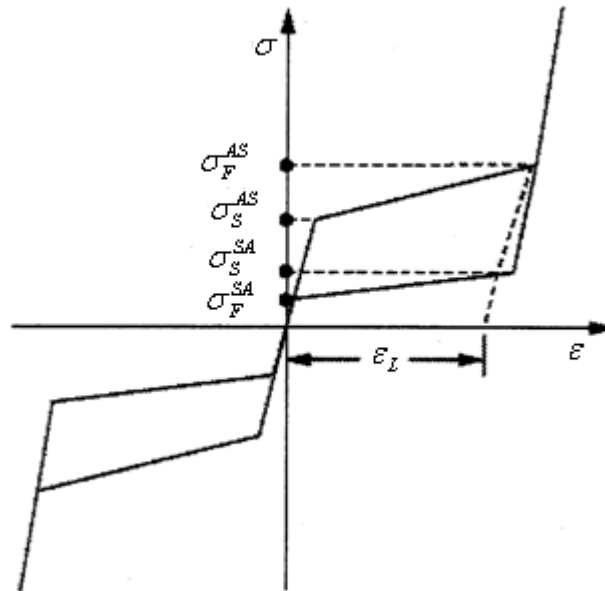


Figure 5.8: Idealization of a typical super-elastic behaviour of SMA.

5.5 The material model

It is worth noting that the behaviour in tension and compression is not accurately described by a simple parameter as α does. This makes the entire model prone to criticism. Nevertheless, in this feasibility study such an inaccuracy is consciously tolerated. For the adopted Cu-based alloy [Casciati and Faravelli, 2004], the following set of data is adopted for ambient temperature:

- $E = 60000$ MPa (Linear elastic modulus of elasticity of the SMA in the austenite phase);
- $\nu = 0.3$ (Poisson's ratio);
- $C1 = 140$ MPa;

- $C2 = 270 \text{ MPa}$;
- $C3 = 200 \text{ MPa}$;
- $C4 = 70 \text{ MPa}$;
- $C5 = 0.03$;
- $C6 = 0.27$;
- $C7 = 20000 \text{ MPa}$ (Modulus of elasticity of the SMA in the martensite phase).

The specific constitutive law implemented with the chosen code can only be specified for plane and solid elements (PLANE182, PLANE183, SOLID185, SOLID186, SOLID187, and SOLSH190). Therefore, the 3-D 8-node structural solid element SOLID185 (Figure 5.9) was adopted [ANSYS, 2003]. In particular, the proposed device is supposed made by the available bars in the laboratory of the department of structural mechanics in the University of Pavia: their diameter is either 3.5 mm or 5.3 mm

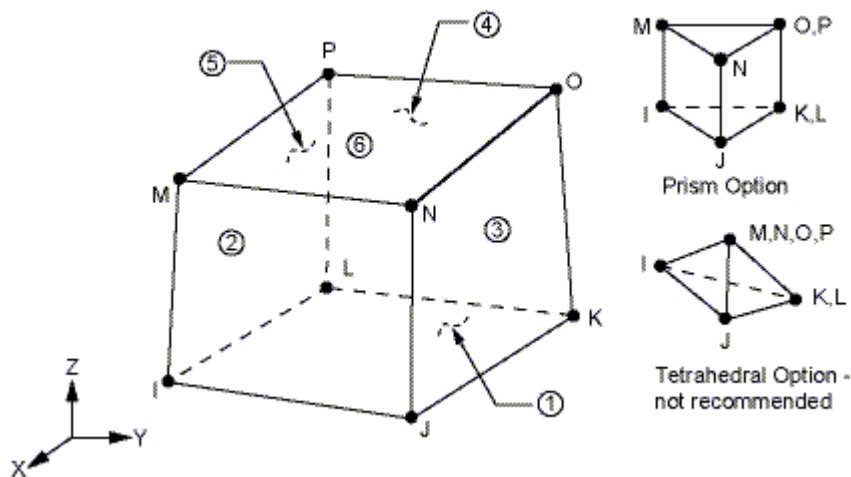


Figure 5.9: The adopted SOLID185 element geometry's.

5.6 The device's numerical model: Single bar

First, and to better understand the behaviour of the SMA bars when loaded by axial and/or lateral forces, a single bar, as seen in Figure 5.10, was fixed at the bottom and loaded first by a vertical action. The stress-strain diagrams produced by the ANSYS code resulted meaningless, since always a linear variation is seen without any trace of hysteresis. The actual stress-strain diagrams were therefore built by associating to the resulting stress an average strain: each strain is computed as the ratio of the difference of the displacements in two nodes (at different levels) divided by the distance between them (found as true strain in some bibliographies).

Consider the SMA single bar, 5.3 mm of diameter and 11 mm of length, (always Figure 5.10) and apply, first, a tension load by increasing the vertical force from 0 to 8.05 kN then down to 0. The resulted stress-strain graph is plotted in the Figure 5.11 below. It illustrates the hysteretic response captured by the shape memory alloy numerical model and clearly shows the meaning of the nine parameters adopted for ambient temperature as presented in section 5.4 above.

Again, on the same single bar, a compression load is now increased from 0 to 6.21 kN (engendering a deformation of 0.5%) and set down to 0. A tension load is then applied and increased from 0 to 8.05 kN (driving beyond 3% of deformation) and finally removed. This test was experimentally done and reported in [Casciati et al., 2005]. The results from the analytical and the experimental tests are proved to be in good agreement (see Figures 5.12 for the numerical test and 5.13 for the experimental one).

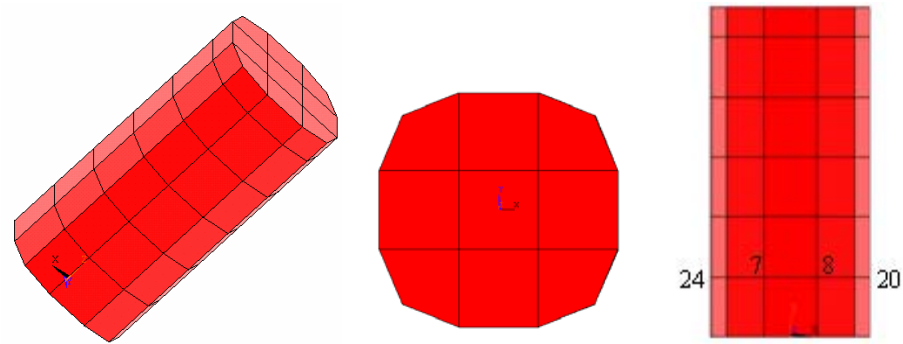


Figure 5.10: Discretization of each bar: section and lateral view.

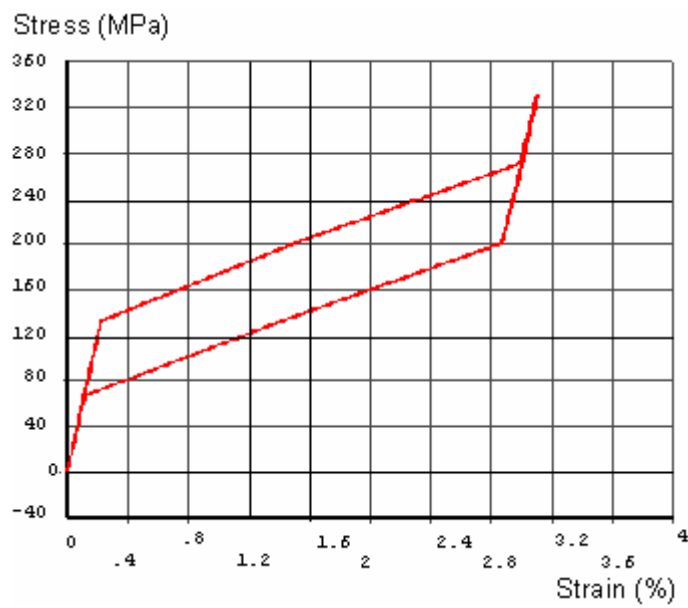


Figure 5.11: Stress- strain (average) obtained in the 5.3 mm bar of Figure 5.10 for a cycle of vertical tension loading-unloading.

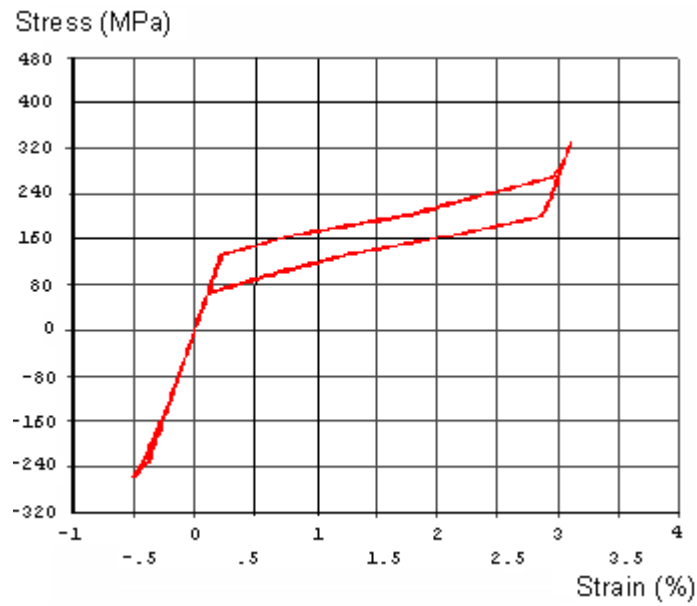


Figure 5.12: Stress- strain (average) obtained in the bar of Figure 5.10 for a cycle of vertical compression then tension loading-unloading.

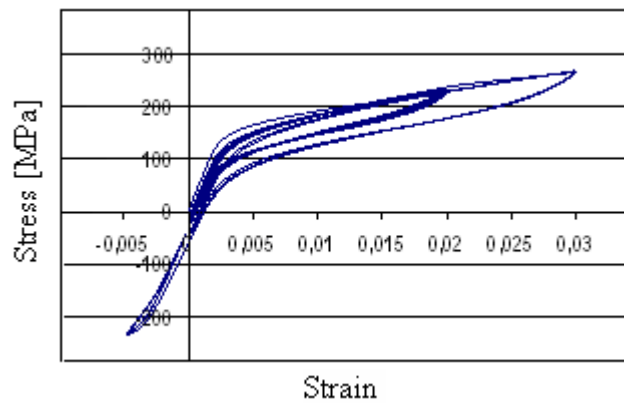


Figure 5.13: Stress- strain (average) obtained in the bar of experimentally as reported in [Casciati et al., 2005] for vertical compression then tension loading-unloading.

The next preliminary test was conducted by increasing first the vertical tension load up to a maximum value of 2415 N, which produces a stress in the elastic range of 100 MPa, and then adding a horizontal load (480 N) doubling the stress. The unloading is done by releasing first the horizontal force and then the vertical one to close the cycle.

Figures 5.14 a and b provide the corresponding stress-strain diagram, computed as for Figure 5.11, in the bottom layer of the bar but in two different nodes: 7 and 24, respectively. Node 7 is the bottom-left node of the central square in the bar section discretization shown previously in Figure 5.10; node 24 has the same ordinate of node 7, but belongs to the external left boundary.

Figure 5.15 collects the four diagrams “strain vs. bending moment” in the four nodes 24, 7, 8 and 20, nodes 8 and 20 being the symmetric (around the y axis) of nodes 7 and 24, respectively.

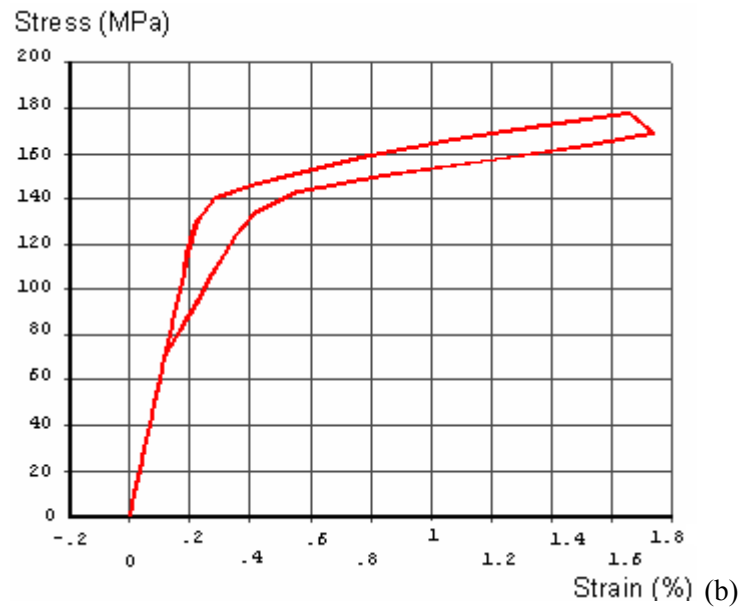
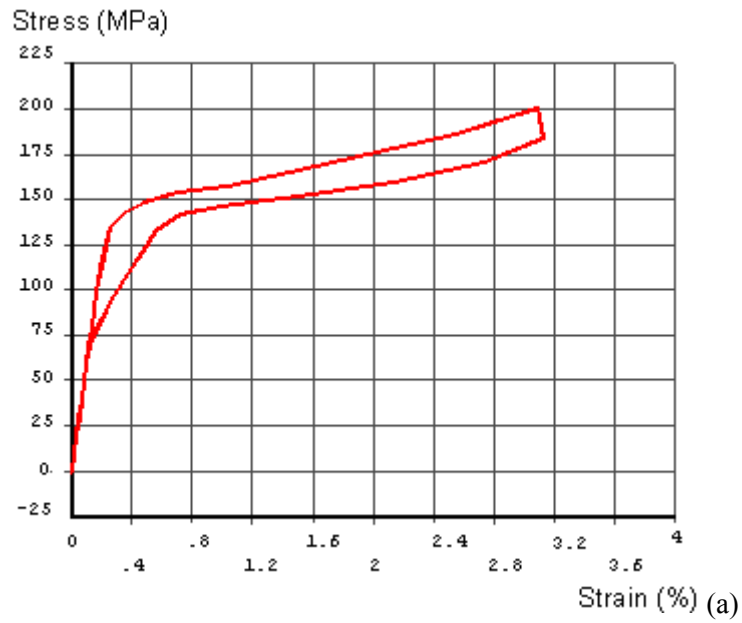


Figure 5.14: Stress-(average) strain obtained in the bar of Figure 5.10 for a cycle where axial-loading-is followed by bending: (a) node 24; (b) node 7.

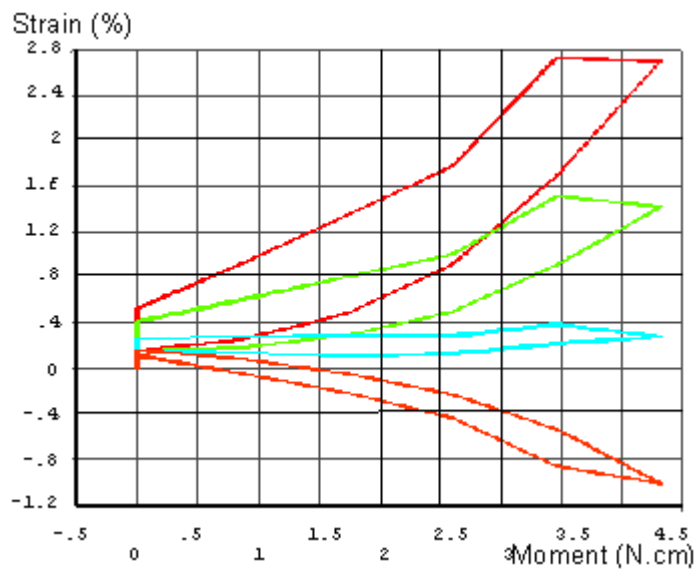


Figure 5.15: (Average) strain (ordinate) vs. bending moment (abscissa) obtained in the bar of Figure 5.10 for a cycle where axial loading is followed by bending. The nodes are 24, 7 and their symmetric ones (8, 20) from the top to the bottom.

This last plot is drawn again but in the case when the tension action is replaced by a compression force. The final vertical compression has the same absolute value of 2415 N (as in the tension case), and the horizontal added force is always of 880 N.

Similarly, the four diagrams “strain vs. bending moment” in nodes 24, 7, 8 and 20 are drawn in Figure 5.16.

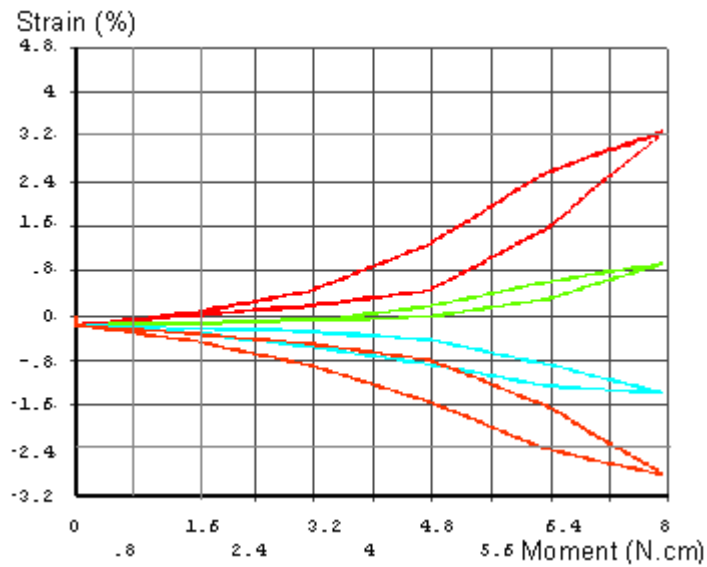


Figure 5.16: (Average) strain (ordinate) vs. bending moment (abscissa) obtained in the bar of Figure 5.10 for a cycle where axial compression loading is followed by bending. The nodes are 24, 7 and their symmetric ones (8, 20) from the top to the bottom.

Figure 5.17 shows the dependence of the strain in these four equi-spaced nodes along the base section (when considering the vertical action as tension). Figure 5.17a is drawn in the step when the applied moment was of 4.32 N.cm, where Figure 5.17b when the moment was only 2.16 N.cm. It is worth noting how the neutral axis moves as the moment increases.

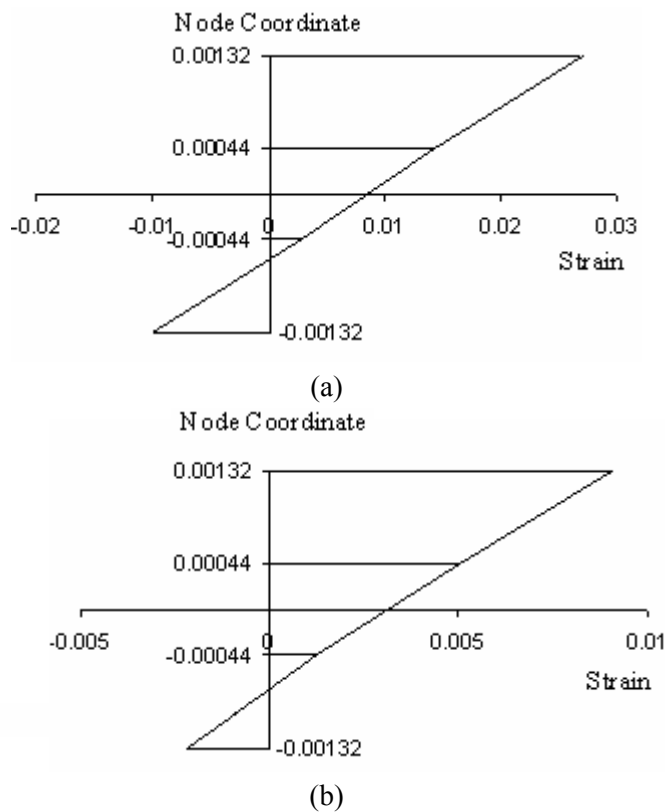


Figure 5.17: Different location of the neutral axis for, (a) $M = 4.32$ N.cm and (b) $M = 2.16$ N.cm.

5.7 Experimental features

Among the several tests that were conducted by using the universal material testing machine, MTS 858 Microbionix II, also available in the Vibrational Laboratory of the Structural Mechanics Department at the University of Pavia, Figure 5.18 collects two meaningful examples. They were obtained for bars of diameter 2.85 mm at ambient temperature. The stress was calculated from the load measured by the machine load cell; the strain was directly read by the extensometer. The tests were driven in deformation control during the loading

and in load control during the unloading. The bar in Figure 5.18a underwent the following process:

- Preliminary thermal treatment [Casciati and Faravelli, 2004] (aging);
- 20 cycles from 0% to 1% of strain;
- 3 cycles up to the strain of 2%;
- 1 cycle up to 3% of strain.

The test speed was of 0.05 mm/s. The following comments arise:

- a) on a virgin bar, the first cycle follows its own path; several cycles (training) are required to stabilize the response;
- b) the same test conducted without thermal treatment, would not have seen the knee to the plateau between 100 and 150 MPa, but between 220 and 300 MPa;
- c) if it is true that the loading always follows the same backbone curve, it is false that the unloading always follows the same path. The actual unloading path depends on the maximum value achieved by the strain. This is due to the production of fractions of martensite (from the original full austenite state). This production is also related to the residual displacement met at the end of the unloading.
- d) the initial (austenite) elastic Young modulus is 61300 MPa, while decreasing to 3500 MPa in the “plateau” region. The bar in Figure 5.18b underwent the following process:
 - Preliminary thermal treatment;
 - 20 cycles from 0% to 4% of strain.

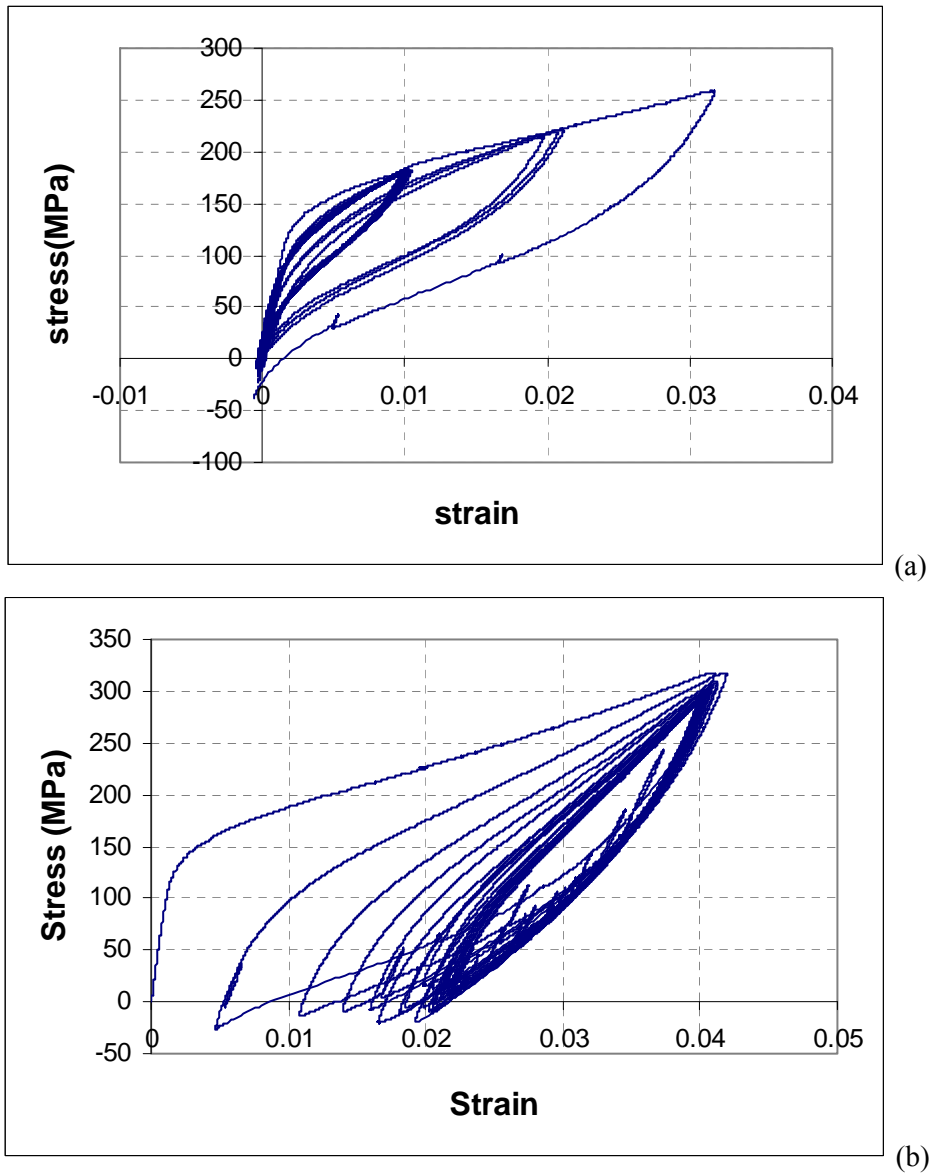


Figure 5.18: Stress- strain obtained in the bar tests under tension load.

The test speed was once again 0.05 mm/s. The further comment arises:

1. carrying the training in the range up to 4% produces a step by-step growth of the martensite. The presence of martensite fractions induces residual displacements. Therefore, loading–unloading cycles expected between 0 and 4% of strain actually occur between 2% and 4% of strain!;
2. when the strain approaches the 4%, the Young modulus increase again up to 5000 MPa. Moreover, it is worth noting: the progressive decrease of the Young modulus for subsequent loading cycles (from austenite to martensite) so that the martensite Young modulus can be estimated around 20000 MPa.

As the temperature is increased, the “plateau” is reached at higher levels of stress and the rupture elongation becomes lower.

As a conclusion on this comparison between numerical model and actual behaviour of the alloy bar, one should be aware that the numerical model contains so many approximations and simplifications that the results achieved by it are more qualitative than quantitative. Next section will use this numerical model just to find the general features of the device toward the design of a prototype. Nevertheless, attention will be focused on some global response measures which can be easily compared from the results of the experimental validation tests on the prototype itself.

5.8 Conceiving the device prototype

As sketched in Figure 5.19 (for a case of 12 bars model), more bars are assembled into a device model. Several static analyses were conducted with different applied load (following linear or sinusoidal law) and different bars length toward a better understanding of the behaviour of the system. The computational effort required by each static analysis allowed the author to run even complex models (say with 12 bars) discretized with 3-D 8-node solid elements. Then a device model with only 3 bars was considered and studied statically and dynamically. Each numerical model is loaded first by a vertical (compression) load, i.e., along the z-axis, to simulate the action of a superimposed mass (structure), then horizontal load along the x-axis is added.

The unloading is always done by first releasing the horizontal force, and then the vertical force to close the cycle. Note, that the vertical action is applied following a linear law, while the horizontal load varies following a sinusoidal law.

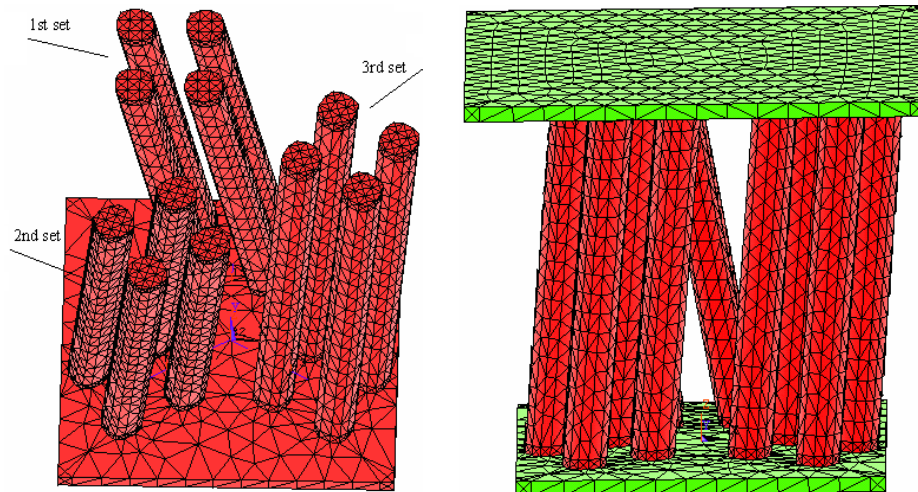


Figure 5.19: Numerical model for the whole device: four bars are incorporated in each of the three oblique sets.

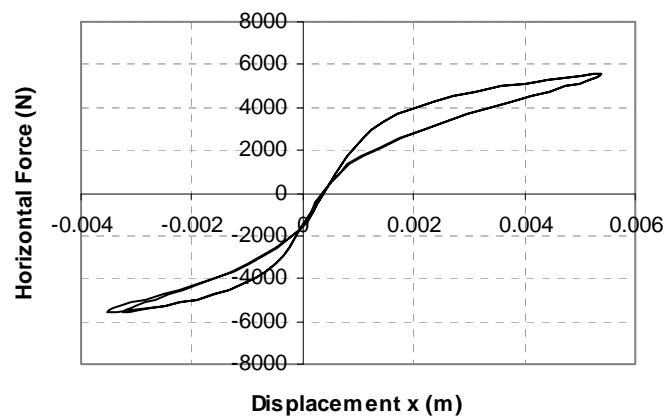
5.8.1 The 12-bars device

The device prototype studied here is assumed to transfer all the interface forces between upper system and foundation: in particular it carries the vertical component of the force. This is required to investigate the feasibility of a device in which each of the three bar inclinations is served by several bars (say 4). The device in Figure 5.19 is formed by 12 SMA bars of diameter 5.3 mm, 4 for each inclination set, disposed in a “Y” shape. The bars, inclined by 10 degrees from the vertical axis z , are fixed at the top and bottom of the steel plates. Moreover a base isolator must allow relative displacements between the top and the bottom. The physical limit to this displacement is larger as the bar length is larger. But the two requirements (to carry the vertical force versus large allowable relative

displacement) are in conflict with one another. Two options were therefore considered: short bars of length 5 cm and long bars of length 20 cm.

5.8.1.1 Short-bar model

The finite element model of the short-bar device, which is made by 12 SMA bars of 5 cm length, consists of 5159 nodes and 17396 3-D 8-nodes elements. A vertical (i.e., acting along the z -axis) compression load of 12.60 kN is first applied. The vertical displacement achieved is 0.082 mm under this vertical load. Then, an additional horizontal force of 5.6 kN is added in the x direction following a sinusoidal law. In view of the final comparison with experimental results, the global behaviour of the device is conveniently described by diagrams plotting the horizontal force versus the three generalized displacements (along x , along y and the rotation around z) of the top plate. They are summarized in Figure 5.20 (a-c), for two clockwise cycles of loading-unloading. It is also of interest to see how the force is related with the velocity along x : the plot is in Figure 5.21, with an anti-clockwise reading. The hysteresis loop is evident, while the maximum top-bottom relative displacement is only 5 mm. the force values are rather low, but larger values de-stabilize the analysis.



(a)

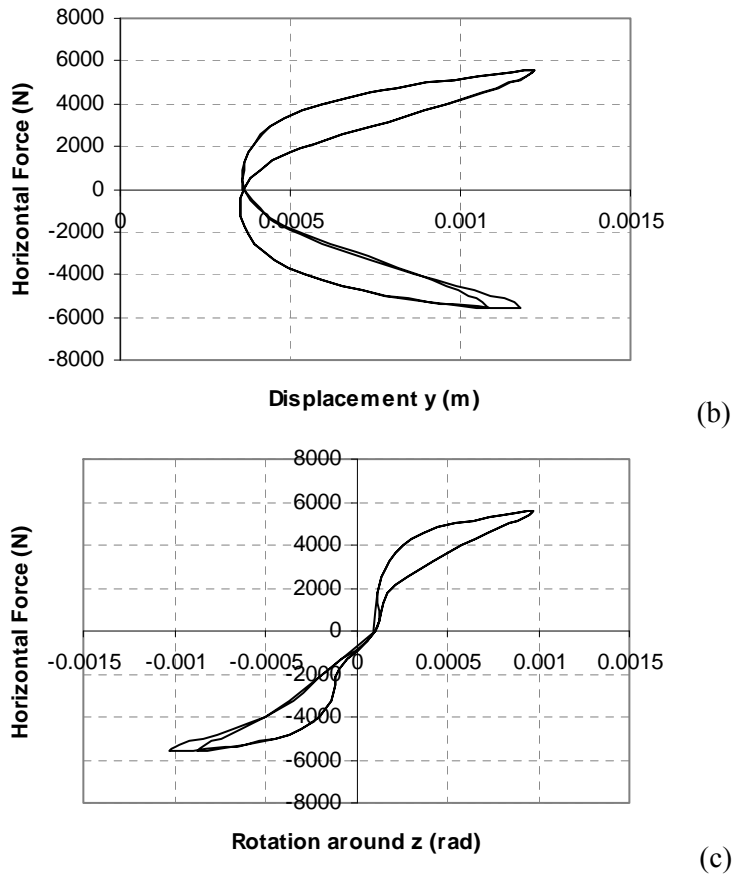


Figure 5.20: (a), (b) and (c): maximum top displacements vs. horizontal force (two cycles).

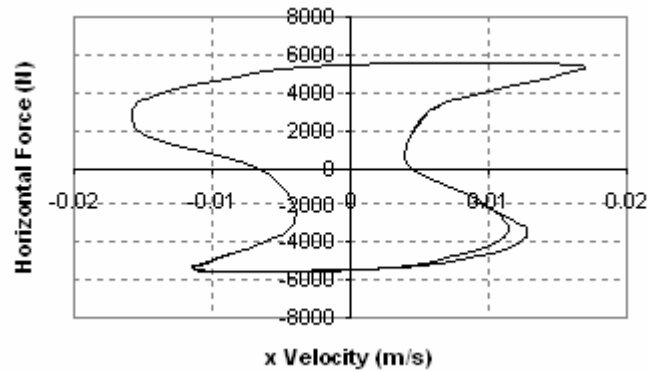
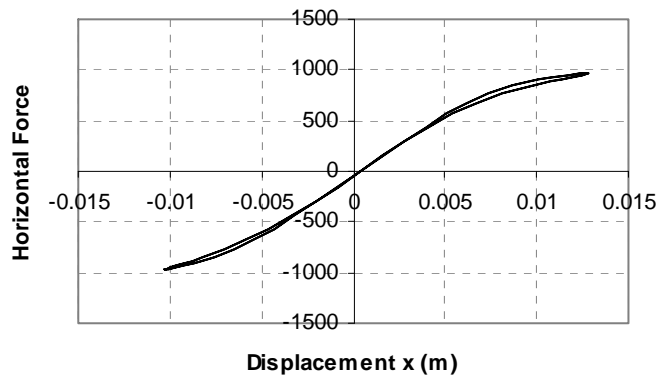


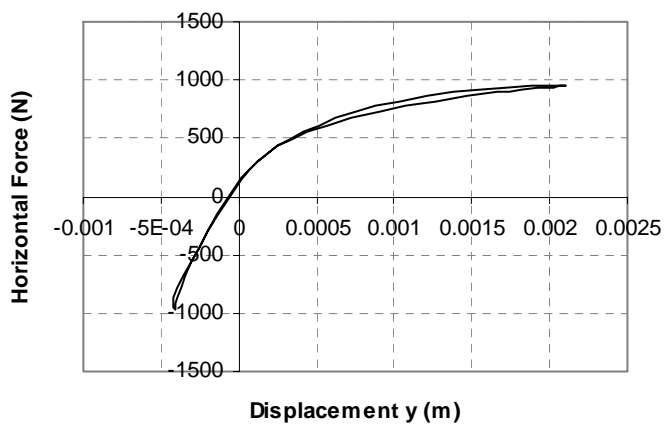
Figure 5.21: Top horizontal velocity in the x direction vs. horizontal force (two cycles).

5.8.1.2 Long-bar model

When dealing with the long-bar scheme, the finite element model of the device made of 12 SMA bars of 20 cm length consists of 17109 nodes and 55744 3-D 8-nodes elements. Let the vertical load be 2.4 kN in this case (less than 1/5 of the value used in sub-section 5.7.1.1!). The vertical displacement achieved is 0.153 mm under the vertical load. An additional horizontal force (in the x direction) of 0.92 kN, is then added following a sinusoidal law. The plots of the horizontal force versus the generalized displacements for two cycles of loading-unloading are presented in the set of Figure 5.22 (a, b and c) and 5.23, where the relation between the force and the velocity along x is shown. The hysteresis nearly disappears, while the maximum relative displacement jumps up to 13 mm, when compared with the results in Figure 5.20. The comparison between Figures 5.21 and 5.23 emphasizes a wider hysteresis loop.



(a)



(b)

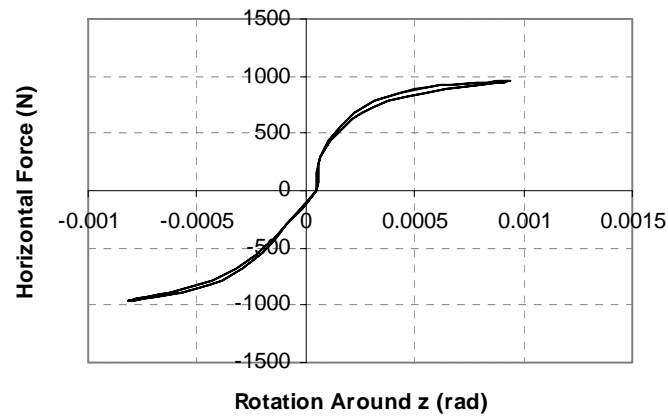


Figure 5.22: (a), (b) and (c): maximum top displacements vs. horizontal force (two cycles).

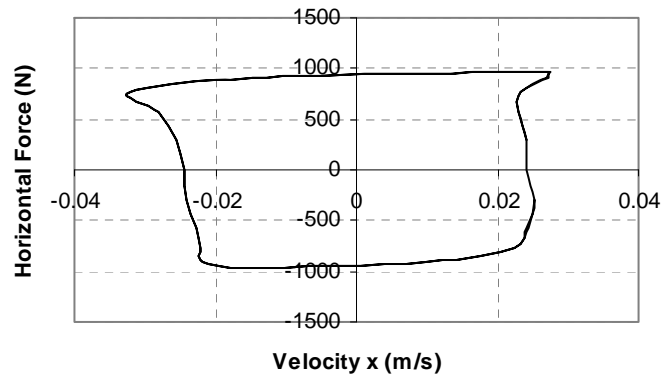


Figure 5.23: Top horizontal velocity in the x direction vs. horizontal force (two cycles).

5.8.2 The 3-bars device

Attention is now focused on the 3-bars device prototype in Figure 5.24. It is made by bars of diameter 3.5 mm and 20 cm length, with one bar in each inclination set. The device model is numerically built again by adopting the 3D

8-nodes solid element offered in [ANSYS, 2003] for each SMA bar (Figure 5.24b). The associated finite element model consists of 5593 nodes and 14669 elements.

Several devices were conceived with different inclinations of the bars over the z -axis, namely 0° , 15° , 30° , 45° and 60° .

Here, the steel plates assembling the top and bottom of the bars are both of thickness 5 mm. Three fractions of vertical/horizontal forces are assumed for the five built devices (each with a different inclination angle). The vertical force is always kept of 75 N (less than 1/10 than in sub-section 5.7.1.2!). The vertical displacement achieved is 1.515 mm under the vertical load. The horizontal force is taken equal to the vertical load multiplied by the factors 0.1, 0.25 and 0.28, respectively, i.e., the adopted horizontal forces are 7.5, 18.75 and 21 N. Figure 5.25 summarizes these results. Its inspection identifies the optimum configuration as the one with a bar inclination around 30 degrees from the vertical axis z . This optimum depends on the horizontal force level (see Figure 5.25b) and the length of the bars. Thence, it must be regarded as a peculiar result of the studied cases.

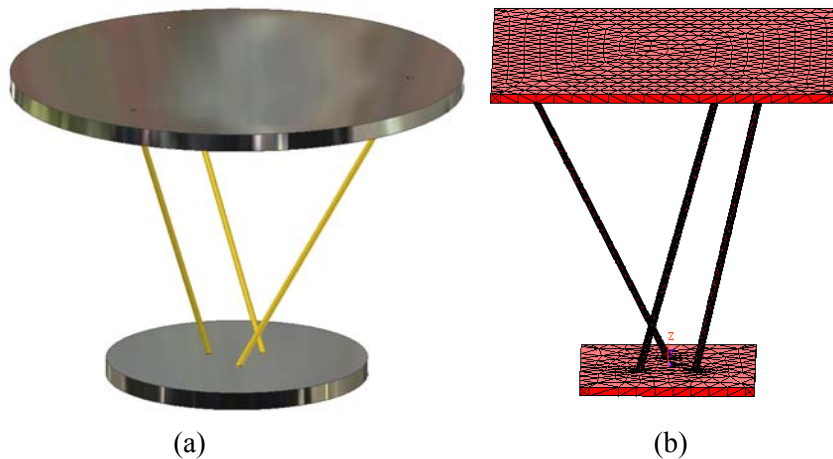
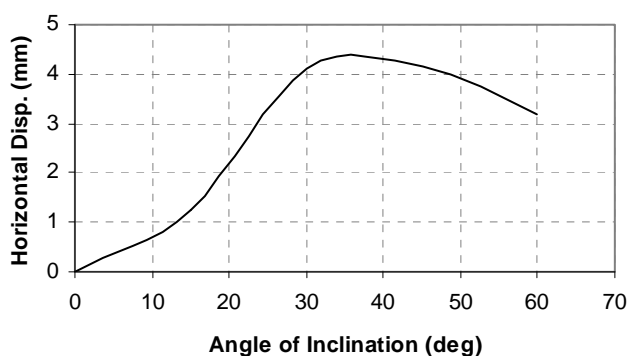
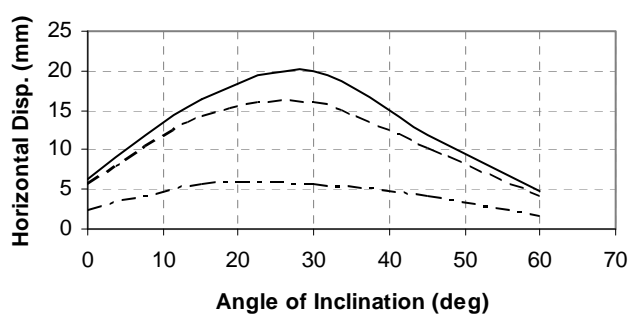


Figure 5.24: (a) 3D sketch of the proposed 3-bars passive device. (b) Numerical model for the 3-bars device.



(a)

--- 0,1 - - - - 0,25 ——— 0,28



(b)

Figure 5.25: (a) Horizontal displacement (due to the vertical force) vs. angle of inclination of the bars. (b) Horizontal displacement (due to the horizontal force applied after the vertical one) vs. angle of inclination of the bars.

5.8.2.1 Static characterization

To describe the global behaviour of the 3-SMA-bars device (with the optimal inclination of 30°), the diagrams plotting the horizontal force versus the displacements along x , y and the rotation around z of the top plate are drawn. They are given in Figure 5.26 (a, b and c) for one cycle of loading–unloading. The plot showing the relation between the horizontal applied force and the velocity along x is provided in Figure 5.27. It is seen that a relative

displacement less than 3 mm is achieved, while the hysteresis loop is nearly totally disappeared.

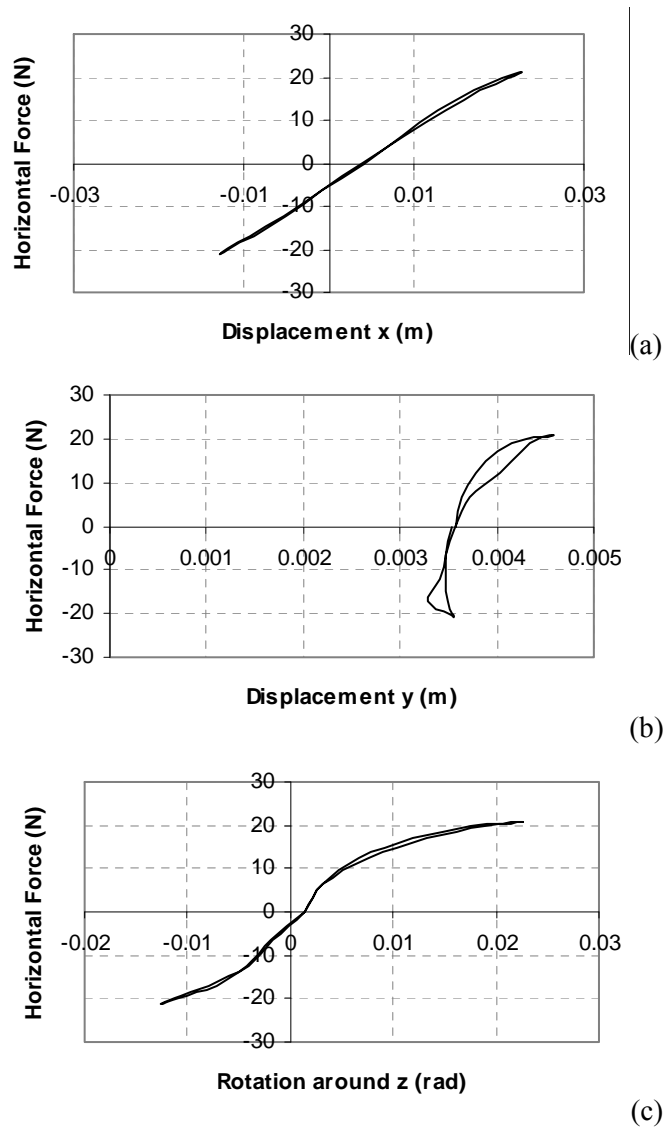


Figure 5.26: (a), (b) and (c): top displacements vs. horizontal force for a sinusoidal variation of the horizontal load (with sinusoidal variation of force).

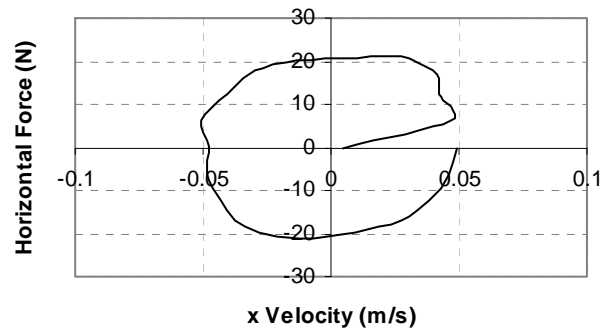
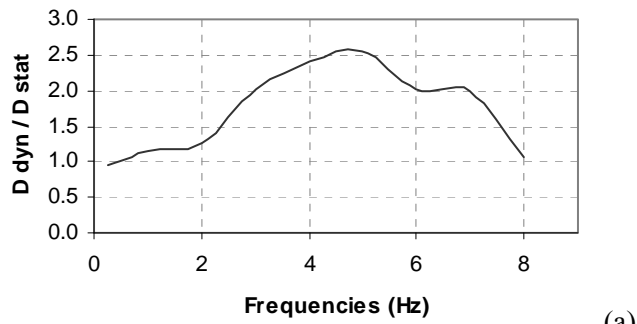


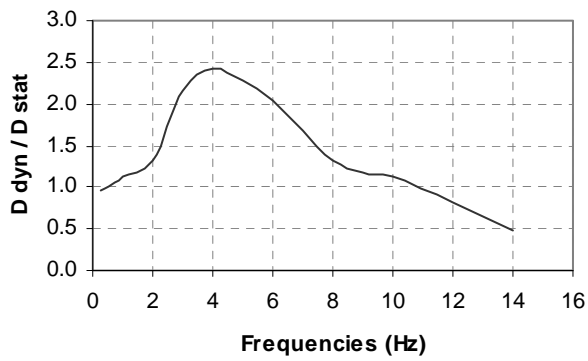
Figure 5.27: Top horizontal velocity in the x direction vs. horizontal force.

5.8.2.2 Dynamic characterization

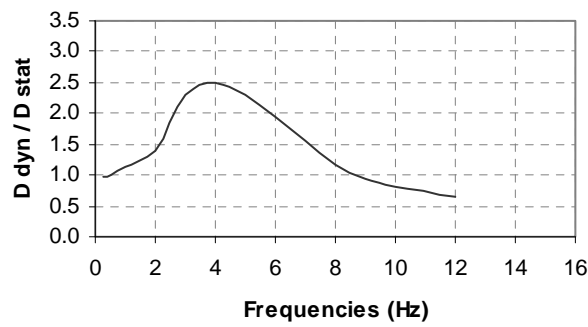
Attention is focused now on the dynamic characterization of the device. The modal analysis of the numerical model would provide fundamental frequencies of 4.58, 4.74 and 8.12 Hz but this requires that the SMA bars are regarded as fully elastic with Young modulus equal to the initial value shown in the austenite phase. Due to the actual non-linearity of the SMA constitutive law, the device must be analyzed dynamically under a sinusoidal excitation of increasing frequency. The analysis was repeated for three different intensities of the horizontal load: 5% of the static peak horizontal load of 21 N (Figure 5.28a), 20% of the static peak horizontal load (Figure 5.28b) and 50% of the static peak horizontal load (Figure 5.28c). The detected fundamental frequency moved from 4.58 to 4.00 and 3.50, as expected because a lower equivalent stiffness replaces the initial one, as the excitation intensity increases.



(a)



(b)



(c)

Figure 5.28: Dynamic amplification diagram for: (a) the lower, (b) the medium and (c) the higher intensity of the horizontal load.

5.8.2.3 Summary of the numerical investigation

The numerical investigation pointed out the weakness of a device conceived to directly support the vertical component of the interface force. Only very low values of the relative displacement are allowed in this case and the bearing capacity is very modest.

5.9 Geometry of the experimentally tested device

Following the numerical analyses, the base isolator deeply studied in the previous section have been realized and tested. It is composed of two disks, one vertical cylinder with an upper enlargement sustained by three horizontal cantilevers, and at least three inclined SMA bars.

Recall that the adopted finite element code for this analysis, unfortunately, restricted the definition of the studied material only as plane or solid element. A general purpose finite element code offering a super-elastic constitutive law was adopted for this analysis. Unfortunately, the use of this material routine was restricted to plane and solid finite elements. Therefore, and as presented in the numerical analysis, hexagon elements were adopted to discretize each SMA bar, which made the computational effort very difficult. In addition, the routine did not account for the actual austenite-martensite transformations and was inadequate in managing the different responses of the device to tension and compression. As a result, the numerical response was not consistent with the experimental evidence and some changes were made for the laboratory tested prototype.

The following geometric parameters characterize the assemblage as illustrated in Figure 5.29:

- B = diameter of the bottom disk of thickness s_1 ;
- D = diameter of the top disk of thickness s_2 ;
- b = diameter of the vertical cylinder;
- φ = diameter of the SMA bar;

- l = length of the cantilever measured from the axis of the cylinder;
- L = length of projection of the cantilevers; a lateral view would provide $L = 1.5 l$; a front view would provide $L = 3l/2$;
- h = distance between the two horizontal disks;
- d_1 = diameter of the inner circle on the bottom disk where the bars are placed;
- d_2 = diameter of the inner circle on the top disk where the bars are placed.

Note that the bars are not only joining points on circles of different diameters, but the points on the top circle are rotated 180° .

The disks and cylinder can be made of steel, aluminium or nylon. The SMA [Auricchio et al., 2001] adopted in this thesis is the copper-aluminium-beryllium (Cu-Al-Be) alloy studied in depth by the author, during his stage at the University of Pavia [Casciati and Faravelli, 2004], [Casciati and Faravelli, 2007], [Casciati and van Eijk, 2008]. Its important features are its austenite transformation finish temperature, which is lower than 0°C , and its ability to preserve the shape of its hysteretic super-elastic cycles up to temperatures much higher than 100°C . A similar device, with the alloy bar fixed both at the bottom and top disks, was investigated in depth numerically by the author and his supervisor [Casciati et al., 2006], [Casciati et al., 2007a, b, c and d].

The first laboratory tests were carried out as reported in [Casciati and Hamdaoui, 2008] and some noteworthy observations are as follows:

1. A device made only of inclined SMA bars, without the presence of the vertical cylinder, could also be realized, but the vertical sustainable load would result strongly reduced. Moreover, the expected benefit of adopting SMA bars is undermined by the large amount of resources required to support the vertical loads;
2. Bars fixed at the top disk, as modelled in the numerical studies, result into rotations of the top disk around the vertical axis, as well as in its rolling due

to the large displacement geometric effect; this suggests that sliding bars must be much longer than the length required at rest;

3. When the bars are fixed at both ends and also support the vertical loads, the bar inclination on the vertical axis was optimized. The optimum value was shown to be 30° and this design value is adopted in the prototype built and tested in this paper.

The fatigue performance of the bars (as investigated in [Casciati et al., 2007e]) was very satisfactory. Moreover, the bars were fully recovered after cycles of loading and unloading using suitable thermal treatments [Casciati, 2007].

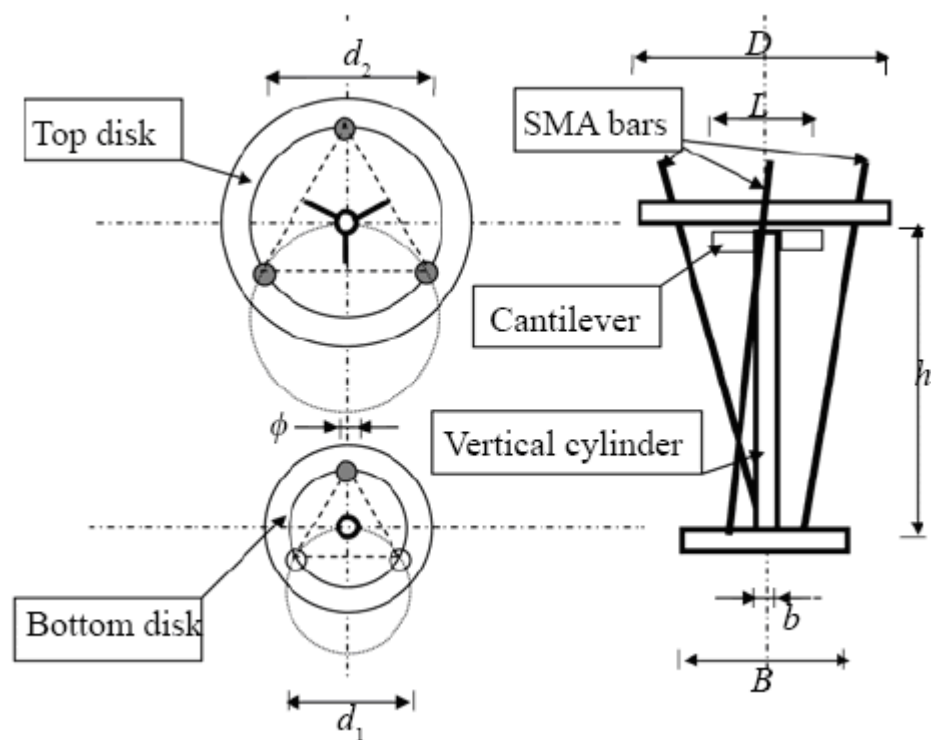


Figure 5.29: Geometry of the proposed device. The view on the left is from the top on the bottom disk and from the bottom on the top disk.

5.10 Prototype test and system identification

Figure 5.30 provides the details of the prototype base isolator (made by two aluminium disks, three SMA bars and one vertical cylinder). The upper aluminium disk (diameter $D = 25$ cm and thickness $s_1 = 2$ cm) serves as a superimposed tray: the system to be isolated will be mounted on it. The three SMA bars have a diameter of $\varphi = 3.5$ mm and >20 cm long. The bars, inclined 30° on the vertical axis z , were free to move at the top end but fixed at the bottom to the lower aluminium disk (diameter $B = 15$ cm and thickness $s_2 = 1.5$ cm).

The role of the vertical shaft, with a diameter of $b = 2.6$ cm (4 cm in the upper part) and a height of $h = 16$ cm, placed at the centre of the tested prototype, is to absorb the vertical load of the structure to be isolated. Consequently, only the horizontal action engages the inclined SMA bars. Note that between the head of the cylinder and the top aluminium disk, a Teflon layer is added to facilitate the sliding. To complete the prototype geometry, the diameter of the inner circle on the bottom disk where the bars are placed, is $d_1 = 3.8$ cm while the diameter of the inner circle on the top disk where the bars are placed, is $d_2 = 18.2$ cm.

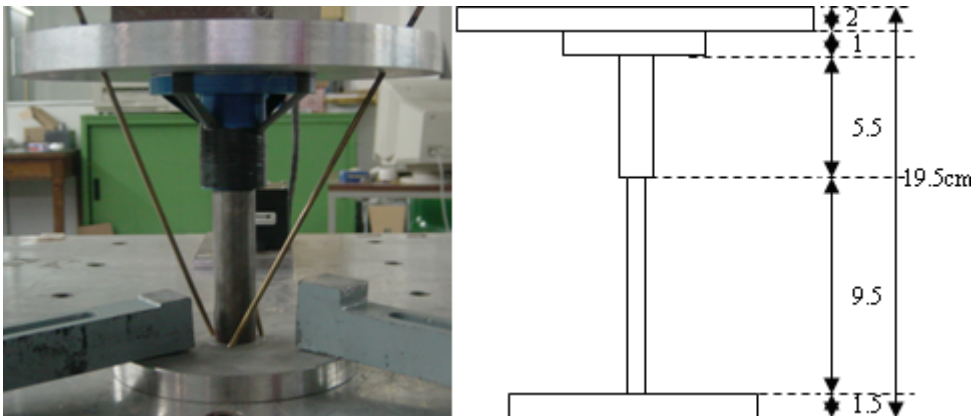


Figure 5.30: Prototype of base isolator (dimensions are shown in cm).

As shown in Figure 5.31, the device bottom disk is fixed to the shaking table in the Vibration Laboratory at the University of Pavia. A mass of 31 kg is placed on its top. The two accelerometers which were used to capture the accelerations are also shown on the shaking table and on the top of the device.

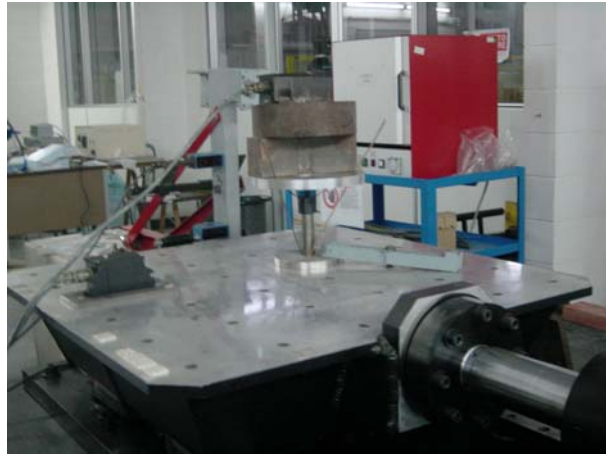


Figure 5.31: Prototype device fixed on the shaking table.

During the tests, an eight-channel acquisition system received the signals measured by four sensors. Two are mono-axial accelerometer FBA-11 EP-sensors, made by Kinemetrics, and are mounted on the table and top mass, respectively. The other two channels use two Wenglor non-contact displacement laser sensors (located on a mass outside the table) for measuring the displacements of the bottom and top disks.

The sensors are linked to the acquisition system through a junction box, which provides power to the sensors and, at the same time, receives the signals from them. An anti-aliasing filter at 10 Hz is performed by the acquisition device, before the A/D (analog/digital converter) transfers the signals to the PC for storage.

Standard shaking table tests were carried out to evaluate the dynamic characteristics of the structural model. Long records of the response were

collected when the model was excited at the base by acceleration white noise. The shaking table was driven by a displacement time history of long duration, i.e., 5 minutes, whose corresponding acceleration time history fits a white noise spectrum in the range from 0 to 20 Hz. The intensity was modified by either scaling the integrated displacement and forwarding it to the shaking table as reference input, or by modifying the shaker span.

However, the intrinsic nature of the device is nonlinear. The global stiffness primarily depends on the excitation intensity (due to the SMA constitutive law), while the device response is significantly different when above or below the force threshold, which results from friction and the SMA bar contrast. In order to identify the last force, it was decided to perform the tests by sinusoidal waves of displacement $u(t)$ of increasing frequency f for given span U of the shaking table piston:

$$u(t) = U \sin(2\pi ft) \quad (5.1)$$

where t denotes the time. The prototype device was tested for three sets of shaking span amplitudes: 10 mm, 12.5 mm and 15 mm. For each test, several sequences of sinusoidal excitations, with frequencies ranging from 1 to 4 Hz, were generated.

The sensor readings provide the measured time histories of the bottom and top displacements, $u_b(t)$ and $u_t(t)$, and accelerations, $a_b(t)$ and $a_t(t)$, respectively. They allow the relative displacement between the top and bottom disks to be estimated as follows:

$$\Delta u(t) = u_t(t) - u_b(t) \quad (5.2)$$

and the inertia force of the top mass:

$$F = ma_t(t) \quad (5.3)$$

The limit force F_Y is defined as the value of the force in Eq. (5.3) for which there was a discontinuity in Eq. (5.2). Note that the device does not have a symmetrical axis, but its geometry is based on equilateral triangles and should provide a type of isotropic response. The asymmetry in the values of F_Y in the two directions indicates a deviation from this isotropy. The pairs $(\pi 2 f^2 U, F_Y)$ revealed by the experiments are shown in Figure 5.32. Note that the force is nearly constant (around 62 N, as the difference between the laser sensors readings). The measurements were collected for three different values of vibration intensity, fixed by assigning the span of the shaking table piston: 10, 12.5 and 15 mm. Each excitation time history is sinusoidal of increasing accepting a flat friction coefficient of 0.2, the mass being 31 kg!). This means that the top acceleration at sliding is nearly the same, while the base acceleration decreases as the excitation intensity increases. In other words, the acceleration amplification factor (calculated as the ratio between the maximum absolute accelerations detected at the top over the bottom) varies with the excitation frequency even before the sliding.

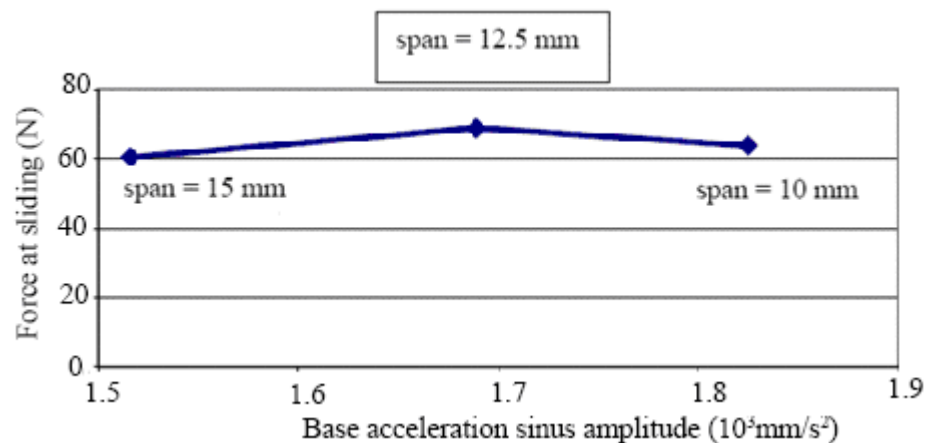


Figure 5.32: Pairs $(4\pi^2 f^2 U, F_Y)$ revealed during the experimental program.

In particular, the amplification factors of displacement and acceleration are different due to the nonlinear characteristics of the system. They are summarized in Figure 5.33 for the three span values adopted in the experimental program. The discontinuities in Figure 5.33a are due to the sensor resolution. The values shown in Figure 5.33b, higher than the corresponding values in Figure 5.33a, are due to the fact that the device stiffness increases to avoid large displacements, which results in values of the top acceleration being comparable with those at the base (see Section 5.10 for a more detailed explanation).

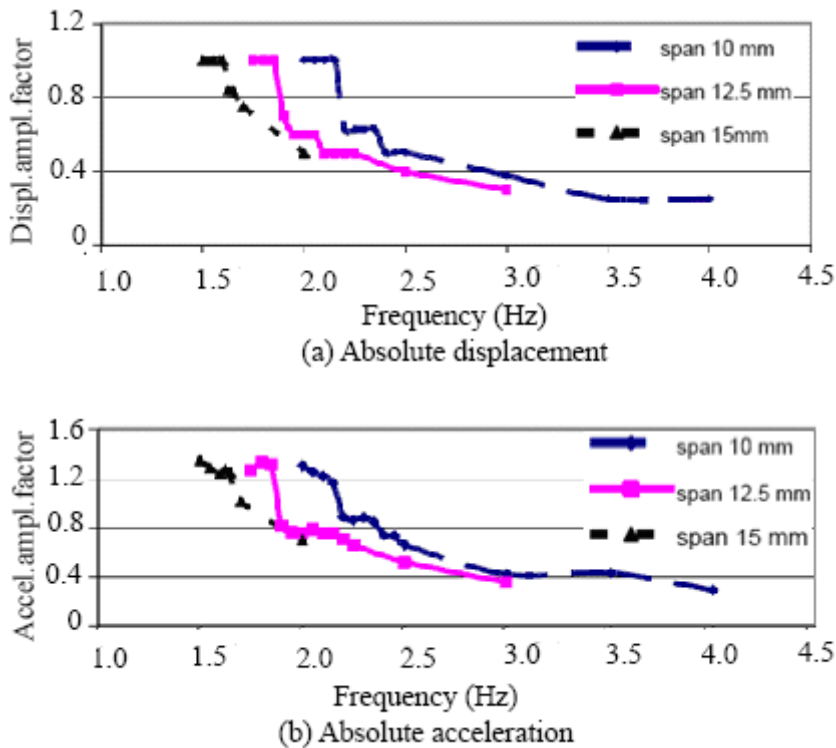


Figure 5.33: Amplification factors.

The sliding threshold satisfies the first requirement listed in the introduction; that is, the sliding should not occur under low intensity excitations to counteract

static or semi-static actions. Reparability is satisfied by the simple assemblage scheme of the device, while the suitability of the working temperature is achieved by the specific selection of the shape memory alloy.

5.11 Test details and hysteresis loops

As mentioned in the previous section, hysteresis is pursued in the relationship between the force at the top of the device (estimated from the measured top acceleration) and the relative displacement (achieved frequency).

5.11.1 Test with amplitude of 10 mm

The test was started with an initial frequency of 2 Hz; it was then slowly increased up to 4 Hz. Signals were recorded for the following intermediate values: 2.00, 2.05, 2.10, 2.15, 2.20, 2.25, 2.30, 2.35, 2.40, 2.45, 2.50, 3.00, 3.50, 4.00 Hz.

Initially no significant relative displacement between the top and the bottom disk was detected. In other words, the top force was lower than the friction force between the upper side of the vertical cylinder and the aluminium plate. At the frequency of 2.20 Hz, the top plate moves independently of the bottom disk; the hysteretic behaviour is emphasized as seen in Figures 5.34 and 5.35. Similar plots could be reported for all the tests excited at greater values of the frequency.

In Figure 5.34, from the rest to the stationary cycles, the force varies first, for negligible relative displacements, below the negative threshold. Then, the threshold is achieved and the graph follows a few irregular loops until the motion stabilizes along the stationary cycles. Each cycle shows low forces at zero displacements and peak values of nearly 40N (and -40N) for large positive relative displacements (15mm) and large negative values (-15mm).

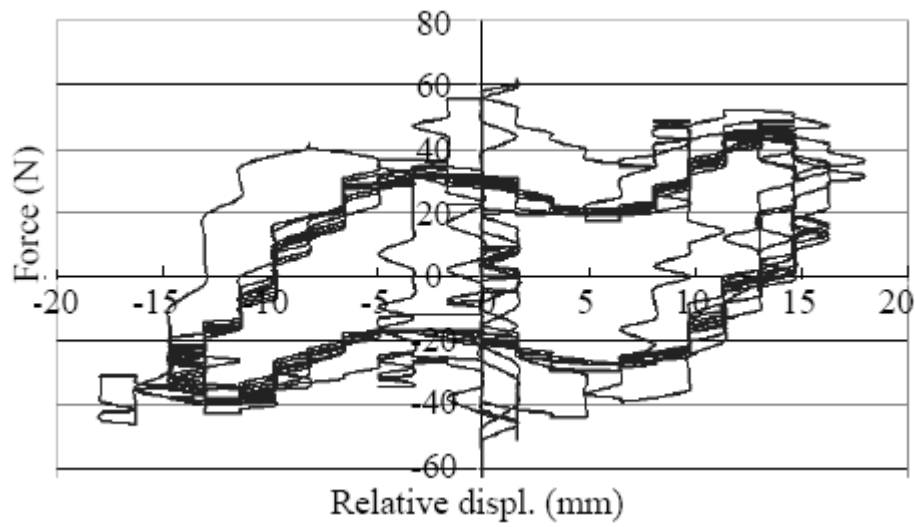


Figure 5.34: Top force vs. relative displacement: amplitude 10 mm, frequency 2.20 Hz. From the rest to the stationary response: duration 8 s.

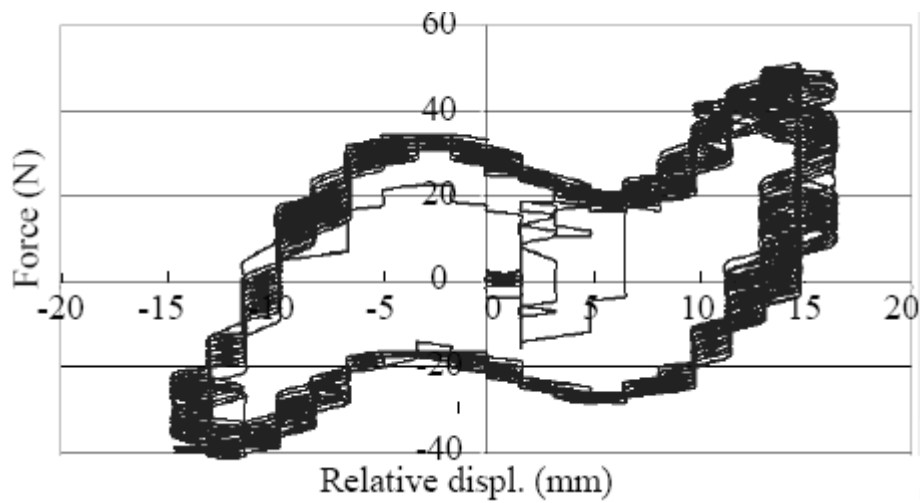


Figure 5.35: Top force vs. relative displacement: amplitude 10 mm, frequency 2.20 Hz. From the stationary response to rest: emphasis on the re-centring ability.

In Figure 5.35, the stationary response is perturbed when the excitation is switched off; note the ability of the device to re-centre itself, with force and displacement returning to the initial rest position. To understand the response in more detail, the acceleration signal was filtered by a band-pass between 0.5 and 4 Hz. The plot of the filtered force is shown in Figure 5.36, where contributions to the global motion in Figures 5.34 and 5.35 of higher frequency modes, which are now suppressed, are seen. The filtered time history shows a constant time delay of the peaks with respect to the peaks achieved by the base acceleration.

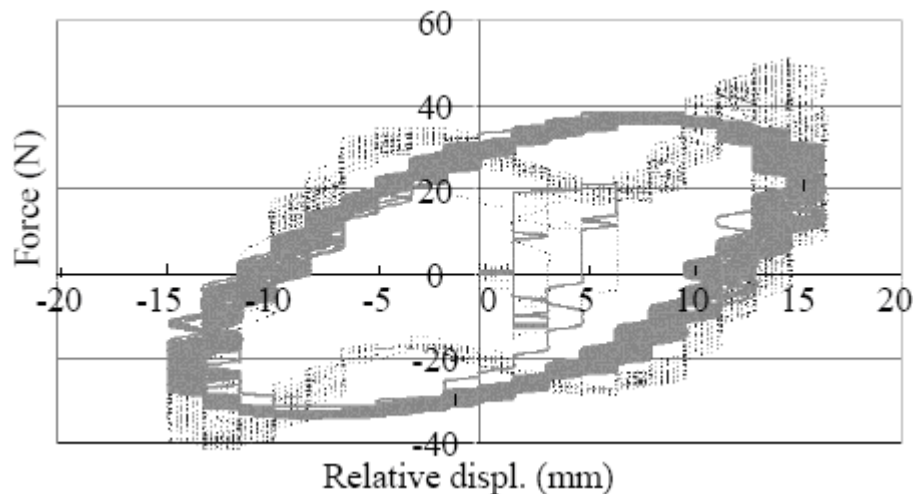


Figure 5.36: Top force vs. relative displacement: amplitude 10 mm, frequency 2.20 Hz. From the stationary motion to rest. Actual signal in dotted line; filtered signal in solid line.

As the frequency increases, two stages occur: first, the top acceleration increases, as does the force; then the base isolation actually occurs. In stage 1, an increase of the maximum relative displacement would be expected, but as shown in Figure 5.37 for a frequency of 2.35 Hz, the device reacts by increasing the stiffness, which constraints the maximum displacement to remain at 15 mm. However, the corresponding acceleration peak does not de-amplify.

Note that the device globally reacts in a way quite similar to any elastomeric material, showing an initial stiffness at low strain, a large flexibility at a strain of 100% and finally a large stiffness, which prevents very large displacements.

When the frequency is further increased, a full isolation is reached (stage 2). The hysteresis assumes the shape in Figure 5.38, drawn for a frequency of 4 Hz, and the maximum value of the relative displacement is lower than the values in Figures 5.34 to 5.37.

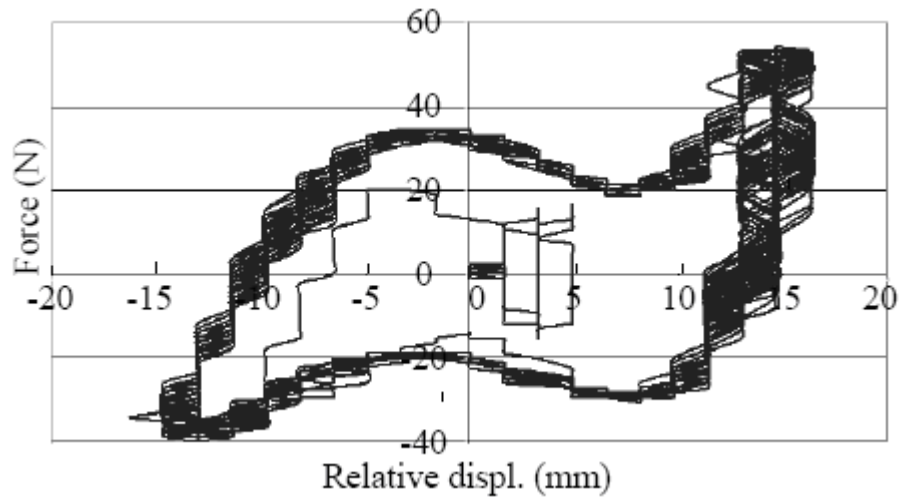


Figure 5.37: Top force vs. relative displacement: amplitude 10 mm, frequency 2.35 Hz. From the stationary response to rest: emphasis on the way the maximum displacement is limited by increasing the force value.

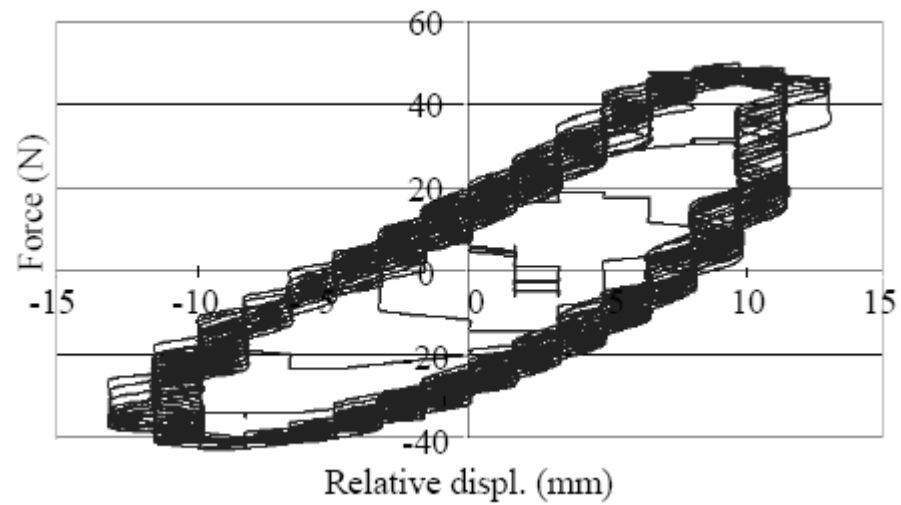


Figure 5.38: Top force vs. relative displacement: amplitude 10 mm, frequency 4 Hz. From the stationary response to rest: emphasis on the reduced value of the maximum displacement.

5.11.2 Test with amplitude of 12.5 mm

In this test, the oscillation amplitude is increased by adopting a span value of 12.5 mm. Here, the initial frequency is 1.75 Hz, and is slowly increased up to 3 Hz (1.75, 1.80, 1.85, 1.90, 1.95, 2.00, 2.05, 2.10, 2.15, 2.20, 2.25, 2.50, 3.00 Hz). The first hysteresis loop was detected for the frequency of 1.90 Hz, i.e., the horizontal force exceeded the friction force between the upper part of the vertical shaft and the aluminium plate. Figures 5.39 and 5.40 plot this situation, while Figure 5.41 provides the graph obtained for 3 Hz. Note that the maximum relative displacement is now 20 mm.

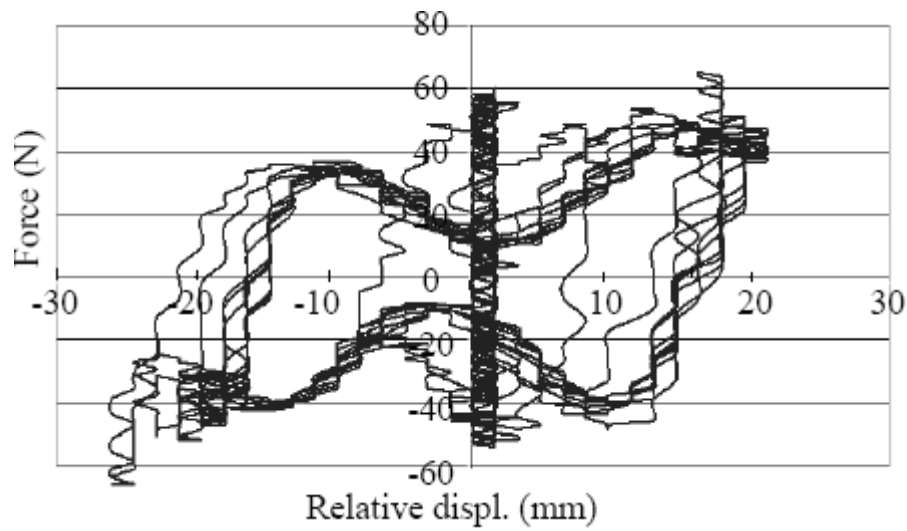


Figure 5.39: Top force vs. relative displacement: amplitude 12.5 mm, frequency 1.90 Hz. From the rest to the stationary response: duration 12 s.

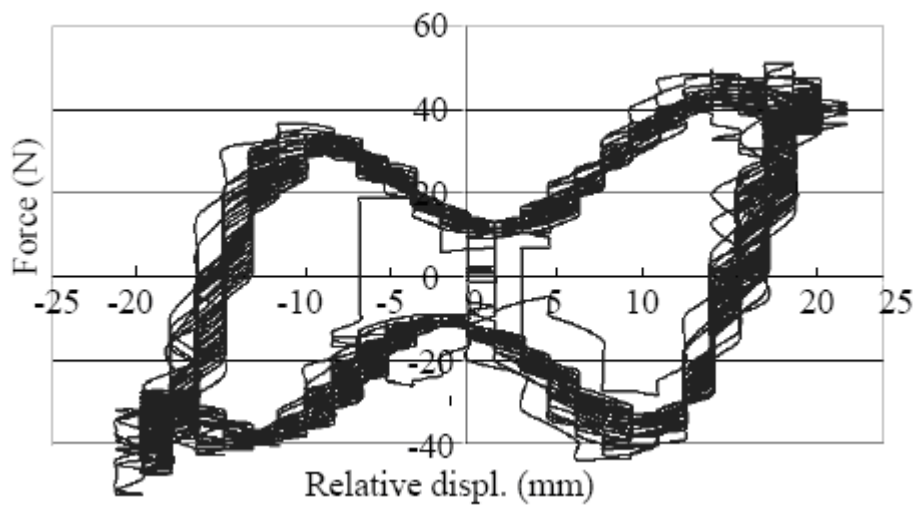


Figure 5.40: Top force vs. relative displacement: amplitude 12.5 mm, frequency 1.90 Hz. From the stationary response to rest: emphasis on the re-centering ability.

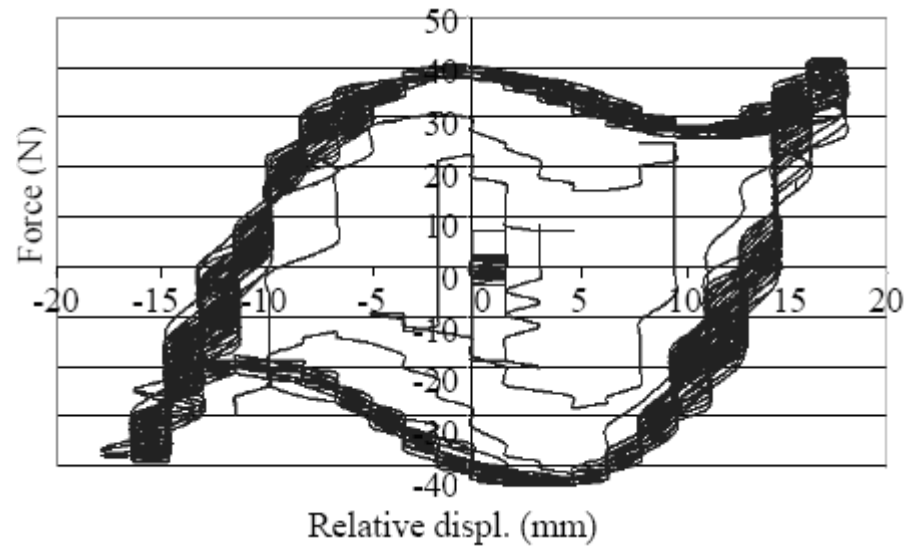


Figure 5.41: Top force vs. relative displacement: amplitude 12.5 mm, frequency 3 Hz. From the stationary response to rest: emphasis on the reduced value of the maximum displacement.

5.11.3 Test with amplitude of 15 mm

In the test with the largest span value of 15 mm, the initial frequency was 1.50 Hz, and gradually increased up to 2 Hz (1.50, 1.55, 1.60, 1.625, 1.65, 1.70, 2.00 Hz). The friction force threshold was achieved for a frequency of 1.625 Hz. Figures 5.42 and 5.43 illustrate this situation. Note that while the displacement amplification factor is small, the one associated with the acceleration is large. Indeed, large accelerations are required to prevent large displacements. The value of the maximum relative displacement (25 mm) also increased.

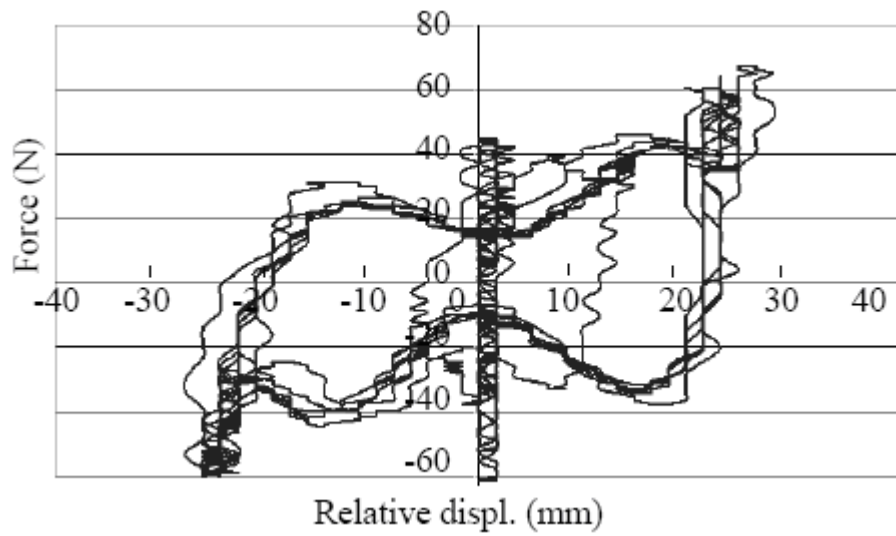


Figure 5.42: Top force vs. relative displacement: amplitude 15 mm, frequency 1.625 Hz. From the rest to the stationary response: duration 12 s.

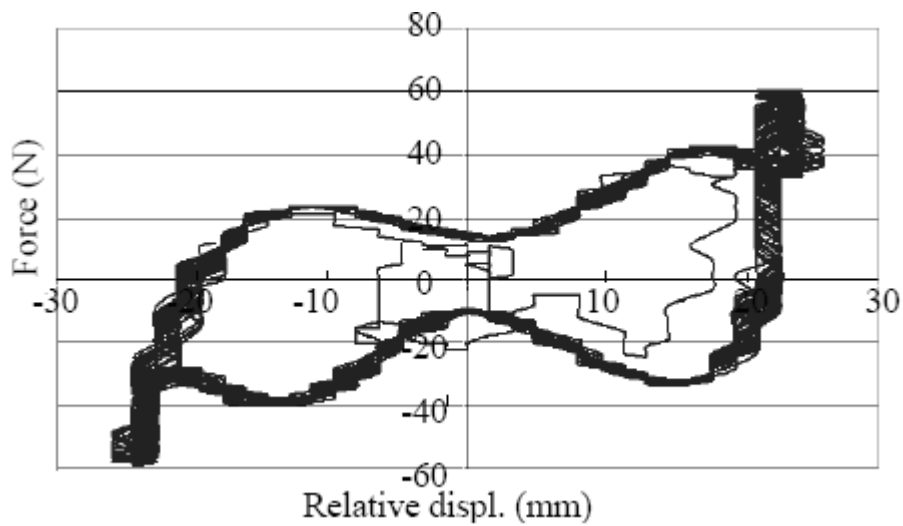


Figure 5.43: Top force vs. relative displacement: amplitude 15 mm, frequency 1.625 Hz. From the stationary response to rest: emphasis on the re-centring ability.

5.12 Conclusion

This chapter describes a new and innovative base isolator in which a sliding system is coupled with inclined bars in shape memory alloy in its austenite phase. These bars have four functions:

- (i) to provide stiffness against low intensity excitations;
- (ii) to contrast very large displacements;
- (iii) to re-centre the device;
- (iv) to dissipate energy during the motion.

The presented prototype is modelled and tested. It just utilizes the geometric mutual collocation of inclined bars made of the Cu-based shape memory alloy. To model this specific material requires a very complex constitutive law description, possibly accounting for the martensite fractions in it. When bars of this alloy are assembled into a structural system, the compromise between accuracy and feasibility (as achievable through commercial software) strongly penalizes the former requirement, resulting in numerical results roughly representative of the actual system response.

Based on experimental observations carried out on a model, the main feature is that for cyclic loading, the super-elastic behaviour of the alloy results in wide load-displacement loops, where a large amount of energy is dissipated. These loops become smaller and smaller as the excitation intensity decays, resulting in the device re-centering.

The following research topics should be investigated in more detail:

1. Dynamic comparison: the behaviour of the sliding system without SMA bars should be recorded during experimental tests where the excitation is increased up to the collapse of the top disk;
2. Performance characterization: the ratio between the diameters of the top disk over the bottom disk should be optimized;

3. Geometric design: the bar inclination should be optimized; it is likely that this depends on the device height and the above diameter ratio;
4. Numerical modelling: the difficulties met in achieving a satisfactory modelling of the shape memory alloy mainly depend on the adoption of solid hexagonal finite elements; refinements of the mesh only where absolutely necessary or the development of user subroutines that account for specific exploitation of the alloy should be investigated;
5. Carrying capacity: while waiting for a reliable numerical model, the existing device should be tested with different masses to identify the vertical carrying capacity to allow a large enough margin to undergo horizontal motions;
6. Design scaling: until a reliable numerical model is developed, prototypes of different sizes should be constructed to collect preliminary information on the way a larger device could be developed;
7. Alloy alternative: despite being more expensive, nickel-titanium (Ni-Ti) alloys are often used in engineering applications; therefore prototypes using this different shape memory alloy should also be tested in different environment conditions.

References

1. ANSYS Users Manual. (2003). ANSYS Inc.
2. Auricchio F., Faravelli L., Magonette G. and Torra V. (2001). *Shape Memory Alloys: Advances in Modelling and Applications*, CIMNE. Barcelona.
3. Barrett P. and Cunningham P. (2004). "Super Elastic Alloy Eyeglass Frame Design Using the ANSYS Workbench Environment", available at: http://www.caeai.com/papers/ansysconf_paper_2004_CAEA.pdf.
4. Casciati F. and Faravelli L. (2004). "Experimental Characterisation of a Cu-based Shape Memory Alloy Toward Its Exploitation in Passive Control Devices," *Journal de Physique IV*, vol. 115, 299-306.
5. Casciati F. and Hamdaoui K. (2008). "Modelling the Uncertainty in the Response of a Base Isolator," *J. Probabilistic Engineering Mechanics*, vol. 23, no. 4, 427-437.
6. Casciati F. and van Eijk C. (2008). "Mechanical Properties and Microstructure Characterization of CuAlBe Shape Memory Alloys for Vibration Mitigation," *Smart Structures & Systems*. vol. 4, no. 2.
7. Casciati F., Faravelli L. and Hamdaoui K. (2006). "Reliability Study for a New Concept of Base Isolator," *Proceedings Fifth International Conference on Computational Stochastic Mechanics*, June 20-23. Rhodes, Greece, 163-168.
8. Casciati F., Faravelli L. and Hamdaoui K. (2007a). "A Base Isolation Device with Bars in Shape Memory Alloys", *Proceedings First International Conference on Self Healing Materials*, Amsterdam, The Netherlands.
9. Casciati F., Faravelli L. and Hamdaoui K. (2007b). "Shape Memory Alloy Bars Assembled In a Base Isolator", *Asian-Pacific Network of Centers for Earthquake Engineering Research (ANCER) Meeting*, May, 29-30, Hong Kong, China.
10. Casciati F., Faravelli L. and Hamdaoui K. (2007c). "Performance-based Design of a Shape Memory Alloy Base Isolator," *Proceeding of the 10th*

International Conference on Applications of Statistics and Probability in Civil Engineering, Tokyo, Japan.

11. Casciati F., Faravelli L. and Hamdaoui K. (2007d). "Numerical Modelling of a Shape Memory Alloy Base Isolator", *Proceedings of 3rd International Conference on Structural Engineering, Mechanics and Computation*, Cape Town, South Africa.
12. Casciati F., Faravelli L. and Hamdaoui K. (2007e). "Performance of a Base Isolator with Shape Memory Alloy Bars", *J. Earthquake Engineering and Engineering Vibration*, vol. 6, no. 4, 401-408.
13. Casciati F., Magonette G. and Marazzi F. (2006). *Semi-active Devices and Applications in Vibration Mitigation*, John Wiley & Sons, Chichester, UK.
14. Casciati S. (2007). "Thermal Treatment Optimization for Cu-based Shape Memory Alloys," *First International Conference on Self-Healing Materials*, Berlin: Springer Verlag.
15. Casciati S. and Faravelli L. (2007). "Structural components in shape memory alloy for localized energy dissipation", *Computer & Structures*, vol. 86, no. 3-5, 330-339.
16. Casciati S., Faravelli L. and Domaneschi M. (2005). "Dynamic tests on Cu-based shape memory alloys toward seismic retrofit of cracked stone monuments", *Workshop on smart structures and advanced sensor technologies*. June 26-28. Santorini Island, Greece.
17. Soong, T.T. and Dargush, G.F. (1997). *Passive Energy Dissipation Systems in Structural Engineering*, John Wiley & Sons, Chichester, UK.
18. Tahiri V.L., Patoor E. and Eberhardt A. (2004). "An Analysis of the Thermomechanical Behaviour of a Shape Memory Alloy/elastomer Composite", *Journal de Physique IV*, vol. 115, 195-203.
19. Takayoshi K. and Takafumi F. (2008). "State of the Art of Development and Application of Antiseismic Systems in Japan" *Proceedings of the 2008 Seismic Engineering International Conference "MERCEA 08"*, Reggio Calabria, Italy.
20. Wikipedia encyclopedia, www.wikipedia.org

Conclusions

This Ph.D. thesis was fully supported by the INCOMED WIND-CHIME program, funded by the European Union within the 6th Framework Program (2004-2007). Such a support allowed the team to buy, treat, test and apply shape memory alloy (SMA) specimens and elements, as innovative smart material, for civil engineering applications.

This specific study treats some experimental applications based on a Cu-based Shape Memory Alloys. The selected type of SMA was mainly studied for the retrofitting of historical monuments. A prototype laboratory model was firstly built and tested on a shaking table, before and after having been sewed with a number of treated SMA wires (Chapter 3). Then, an “in situ” application was designed according to the laboratory results. The selected monument was the aqueduct of Larnaca (Chapter 4). The performance of a base isolator made of SMA bars was finally considered (Chapter 5).

The following conclusions can be drawn:

A. Pre-stressed SMA wires for structural retrofitting:

A.1 The masonry wall model

1. The design aspects related to the adoption of Cu-based SMA wires to reinforce a prototype masonry model was discussed;
2. Shaking table experiments were carried out to test the built masonry wall model, first in its virgin state, then after having been reinforced with 2, 4 and 6 SMAs ties;
3. SMA wires were pre-stressed in a way to reach the plateau of its super-elastic constitutive law (2%), so, no additional stress was transferred to the

masonry at higher strain levels; the energy dissipation was guaranteed by the possibility of mutual displacements between the masonry blocks;

4. Further energy dissipation was achieved by the hysteresis loop of the hyper-elastic stress - strain relation which characterizes the SMA alloy;
5. At the end of the test, it was seen that the ties were able to re-centre themselves in their initial position, without any residual displacement. However, under high intensity excitations, inelastic permanent deformations rise;
6. A 3-D, 8-node, solid finite elements numerical model was built in order to compare experimentally obtained results with those from numerical analysis;
7. In order to quantify the effectiveness of the retrofit and its advantages with respect to traditional techniques, the finite element model was used to evaluate the case when steel is used instead of SMA wires.

A.2 The aqueduct of Larnaca

1. The aqueduct of Larnaca, in Cyprus, was selected to be the first application of SMA ties on real historical monuments (May 1, 2007);
2. Ambient vibration tests were carried out to get the dynamic characteristics of the tested aqueduct, first without any reinforcement, then after having been sewed with 4, 12 and 20 SMA wires. Ambient vibration tests were also conducted in the unloading stage, when the wall was reinforced with 16 and 8 wires;
3. The dynamic characteristics of the monument showed considerable differences when compared with the 2004 test [Chrysostomou et al., 2004] on the acqueduct before retrofitting. The team work attributed these changes to the modification of the soil conditions due to the level of the water in the

nearby salt lake. Soil-structure interaction was proved to be quite important in this application;

4. From the gathered results, the insertion of SMA wires showed a significant effect on the dynamic characteristics of the monument;
5. The increase in the first fundamental frequency from 0.85 Hz to 1.01 Hz (period shift from 1.18 s to 0.99 s) showed an increase in the stiffness of the structure, which can be attributed to modification of the equivalent modulus of elasticity due to the pre-stressing force that makes the masonry matrix more homogeneous;
6. A discrepancy was observed between the loading and the unloading cycle, due to the difference in the load pattern followed in the sequence of pre-stressing the wires.

B. SMA bars assembled in a base isolation device:

1. A new concept of base isolator that consists of several SMA bars assembled in a suitable geometry was introduced;
2. The ANSYS software was used for the numerical modelling of the proposed prototype. The specific material required a very complex constitutive law description, where only solid and plane elements were allowed;
3. The nonlinear character of the constitutive law makes the numeric analysis cumbersome and very sensitive to the values of the many parameters to be specified;
4. The numerical studies appear unsatisfactory for accounting the actual constitutive law of the alloy: the actual behaviour in tension and compression is not accurately described, as resulting from the laboratory tests carried out;

5. The experimental tests on the prototype were carried out on a shacking table excited by a white noise realization. The main feature is that for cyclic loading, the super-elastic behaviour of the alloy results in wide load-displacement loops, where a large amount of energy is dissipated. These loops become smaller and smaller as the excitation intensity decays, resulting in the device re-cantering;
6. The following research topics require further investigation:
 - Dynamic comparison: the behaviour of the sliding system without SMA bars should be recorded during experimental tests where the excitation is increased up to the collapse of the device;
 - Performance characterization: the ratio between the diameters of the top disk over the bottom disk should be optimized;
 - Geometric design: the bar inclination should be optimized; it is likely that this depends on the device height and the above diameter ratio;
 - Numerical modelling: the difficulties met in achieving a satisfactory modelling of the shape memory alloy mainly depend on the adoption of solid hexagonal finite elements; either refinements of the mesh are required or the development of user subroutines that account for the specific exploitation of the alloy under investigation;
 - Carrying capacity: while waiting for a reliable numerical model, the existing device should be tested with different masses to identify the vertical carrying capacity.
 - Design scaling: until a reliable numerical model is developed, prototypes of different sizes should be constructed to collect preliminary information on the way a larger device could be developed;
 - Alloy alternative: despite being more expensive, nickel-titanium (Ni-Ti) alloys are often used in engineering applications; therefore prototypes

using this different shape memory alloy should also be tested in different environment conditions in a sort of material optimization.

Bibliography

1. Abadie L. (1994). *Tlemcen au Passé Retrouvé*, Editions Jacques Gandini. (In french).
2. Abdessemed-Foufa A. and Benouar D. (2005). “Atlas of Earthquake-Resistant Traditional Techniques in Algeria: The Case of the Casbah of Algiers”, *European Earthquake Engineering journal*, *EEE* 2, 05, 2-29.
3. Abed M., Bouarfa H. and Boulaghmen F. (2005). “Assistance a L'évaluation Post-Séismique des Constructions par Raisonnement Basé sur des Cas”, *Proceedings du Congrès International Réhabilitation des Constructions et Développement Durable*, May 3-4, Algiers, Algeria, vol. 2, 272-277. (In french).
4. Aghakouchak A.A., Kiamehr H. and Ghafouripour A. (2000). “An Overview of System Identification Methods and Applications Part I: Methods of System Identification and Dynamic Tests”, *Proceedings of the 4th International Conference on Coasts, Ports & Marine Structure*, Shahid Rajaei Port Complex, Bandar Abbas, Iran.
5. Ambient Vibration Response (Output-only) based System Identification. Available from URL <http://www.cse.polyu.edu.hk/~dynamics/si.htm>
6. Andersen P. (1997). “Identification of Civil Engineering Structures using Vector ARMA Models”, *Ph.D. Dissertation*, Department of Building Technology and Structural Engineering, Aalborg University, Denmark.
7. ANSYS Users Manual. (2003). ANSYS Inc.

8. Aoudia A. and Meghraoui M. (1995). "Seismotectonics in the Tell Atlas of Algeria: the Cavaignac (Abou El Hassan) earthquake of 25.08.1922." *Tectonophysics*, 248, 263-276.
9. Aoudia A., Vaccari F., Suhadolc P. and Meghraoui M. (2000). "Seismogenic potential and earthquake hazard assessment in the Tell Atlas of Algeria", *J. Seismol.*, vol. 4, 79-98.
10. Auricchio F. (1995). "Shape Memory Alloys: Applications, Micromechanics, Macromodelling and Numerical Simulations", *Ph.D Thesis*, University of California at Berkeley, USA.
11. Auricchio F., Faravelli L., Magonette G. and Torra V. (Eds.) (2001). *Shape Memory Alloys: Advances in Modelling and Applications*, CIMNE, Barcelona.
12. Auricchio F., Taylor R.L. and Lubliner J. (1997). "Shape-Memory Alloys: Macromodeling and Numerical Simulations of the Superelastic Behavior", *Computational Methods in Applied Mechanical Engineering*, vol. 146, 281-312.
13. Barrett P. and Cunningham P. (2004). "Super Elastic Alloy Eyeglass Frame Design Using the ANSYS Workbench Environment", available at: http://www.caeai.com/papers/ansysconf_paper_2004_CAEA.pdf.
14. Beck J. and Dionisio B. (2001). "A Benchmark Problem for Structural Health Monitoring", *Earthquake experimental Techniques*, vol. 25, no. 3, 49-53.
15. Bendimerad F. (2004). "The 21 May 2003 Boumerdes Earthquake Lessons Learned And Recommendations", *13th World Conference on Earthquake Engineering*, Vancouver, B.C., Canada.

16. Benouar D. and Laradi N. (1996). "A Reappraisal of the Seismicity of the Maghreb Countries – Algeria, Morocco, and Tunisia", *Natural Hazards*, vol. 13, no. 3, 275-296.
17. Benouar D. (1994). "Materials for the investigation of the seismicity of Algeria and adjacent regions during the twentieth century", *Special Issue of the Annali Di Geofisica* (Istituto Nazionale di Geofisica, Italy), vol. XXXVII, No. 4.
18. Bernard M.A. (1913). *Les chemins de fer algériens*, éditions A. Jourdan. (In french).
19. Bezzeghoud M. and Buforn E. (1999). "Source parameters of 1992 Melilla (Spain, MW= 4.8), 1994 Alhoceima (Morocco, MW= 5.8), and 1994 Mascara (Algeria, MW= 5.7) earthquakes and seismotectonic implications", *Bull. Seismol. Soc. Am.*, vol. 89, 359-372.
20. Biritognolo M., Bonci A. and Viskovic A. (2000). "Numerical models of masonry façade walls with and without SMADs", *Proceeding of Final Workshop of ISTECH Project - Shape Memory Alloy Devices for Seismic Protection of Cultural Heritage Structures*, 117-140, Joint Research Centre, Ispra, Italy.
21. Boumechra N. and Hamdaoui K. (2008). "Dynamic and Fatigue Analyses of an 18th Century Steel Arch Bridge", *Proceedings of the 2008 Seismic Engineering International Conference "MERCEA'08"*, Reggio Calabria, Italy.
22. Buehler W.J. and Wiley R.C. (1965). "Nickel-based Alloys", *Technical report*, US-Patent 3174851.
23. Caicedo J.M. (2001). "Two Structural Health Monitoring Strategies Based on Global Acceleration Response: Development, Implementation, and Verification", *Master Thesis*, Department of Civil Engineering. Washington University, St. Louis. Missouri, U.S.A.

24. Cardone D., Dolce M. and Nigro D. (1999). "Experimental test on SMA based seismic devices", *Proceedings of MANSIDE Project Final Workshop*, Rome, Italy.
25. Casciati F. (2006). "Structural monitoring for the diagnostic and the retrofitting of the monumental heritage", *Proceedings of Structural Health Monitoring and Intelligent Infrastructures*, Shenzhen University, Taylor and Francis, London, 49-54.
26. Casciati F. (ed.) (2003). *Proceeding of the 3rd World Conference on Structural Control*, John Wiley & sons, Chichester.
27. Casciati F. and Faravelli L. (2004). "Experimental characterisation of a Cu-based shape memory alloy toward its exploitation in passive control devices", *Journal de Physique IV*, vol. 115, 299-306.
28. Casciati F. and Hamdaoui K. (2008). "Modelling the Uncertainty in the Response of a Base Isolator," *J. Probabilistic Engineering Mechanics*, vol. 23, no. 4, 427-437.
29. Casciati F. and van Eijk C. (2008). "Mechanical Properties and Microstructure Characterization of CuAlBe Shape Memory Alloys for Vibration Mitigation," *Smart Structures & Systems*. vol. 4, no. 2.
30. Casciati F., Casciati S. and Faravelli L. (2007). "Fatigue characterization of a Cu-based shape memory alloy", *Proceedings of the Estonian Academy of Sciences – Physics Mathematics*, vol. 56, no. 2, 207-217.
31. Casciati F., Faravelli L. and Hamdaoui K. (2006). "Reliability Study for a New Concept of Base Isolator," *Proceedings Fifth International Conference on Computational Stochastic Mechanics*, June 20-23. Rhodes, Greece, 163-168.
32. Casciati F., Faravelli L. and Hamdaoui K. (2007a). "A Base Isolation Device with Bars in Shape Memory Alloys", *Proceedings First*

-
- International Conference on Self Healing Materials*, Amsterdam, The Netherlands.
33. Casciati F., Faravelli L. and Hamdaoui K. (2007b). "Shape Memory Alloy Bars Assembled In a Base Isolator", *Asian-Pacific Network of Centers for Earthquake Engineering Research (ANCER) Meeting*, May, 29-30, Hong Kong, China.
 34. Casciati F., Faravelli L. and Hamdaoui K. (2007c). "Performance-based Design of a Shape Memory Alloy Base Isolator," *Proceeding of the 10th International Conference on Applications of Statistics and Probability in Civil Engineering*, Tokyo, Japan.
 35. Casciati F., Faravelli L. and Hamdaoui K. (2007d). "Numerical Modelling of a Shape Memory Alloy Base Isolator", *Proceedings of 3rd International Conference on Structural Engineering, Mechanics and Computation*, Cape Town, South Africa.
 36. Casciati F., Faravelli L. and Hamdaoui K. (2007e). "Performance of a Base Isolator with Shape Memory Alloy Bars", *J. Earthquake Engineering and Engineering Vibration*, vol. 6, no. 4, 401-408.
 37. Casciati F., Magonette G. and Marazzi F. (2006). *Semi-active Devices and Applications in Vibration Mitigation*, John Wiley & Sons, Chichester, UK.
 38. Casciati S. (2007). "Thermal Treatment Optimization for Cu-based Shape Memory Alloys," *First International Conference on Self-Healing Materials*, Berlin: Springer Verlag.
 39. Casciati S. (2007). "Thermal treatment optimization for Cu-based shape memory alloys", *Proceedings of the First International Conference on Self-healing Materials*, Noordwijk, Netherlands.
 40. Casciati S. and Faravelli L. (2003). "Thermo-mechanic properties of a Cu-based shape memory alloy", *Proceedings of SMART03*, Warsaw, Poland.

41. Casciati S. and Faravelli L. (2004). "Fastening Cracked Blocks by SMA Devices", *Proceedings of the 3rd European Conference on Structural Control*, Vienna, Austria, M1-1/M1-4.
42. Casciati S. and Faravelli L. (2004). "Thermo-mechanic Characterization of a Cu-Based Shape Memory Alloy", *Proceedings SE04*, Osaka, Japan, 377-382.
43. Casciati S. and Faravelli L. (2007). "Structural components in shape memory alloy for localized energy dissipation", *Computer & Structures*, vol. 86, no. 3-5, 330-339.
44. Casciati S. and Hamdaoui K. (2008). "Experimental and Numerical Studies toward the Implementation of Shape Memory Alloy Ties in Masonry Structures", *J. Smart Structures and Systems*, vol. 4, no. 2, 153-169.
45. Casciati S. and Osman A. (2005). "Damage assessment and retrofit study for the Luxor Memnon Colossi", *J. Struct. Control Health Monitoring*, vol. 12, no. 2, 139-156.
46. Casciati S., Faravelli L. and Domaneschi M. (2005). "Dynamic tests on Cu-based shape memory alloys toward seismic retrofit of cracked stone monuments", *Workshop on smart structures and advanced sensor technologies*. June 26-28, Santorini Island, Greece.
47. CGS- Centre de Genie Paraseismic, www.cgs-dz.org.
48. Chesneau M. (1892). "Notes sur les tremblements de terre en Algérie", *Annales des mines*, neuvième série, TI, Ed Dunod, Paris, France. (In French).
49. Chrysostomou C.Z., Demetriou T. and Pittas M. (2003). "Conservation of historical Mediterranean sites by innovative seismic-protection techniques", *Proceedings 3rd World Conference on Structural Control*, Como, Italy, vol. 2, 947-954.

-
50. Chrysostomou C.Z., Demetriou T., Pittas M. and Stassis, A. (2005). "Retrofit of a church with linear viscous dampers", *J. Struct. Cont. Health Monit*, vol. 12, no. 2, 197-212.
 51. Chrysostomou C.Z., Demetriou T., Stassis A. and Hamdaoui K. (2008a). "Seismic Protection of an Ancient Aqueduct Using SMA Devices", *Proceedings of The 2008 Seismic Engineering International Conference "MERCEA '08"*, Reggio Calabria, Italy.
 52. Chrysostomou C.Z., Stassis A., Demetriou T. and Hamdaoui K. (2008b). "Application of Shape Memory Alloy Prestressing Devices on an Ancient Aqueduct", *J of Smart Structures and Systems*, vol. 4, no. 2, 261-278.
 53. Chrysostomou. C.Z., Demetriou T. and Stassis A. (2004). "Seismic protection of an aqueduct by innovative techniques", *Proceedings 3rd European Conference on Structural Control*, Vienna, Austria.
 54. Comelin P. (1720). "Voyages pour la rédemption des captifs aux royaumes d'Alger et de Tunis", *Printed by J.Ritchie, Edinburgh*, vol I, 277, 14-16.
 55. CRAAG- Centre de Recherche en Astronomie, Astrophysique et de Géophysique. (1994). "Les séismes en Algérie de 1365 à 1992". *CRAAG Report*, Algiers, Algeria. (In French).
 56. Croci G. (2000). "General methodology for the structural restoration of historic buildings: the cases of the tower of pisa and the basilica of assisi", *J. Cultural Heritage*, vol. 1, 7-18.
 57. CTC. "Le Risque Sismique en Algérie", *Centre National de Recherche Appliquee en Genie Parasismique (CTC)*, Algiers, Algeria. (In French).
 58. Delmonte G. (2007). "Pretensionamento Con Fili In Lega A Memoria Di Forma Di Elementi Strutturali Murari", *Master Thesis*, Department of Structural Mechanics, University of Pavia, Italy. (In Italian).

59. Delphin G. (1922). "Histoire des Pachas d'Alger de 1515 à 1745, Extrait d'une chronique indigène", *Extrait du Journal Asiatique (Avril-Juin 1922 et Janvier-Mars 1925)*, Paris, Imprimerie Nationale, 216-218. (In French).
60. Doebling S.W., Farrar C.R., Prime M.B. and Schevitz D.W. (1996). "Damage Identification and Health Monitoring of Structural and Mechanical Systems from Changes in their Vibration Characteristics: A Literature Review", *Los Alamos Report*, LA-13070-MS.
61. Doglioni F., Moretti A. and Petrini V., (eds.) (1994). *Le Chiese e il terremoto*, Edizione Lint, Trieste. (In Italian).
62. Dyke S.J., Caicedo J.M. and Johnson E.A. (2000). "Monitoring of a Benchmark Structure for Damage Identification", *Proceeding of the Engineering Mech. Specialty Conf.*, May 21–24, Austin, Texas, USA.
63. EERI. (2003). "The Boumerdes, Algeria, Earthquake May 21, 2003", *An EERI Learning from Earthquakes Reconnaissance Report*, Earthquake Engineering Research Institute, Oakland, California, U.S.A.
64. El-Borgi S., Choura S., Ventura C., Baccouch M. and Cherif F. (2005). "Modal identification and model updating of a reinforced concrete bridge". *Smart Structures and Systems*, vol. 1, no. 1, 83-101.
65. Faravelli L. (2002). "Experimental Approach to the Dynamic Behaviour of SMA in Their Martensitic Phase", in F. Casciati (ed.), *Proceedings of the 3rd world conference on structural control*, John Wiley & Sons, Chichester: UK, vol 2, 163-168.
66. Faravelli L. and Casciati S. (2003). "Dynamic behavior of a shape memory alloy structural devices: numerical and experimental investigation", K. Watanabe and F. Ziegler (eds.), *Dynamics of Advanced Materials and Smart Structures, IUTAM series*, Kluwer Academic Publishers, Dordrecht, Netherlands, 63-72.

-
67. Fritzen C.P. (2005). "Recent Developments in Vibration-Based Structural Health Monitoring", *Proceedings of the 5th International Workshop on Structural Health Monitoring*, Sep 12-14, Stanford University, Stanford: C A, 42-60.
 68. Frizon de Lamotte D., Saint Bezar B., Bracenc R. and Mercier E. (2000). "The two main steps of the Atlas building and geodynamics of the Western Mediterranean", *Tectonics*, vol. 19, 740-761.
 69. Grammont H. (1887). *Histoire d'Alger sous la domination turque 1515 - 1830*, Ed Levoux, Paris, France. (In French).
 70. Hamdaoui K. (2006). "Historical Monument Health Monitoring Based On Ambient Vibrations", *Master Thesis*, Department of Civil Engineering, Jordan University of Science and Technology, Irbid, Jordan.
 71. Harbi A. (2005). "Evaluation de l'aléa sismique en Algérie du Nord par la modélisation de l'input sismique dans les zones urbaines et l'établissement d'un catalogue", *Ph.D Thesis*, University of Algiers, Algeria. (In French).
 72. Horne A. (2006). *A Savage War of Peace: Algeria 1954-1962*, (New York Review Books Classics). 1755 Broadway, New York, NY 10019: NYRB Classics, 29-30.
 73. Isalgue A., Torra V. and Lovey F.C. (2002). "Cu-based SMA: Quantifying and Guaranteeing the Time and temperature Dependence on Damping", in F. Casciati (ed.), *Proceedings of the 3rd Word Conference on Structural Control*, John Wiley & sons, Chichester, UK, vol. 2, 363-368.
 74. Kullaa J. (2003). "On line Structural Health Monitoring", *Proceedings of the 3rd Word Conference on Structural Control*, Como, Italy, vol. 3, 133-138.
 75. La démographie figurée de l'Algérie, available on line: <http://gallica.bnf.fr/ark:/12148/bpt6k103772b>. (In French)

76. Magpantay H.A. "Modal Identification from Ambient Vibration Measurement: a Technology for Optimization of the Performance of Civil Engineering Structure". [Online], Available from URL <http://www.adnu.edu.ph/Research/gibon4v1n1.asp> --
77. Matlab [Computer Program]. Version 7 (R14). *The MathWorks Inc*; 2004. Available: <http://www.mathworks.com>.
78. McKenzie D. (1972). "Active tectonics of the Mediterranean region", *Geophys. J. R. Astron. Soc.*, vol. 30, 109-185.
79. Meghraoui M. (1988). "Géologie des zones sismiques du nord de l'Algérie, tectonique active, paléo-sismologie et synthèse sismotectonique", *PhD dissertation*, University of Paris-Sud, France. (In French).
80. Mickus K. and Jallouli C. (1999). "Crustal structure beneath the Tell and Atlas Mountains (Algeria and Tunisia) through the analysis of gravity data", *Tectonophysics*, vol. 314, 373-385.
81. Morton P. (2003). "Le développement des chemins de fer en Algérie", *Extrait de la revue du Gamt*, no. 71/2003/3 and 72. (In French).
82. Press. (1716). *Gazette de France*, no. 8 of 10th and 20th, March.
83. Rytter A. (1993). "Vibration Based Inspection of Civil Engineering Structures", *Ph.D. Dissertation*, Department of Building Technology and Structural Engineering, Aalborg University, Denmark.
84. Saadat S., Salichs J., Noori M., Hoo Z., Davoodi H., Bar-on I., Suzuki Y. and Masuda A. (2002). "An Overview of Vibration and Seismic Application of NiTi Shape Memory Alloys", *Smart Materials and Structures*, vol. 11, no. 2, 218-229.

85. Saidouni N. (1985). "El ahwâl ech-chakhsiâ wa al-wadh ed-dimoghrâfi fi al-djazâ'ir athnâa al-aahd al-othmâni". In *Revue d'Histoire du Maghreb*, no. 39-40, 431-445. (In Arabic)
86. SAP 2000. (2003). [Computer Program]. Version 8, Computer and Structures, Inc.
87. SmartLab, <http://smart.tamu.edu/>.
88. Soong T.T. and Dargush G.F. (1997). *Passive Energy Dissipation Systems in Structural Engineering*, John Wiley & Sons, Chichester, UK.
89. Syrmakezis K. and Sophocleous A. (2002). "Passive Control Techniques for the Seismic Protection of Historical and Monumental Masonry Structures", *Proceeding of the 3rd World Conference on Structural Control*, Come, Italy, vol. 2, 955-960.
90. Tahiri V.L., Patoor E. and Eberhardt A. (2004). "An Analysis of the Thermomechanical Behaviour of a Shape Memory Alloy/elastomer Composite", *Journal de Physique IV*, vol. 115, 195-203.
91. Takayoshi K. and Takafumi F. (2008). "State of the Art of Development and Application of Antiseismic Systems in Japan" *Proceedings of the 2008 Seismic Engineering International Conference "MERCEA'08"*, Reggio Calabria, Italy.
92. Tapponier P. (1977). "Evolution tectonique du système Alpin en Méditerranée poinçonnement et écrasement rigide plastique", *Bull. Soc. Geol. Fr.*, vol. 19, 437-460.
93. Tassy L. (1830). *Histoire d'Alger et du bombardement de cette ville en 1816*, Librairie Piltan, Paris, France. (In French).
94. Wenzel H. "Structural Assessment of the Cultural Heritage", Available online from URL <http://www.brimos.com/pdf/cultural.pdf>

95. Wenzel H. and Pichler D. (2005). *Ambient Vibration Monitoring*, England. John Wiley and Sons.
96. Wikipedia encyclopedia, www.wikipedia.org
97. WIND-CHIME 2004-2007, <http://dipmec.unipv.it/chime/>.
98. Zonta D. (2000). "Structural Damage Detection and Localization by Using Vibrational Measurements", *Ph.D. Dissertation*, University of Bologna. Bologna, Italy.